Theses   UAH Electronic Theses and Dissertations

2021

Assessment of performance parameter uncertainty of a solid fuel ramjet

William Jarrett Hankins

ASSESSMENT OF PERFORMANCE PARAMETER UNCERTAINTY OF A SOLID FUEL RAMJET

by
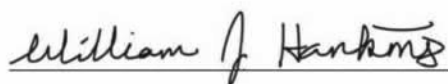
WILLIAM JARRETT HANKINS

A THESIS

Submitted in partial fulfillment of the requirements
for the degree of Master of Science
in
The Department of Mechanical and Aerospace Engineering
of
The School of Graduate Studies
of
The University of Alabama in Huntsville

HUNTSVILLE, ALABAMA
2021

In presenting this thesis in partial fulfillment of the requirements for a master's degree from the University of Alabama in Huntsville, I agree that the Library of this University shall make it freely available for inspection. I further agree that permission for extensive copying for scholarly purposes may be granted by my advisor or, in his/her absence, by the Chair of the Department or the Dean of the School of Graduate Studies. It is also understood that due recognition shall be given to me and to The University of Alabama in Huntsville in any scholarly use which may be made of any material in this thesis.
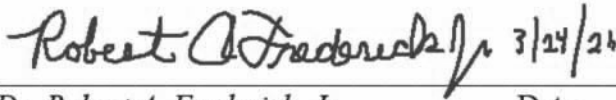

William J. Hankins   March 24, 2021

William J. Hankins   Date

THESIS APPROVAL FORM

Submitted by William J. Hankins in partial fulfillment of the requirements for the degree of Master of Science in Engineering in Aerospace Systems Engineering and accepted on behalf of the Faculty of the School of Graduate Studies by the thesis committee.

We, the undersigned members of the Graduate Faculty of The University of Alabama in Huntsville, certify that we have advised and/or supervised the candidate of the work described in this thesis. We further certify that we have reviewed the thesis manuscript and approve it in partial fulfillment of the requirements for the degree of Master of Science in Engineering in Aerospace Systems Engineering.
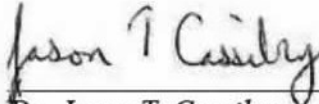
_____ 3/24/24 _____ Committee Chair
Dr. Robert A. Frederick, Jr.   Date

_____ 3-24-21 _____
Dr. David M. Lineberry   Date
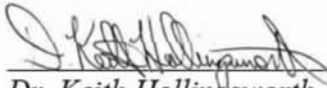
_____ 3/24/2021 _____
Dr. Jason T. Cassibry   Date

_____ 3/26/2021 _____ Department Chair
Dr. Keith Hollingsworth   Date

Shankar Mahalingam — Digitally signed by Shankar Mahalingam
Date: 2021.03.31 16:55:25 -05'00'   College Dean
Dr. Shankar Mahalingam   Date

_____ Yeqing Bao 4/1/2021 _____ Graduate Dean
Dr. Sean Lane   Date

ABSTRACT
School of Graduate Studies
The University of Alabama in Huntsville

Degree <u>Master of Science in Engineering</u>   College/Dept. <u>Engineering/Mechanical and Aerospace Engineering</u>

Name of Candidate <u>William J. Hankins</u>

Title   <u>Assessment of Performance Parameter Uncertainty of a Solid Fuel Ramjet</u>

    This research develops a methodology for quantifying the uncertainties in key experimentally determined performance parameters for two solid fuel ramjet propellants in a connected pipe ramjet using the Monte Carlo Method. The performance parameters include characteristic velocity, characteristic velocity efficiency, thrust, specific impulse, and vacuum specific impulse. The burning rate equations and their uncertainty intervals were also calculated. Burning rate equations were constructed with terms in air flux and air temperature. The uncertainty intervals were found to be 4% - 5.1% at the test points. The burning rates were found to be accurate within $\pm$ 7.7%. Uncertainties in the performance parameters ranged from 16% - 37%. The dominant uncertainties were the nozzle throat diameter, which was affected by slag, and the combustor pressure. Recommendations for test procedures could lower uncertainty by up to 64% for the nozzle and by up to 45% for the combustor pressure.

Abstract Approval: Committee Chair   _____
                                       Dr. Robert A. Frederick, Jr.

                      Department Chair _____ 3/26/2021
                                       Dr. Keith Hollingsworth

                      Graduate Dean   _*Yeqing Bao*_ *4/1/2021*
                                         Dr. Sean Lane

ACKNOWLEDGEMENTS

This thesis would not have been possible without the assistance of the committee. I would like to thank Dr. Robert A. Frederick for his guidance, wisdom, and support while serving as my advisor. I would like to thank Dr. David M. Lineberry for his plentiful assistance in the experiment and analysis as well as effectively serving as my second advisor. Lastly, I would like to thank Dr. Jason T. Cassibry for his support throughout this project.

I would like to thank Dr. Brian McDonald and Dr. Daniel Jones for their support and for allowing me to participate on this research program.

I would like to offer special thanks to the PRC test staff for the running the tests. Their support was what enabled the testing to be completed.

Lastly, I would like to thank my family for the love and support throughout the thesis writing process and throughout my collegiate career.

TABLE OF CONTENTS

LIST OF FIGURES

FIGURE											PAGE

LIST OF TABLES

LIST OF SYMBOLS

SYMBOL	DEFINITION
a	Burn rate coefficient
A	Area
A_{throat}	Throat area
A_{LL1}	Formulation A at test LL1
A_{up}	Upstream flow area
b	Burn rate mass flux exponent
B	Systematic uncertainty
B_{LL1}	Formulation B at test LL1
$\bar{B}$	Systematic uncertainty of the mean
c_D	Coefficient of discharge
$c(k)$	Linear regression constant at iteration k
c^*	Characteristic velocity
C_F	Coefficient of thrust
d	Diameter
d_i	Inner diameter of the fuel grain
d_o	Outer diameter of the fuel grain
F	Thrust
F_{LC}	Thrust measured by load cell
F_{PL}	Thrust cell preload

g_0	Gravitational constant
G	Mass flux
I_t	Total impulse
I_{sp}	Specific impulse
$I_{sp,vac}$	Vacuum specific impulse
L	Length
m_{assy}	Mass of fuel grain assembly
m_b	Mass burned
m_{liner}	Mass of fuel grain liner
m_p	Mass of propellant
m_{post}	Mass of fuel grain post burn
$m(k)$	Linear regression coefficient at iteration k
$\dot{m}$	Mass flow
M	Mach number
n	Burn rate pressure exponent
N	Number of items
O/F	Oxidizer to fuel ratio
p	Pressure
p_t	Total Pressure
P	Random uncertainty
$\bar{P}$	Random uncertainty of the mean
q	Burn rate temperature exponent

R	Specific gas constant
r	Result
$\dot{r}$	Burn rate
$\dot{r}_{conf}$	Burn rate confidence interval
S	Standard deviation
$\bar{S}$	Standard deviation of the mean
t	Time
t_b	Burn time
$t_{b,f}$	Burn time end
$t_{b,s}$	Burn time start
t_{burn}	Burn time in test sequencing
t_{ign}	Ignition time in test sequencing
$t_{preheat}$	Preheat time in test sequencing
T	Temperature
T_t	Total temperature
u	Standard uncertainty
U	Expanded uncertainty
$\bar{U}$	Expanded uncertainty of the mean
UPC	Uncertainty Percentage Contribution
$\overline{UPC}$	Uncertainty Percentage Contribution of the mean
v	Velocity
w_b	Web burned

X	Input variable
$\bar{X}$	Mean of input variable
Y	Output variable
Y_{new}	New output variable from regression fit

GREEK	DEFINITION
β	Elemental systematic error
γ	Ratio of specific heats
ε	Elemental random error
δ	Total error
η_{comb}	Combustion efficiency
η_{c^*}	Characteristic velocity efficiency
$\eta_{I_{sp}}$	Specific impulse efficiency
$\eta_{\Delta T}$	Thermal rise efficiency
θ	Nozzle exit angle
ρ_p	Propellant density

SUBSCRIPT	DEFINITION
∞	Freestream
0	Pre-inlet
1	Inlet-lip
2	Post-inlet

3	Combustor head end
4	Combustor aft end
5	Ramjet nozzle Throat
6	Ramjet nozzle exit
a	Air
f	Fuel
$H2$	Hydrogen
HH	High mass flow and high temperature setpoint
HL	High mass flow and low temperature setpoint
i	Iterator
k	Iterator
LH	Low mass flow and high temperature setpoint
LL	Low mass flow and Low temperature setpoint
m	measured variable
noz	Sonic nozzle
$O2$	Oxygen
r	Result
th	Theoretical
$tube$	Upstream tube
X	Input variable
$X_i X_k$	Correlated variables at i and k
Y	Output variable

CHAPTER 1

INTRODUCTION

The Ramjet has been a subject of interest to the international development community for over one hundred years. Ramjets boast greater specific impulse than conventional liquid or solid rocket propulsion and can operate at much greater speeds than traditional duct jet propulsion such as turbojet or turbofan engines. Ramjets excel at supersonic velocities between Mach 2.5 and Mach 6. Such speeds provide extended range and shorter transit times when compared to turbojets and turbofans. As such, they have enjoyed much military interest for their clear advantages to alternative propulsion systems [1]. It is through such interest that the University of Alabama in Huntsville (UAH) has characterized the performance and experimental uncertainties a variety of solid fuel ramjet (SFRJ) motors as part of an ongoing research program. The process and results of this characterization are presented in this thesis.

1.1 Ramjet Overview

Ramjets are the one of the simplest forms of duct jet propulsion. The most popular form of this type of propulsion is the turbojet engine that is commonly seen on most modern commercial and military aircraft today. All duct jet propulsion captures external air, energizes it, and expels it to obtain thrust. Most modern duct jet propulsion systems compress the external air before being mixed with a propellant and burned. Turbojets rely

on mechanical turbocompressors to compress the external air to the desired temperature and pressure for combustion. Ramjets instead perform this process by capturing the air through a contoured intake into the combustor using the resulting supersonic shocks in the intake to perform the compression action as a type of subsonic diffuser. This requires the vehicle move at supersonic speeds usually Mach 2 or greater. Ramjets have subsonic internal speeds in the combustor while scramjets are supersonic [2].

A variety of ramjets types exist based on what type of fuel they burn. Ramjets can burn gaseous, liquid, or solid propellants. Liquid propellants are introduced in the flow stream at the head end of the combustor. Solid propellants in ramjets are similar to hybrid rockets in that they often line the walls of the combustor and burn away throughout the run time [1].
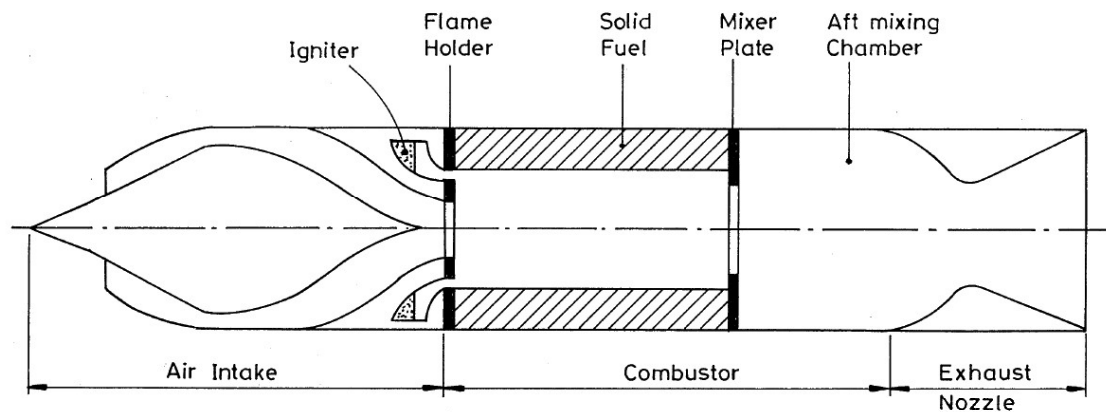
Figure 1.1: Notional Solid Fuel Ramjet Layout [3]

Figure 1.1 shows a notional schematic of a solid fuel ramjet and its major features including intake, combustor, and nozzle. The intake is responsible for capturing air and compressing it for combustion. In the combustion chamber, the propellant and air are

mixed and burned. Many designs include a mixing chamber to allow to for the completion of the combustion process which improves performance. Lastly, the nozzle extracts energy from the flow in the forms of temperature and pressure and converts them into kinetic energy to maximize the exit velocity [1].

1.2 Motivation

The University of Alabama in Huntsville has been testing numerous experimental propellant formulations for ramjets. In order to quantify the performance of the new propellants for solid fuel ramjets, several performance parameters were determined such as characteristic velocity (c^*), characteristic velocity efficiency (η_{c^*}), thrust (F), specific impulse (I_{sp}), and vacuum specific impulse ($I_{sp,vac}$). In addition, a burning rate equation for each solid fuel formulation was determined. It was desired to determine the combined uncertainties (U_c) to provide 95% confidence intervals for each performance parameter and burning rate equation. These performance parameters allow for the propellants to be compared to find the superior option for a target application but only if there is a significant enough of a difference between them to not fall into the confidence intervals of the other propellants.

1.3 Objectives and Scope

The primary objective of this study is to calculate the values of key performance parameters and burn rate equations as well as their combined expanded uncertainties for two different formulations of SFRJ propellant in order to compare their compare their performance with greater confidence. The propellants were studied using in a laboratory-

3

scale connected pipe configuration with heated air. Eight tests were performed for each propellant at four set points. Air mass flow and air temperature were varied 0.146 to 0.238 lbm/s and 662 to 800 °F between tests to evaluate the performance over a range of potential flight conditions. The uncertainties for each of the parameters and burn rate equations were calculated using the Monte Carlo Method (MCM). It is also goal of this thesis to establish a baseline methodology for the analysis of ramjet performance and uncertainty for future work at UAH's Propulsion Research Center.

CHAPTER 2

BACKGROUND

This chapter establishes an overview of ramjets interests and testing methodologies. The baseline ramjet performance parameter equations are reviewed as well as the measurement of burn rate. Burn rate equations are from literature discussed, and following that, the determination of combined uncertainty is presented. This chapter serves as a critical assessment to guide the approach, methods, and analyses for this research study.

2.1 Overview of Modern Ramjet Interest and Research

This section provides a brief overview of the history of ramjet propulsion and its current direction. An overview of modern research literature is presented, which is by no means exhaustive, to highlight the modern interests in the field. The major research categories found were to be fuels development and combustor development. There was found to be a general lack of literature focusing on the uncertainty analysis process for ramjet systems in recent history.

2.1.1 Ramjet History

Ramjets have seen use with militaries and space programs around the world. With a desire for flight vehicles to operate in the supersonic and hypersonic regimes, they have been the choice of propulsion system. While they have been explored for over one hundred years, strong interest formed during the World War 2 [1, 4]. Some older fielded systems are show in Figure 2.1.
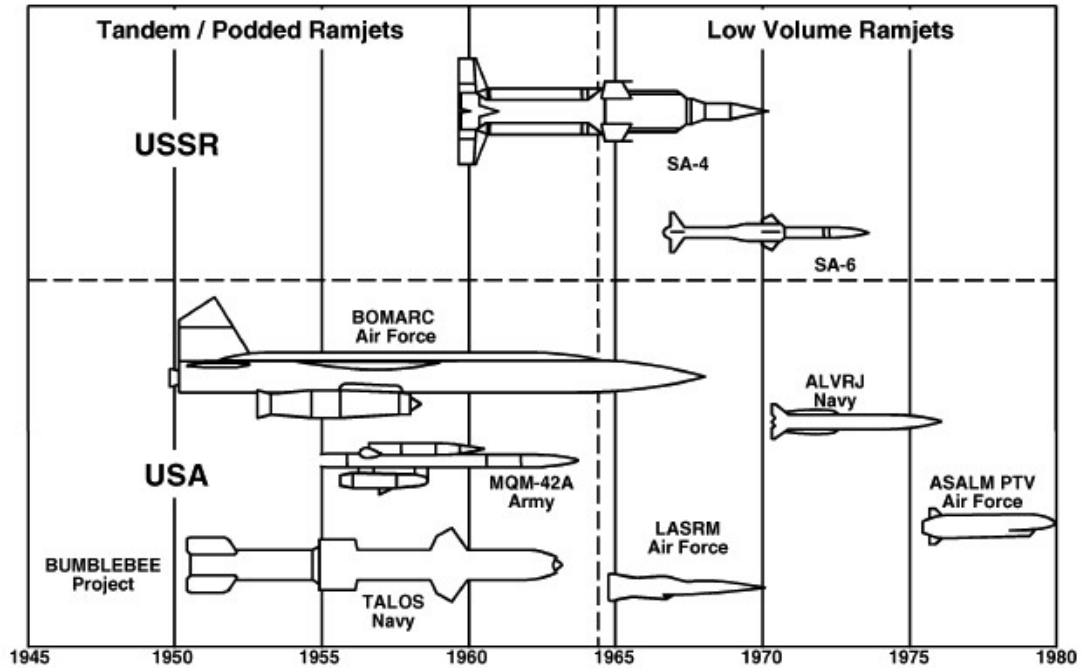
Figure 2.1: Early Ramjet Systems [1]

Perhaps the most popular ramjet vehicle was the Lockheed Martin SR-71 Blackbird. The Blackbird served as a spy plane for the Unites States. It utilized the Pratt and Whitney J58 engine to reach speeds greater than Mach 3 [1].

The most popular uses for ramjets historically have been for anti-aircraft and anti-ship missiles. The United States has produced a large number of experimental programs dedicated to this with operational examples including the TALOS and the Vandal anti-aircraft missiles [5]. Other nations have fielded their own ramjet systems, notably the USSR, to maintain relevance in the fight for air dominance [1].

Modern interest in ramjets focuses on hypersonic regime. A need for speed has been identified resulting in the creation of the hypersonic strike vehicle. American examples include the Lockheed Martin SR-72 and Boeing X-51 [6, 7]. China and Russia

are working on their own versions. Future work will continue to focus on the demands of the defense industry as the world powers vie for dominance of the hypersonic regime [7].

2.1.2 Fuel Development

Fuel development has been and will continue to be an active area of research. Improved performance in thrust to weight, efficiency, and safety drive this initiative. To that end, gel fuels have seen interest for their potential compared to traditional liquid and solid fuels. Gel fuels are liquid fuel and oxidizers with gelling agents added to produce non-Newtonian fluids. The gelling action of the propellants improves safety by automatically plugging leaks and allowing for the suspension of powdered additives [8, 9]. Powdered propellants additives to gel fuels, in addition to powdered fuels on their one was another focus of recent ramjet fuel research. Powdered propellants such as boron, aluminum, and magnesium can boost performance of the fuels. This has seen some success in modern research with the basis for the technology established in 40's and 50's research [10].

2.1.3 Combustor Development

In addition to the development of the fuels for ramjets, the combustor sections have seen improvements to their design and modeling. Following the increase in interest in gel fuels, combustor design has been explored that maximize the potential of gel fuels at the laboratory scale [11].

Numerical modeling of the combustor has seen research interest with the continual improvement of simulation software and hardware. Numerical models are being used to

predict the performance of new ramjet and scramjet formulations. Current techniques are showing agreement to experimental data to within 6.2% [12]. Using numerical models are also being new types of ramjet technology such as a turbocharged SFRJ which is similar to an air turbo ramjet. This method has not had experimental results published as of date [13].

Swirling of the gases in the combustor chamber was another recurrent topic. Swirling the flow can improve burn rates and flame stability but was found to negatively impact ignition and specific impulse. Numerical studies followed by experimental work has been performed and is ongoing [14, 15].

2.1.4 Role of Uncertainty Analysis in Literature

In the modern research on ramjets, it was found that there was a gap in the uncertainty analysis methods. Some articles do not deal with uncertainty at all, while those who did were usually only 1st order. Older work from Blevins and Coleman investigates and evaluate the uncertainties in ramjet testing, but the modern literature has not addressed these topics in detail [16].

Uncertainty analysis is a critical part to any research program and for presenting research to the greater scientific community. The formulations tested as part of the ongoing research program at UAH are attempting to improve SFRJ performance like most modern ramjet research. A rigorous uncertainty analysis is required to validate the results and establish confidence bounds for comparison between tested formulations and with results from other research groups. This thesis attempts to accomplish this.

2.2 Ramjet Test Facility Types

There are three major types of ramjet ground test facility configurations. They are the freejet method, the connected pipe method, and the semi freejet method. A freejet setup seeks to replicate the flight conditions for the testing of the ramjet. The air temperature, pressure, Mach number, and chemical composition are matched to the target altitude and speed. The test cell air stream is large enough to enclose the entire propulsion system so that all elements of the ramjet are tested. Freejet testing is the most expensive of the methods, none of which are inexpensive to begin with, but it does provide the most realistic results. An example setup is shown in Figure 2.2 [17].
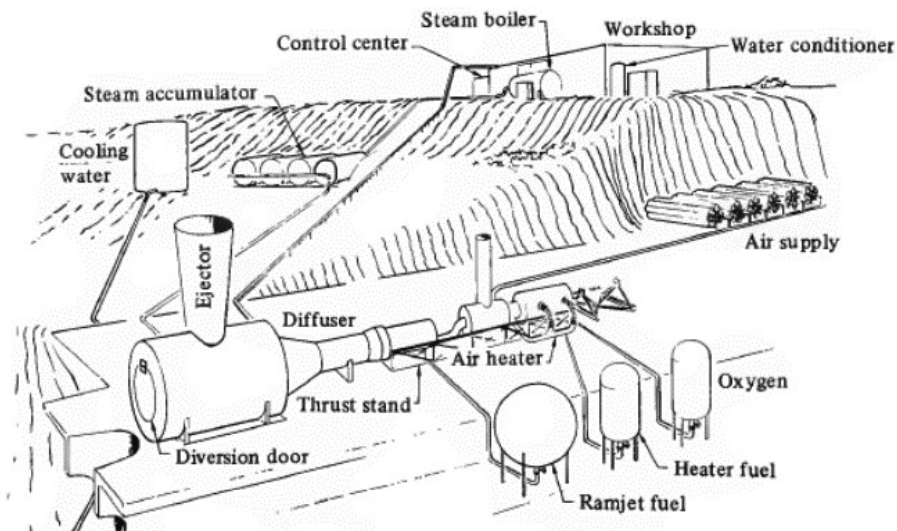
Figure 2.2: Freejet Test Facility [17]

The connected pipe method focuses on the combustion chamber. Only the combustion chamber and nozzle are included in the approach. An example is shown in Figure 2.3. The combustion chamber is fed heated air that is tailored to match predicted

combustor inlet conditions. Connected pipe testing is the least expensive of the three and

serves well for studying the combustion/nozzle processes, and the screening of fuels [17].
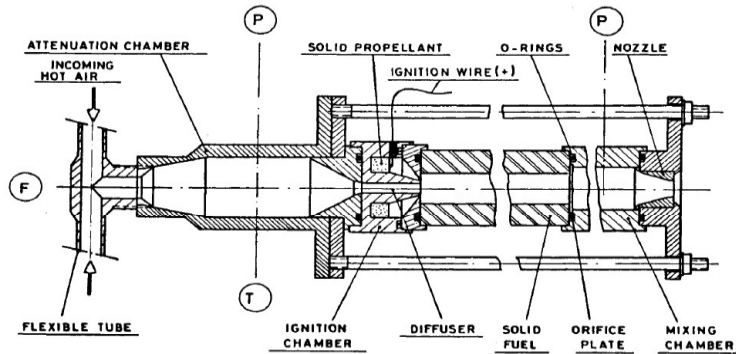
Figure 2.3: Connected Pipe Test Schematic [17]

Lastly, semi freejet testing is a hybridization the prior methods. An example is

shown in Figure 2.4. It mimics the freejet method in that simulated air is passed into the

nozzle section of the ramjet but differs in that there is no air passed over the remainder of

the ramjet. With the exception of the air intake, the process is the same as the connected

pipe methods. The semi freejet method allows of the study of the air intake system without

the complexity and cost of the freejet method [17].
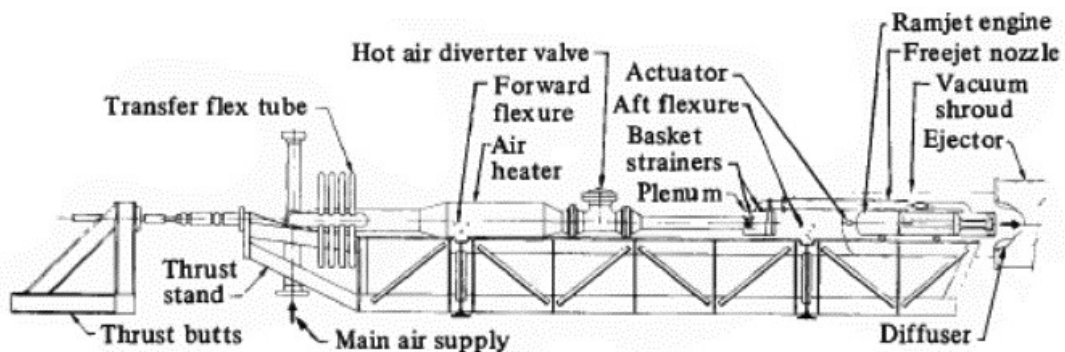
Figure 2.4: Semi Freejet Test Schematic [17]

2.3 Ramjet Performance Parameters

For this work, the Advisory Group for Aerospace Research and Development (AGARD) scheme for station numbering was employed. A schematic for the numbering scheme is shown in Figure 2.5 with the descriptions for the stations listed in Table 2.1. AGARD includes accommodations for an air bypass inlet which is not used in this work [18].
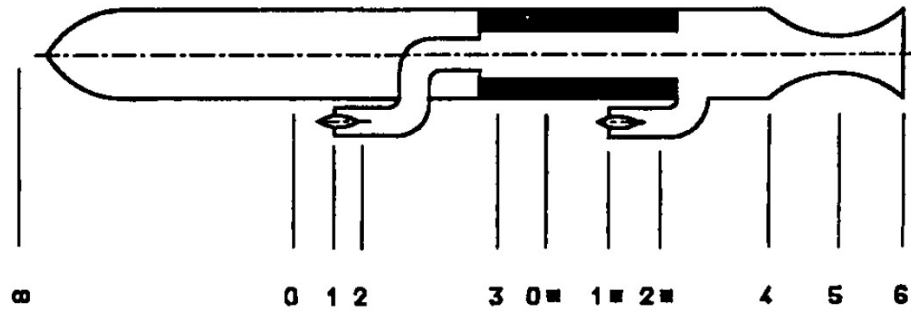
Figure 2.5: SFRJ Station Numbering Scheme [18]

Table 2.1: SFRJ Station Descriptions

Number	Description
∞	Freestream
0	Pre-Inlet
1	Inlet Lip
2	Post-Inlet
3	Combustor Head End
4	Combustor Aft End
5	Nozzle Throat
6	Nozzle Exit
■	Bypass Stations (Unused)

A variety of performance parameters exist for ramjets. Of interest in this study were the thrust, specific impulse, vacuum specific impulse, and characteristic velocity.

11

They are all discussed as well as various methods for their evaluation. Three different efficiency parameters are also discussed. They are c^* efficiency (η_{c^*}), $I_{sp,vac}$ efficiency ($\eta_{I_{sp,vac}}$), and temperature rise efficiency ($\eta_{\Delta T}$) The efficiencies are normalized with theoretical performance predictions and serve as proxies for combustion efficiency.

2.3.1 Thrust

Thrust is the force produced by a propulsion device. It is a measure of the momentum exchange between the propellants from their initial to final stages. In the case of a ramjet, external air is brought in, mixed with fuel, burned, and expelled at a greater velocity than the inlet velocity. The components of the steady state thrust equation are difference in momentum between intake and output (momentum thrust) and a pressure difference projected on the exit area of the nozzle (pressure thrust) are [19].

$$F = \dot{m}_6 v_6 - \dot{m}_1 v_\infty + (p_6 - p_\infty)A_6 \qquad (2.1)$$

The first two terms on the right-hand side represent the momentum change between the intake and output by the working fluid. The $\dot{m}$ represents the mass flow at the specified station. The $\dot{m}_6$ has mass flow added from the engine by the fuel. The v represents the average velocity at the specified station. At the nozzle exit an additional thrust term exists from the difference of pressures between the nozzle exit and the surrounding atmosphere. This term is zero when ($p_6 = p_\infty$), and it is usually more advantageous to design a nozzle to convert any pressure into additional momentum within the first two terms of Equation 2.1 [19].

Thrust can either be measured directly on a thrust stand or calculated in a variety of methods. The most obvious calculation is to measure the variables defined in Equation 2.1. Unfortunately, measurements of the mass flow, velocity, and pressure at the nozzle exit are difficult to obtain directly. Using thermodynamics, it is possible to condense these variables into the form shown in Equation 2.2 which represents force as the product of the coefficient of thrust (C_F), the total pressure of the combustor, and the area of the throat.

$$F_6 = C_F p_{t4} A_5 \qquad (2.2)$$

Equation 2.3 shows formula to calculate the coefficient of thrust.

$$C_F = \frac{1 + \cos\theta}{2} \sqrt{\frac{2\gamma^2}{\gamma - 1}\left(\frac{2}{\gamma + 1}\right)^{\frac{\gamma+1}{\gamma-1}}\left[1 - \left(\frac{p_6}{p_{t4}}\right)^{\frac{\gamma-1}{\gamma}}\right]} + \frac{(p_6 - p_\infty)A_6}{p_{t4}A_5} \qquad (2.3)$$

The grouping with a cosine present is the nozzle efficiency factor which requires the half angle of the nozzle (θ) at the exit. It accounts for momentum losses due to off axis flow. The second grouping with the square root accounts for the momentum thrust gained by the nozzle. The last term accounts for force produced by any pressure gains or losses at the end of the nozzle due to a difference in exit pressure and atmospheric pressure [2].

The major challenge in calculating the thrust and thrust coefficient is in how to calculate the total pressures. Unlike in rockets where the measured chamber pressure is assumed to be the stagnation value, ramjets and hybrid rockets have an active enough flow throughout their combustion chamber which invalidates that assumption. Measured

pressures are typically static pressures to be noninvasive and to be able survive the hot combustion products. Total pressure must be obtained from the values measured [1, 2].

Equation 2.5 is used to calculate the total pressure. To accomplish this, the Mach number (M) at the aft end of the combustor must be calculated. The equation for this is shown in Equation 2.4 which calculates Mach number from the ratio of the throat area (A_{throat}) and upstream area (A_{up}). M appears on both sides of the equation thereby a root solver is required to solve for the Mach number [18]. Experimental values or theoretical values from a thermochemical code can be used to compute the ratio of specific heats, γ [16]. Equations 2.4 and 2.5 are shown in a generic form for any isentropic flow [2].

$$M = \frac{c_D A_{throat}}{A_{up}} \left(\frac{2}{\gamma + 1} + \frac{\gamma - 1}{\gamma + 1} M^2 \right)^{\frac{\gamma - 1}{2(\gamma + 1)}} \tag{2.4}$$

$$p_t = p \left(1 + \frac{\gamma - 1}{2} M^2 \right)^{\frac{\gamma}{\gamma - 1}} \tag{2.5}$$

2.3.2 Specific Impulse

Equation 2.6 shows the form for the determination of average total impulse. Impulse, I_t, is proportional to the total momentum imparted by the propulsion device [2].

$$I_t = F_6 t_b \tag{2.6}$$

Average Specific impulse, shown in Equation 2.7 as I_{sp}, is the total impulse normalized on a per weight basis. The reference gravity for weight is the reference Earth gravity (g_0). The total mass of the propellant burned is represented by m_b. Specific is the

most common measure of economy for a propellant for rocketry. A higher value of specific impulse means that a propellant provides more impulse, the total ability to change the velocity of the vehicle, per unit weight. It is not a perfect economy measure, but it does appear directly in several astrodynamics calculations that govern performance of spacecraft [2].

$$I_{sp} = \frac{I_t}{m_b g_0}$$ (2.7)

An issue arises in specific impulse calculations when the freestream pressure, or atmospheric pressure for static test firings, is different between tests or testing locations. A lower pressure helps to deliver more thrust. In solid rocketry, the external pressure is frequently normalized to the ambient pressure at sea level. In ramjets it is appropriate to normalize to a vacuum, a proxy for high altitude flight, which results in an alternative form of the specific impulse equation. This is called the vacuum specific impulse; the formula for averaged version is shown in Equation 2.8 [18].

$$I_{isp,vac} = \frac{I_t + p_\infty A_6 t_b}{m_b g_0}$$ (2.8)

2.3.3 Characteristic Velocity

A common figure of merit among propellants is the characteristic velocity (c^*). Characteristic velocity is a fictious velocity in a ramjet or rocket and is independent of the nozzle geometry. This makes it ideal for an even comparison between different propellants

and as a measure of combustion chamber performance and is compared with a theoretical maximum to determine combustion efficiency. [2]. Equation 2.9 shows the formula for c^* in a ramjet using measured pressure and mass flow. Equation 2.10 shows the two component mass flows, mass flow of air ($\dot{m}_a$) and mass flow of fuel ($\dot{m}_f$), that sum to become the total mass flow exiting the combustor.

$$c^* = \frac{c_{D5}p_{t4}A_5}{\dot{m}_4} \tag{2.9}$$

$$\dot{m}_4 = \dot{m}_a + \dot{m}_f \tag{2.10}$$

Equation 2.11 shows the formula using the thermodynamic definition which requires knowledge of the ratio of specific heats (γ)and total temperature of the combustor (T_{t4}). The total temperature of the combustor, ratio of specific heats, specific gas constant of the combustion products (R), and coefficient of discharge for the nozzle (c_{D5}) are required. The ratio of specific heats and specific gas constant are typically obtained from thermochemical software at a particular O/F ratio [18, 2].

$$c^* = \frac{\sqrt{\gamma R T_{t4}}}{\gamma \sqrt{\left[\frac{2}{\gamma+1}\right]^{\frac{\gamma+1}{\gamma-1}}}} \tag{2.11}$$

The determination of c^* has complexities regardless of the form used. In the first form in Equation 2.9, pressure, mass flow, throat area, and the throat coefficient of discharge must be accurately determined which is not a trivial task. Pressure is frequently

the easiest of these as it is usually possible to insert a pressure transducer on or near the combustion chamber. Converting from static pressure to total pressure requires information on the combustion products' properties and geometry of the combustor, which can be a variable in some cases [20].

The mass flow of the air can be measured in a variety of ways notably by constriction flow meters or more directly by Coriolis flow meters. Inherent to flow meters is the effect they impose on the incoming air which is of the same type discussed shortly in the coefficient of discharge for the ramjet [21, 22].

The mass flow of the fuel is difficult to measure. Measurements of the grain can be made before and after a test firing, and when coupled with knowledge of the fuel density and grain geometry, a fuel mass flow can be determined. This methodology assumes a good knowledge of the density of the fuel which is not always valid. Voids and other imperfections can cause a deviation from the theoretical density and can also lead to issues with uneven burning [2].

The coefficient of discharge can be obtained through cold flow tests using similar fluids. Those forms of experiments capture effects such as the vena contracta and flow losses, but they ignore thermal effects. These appear in the experiment as a shrinking of the effective nozzle area, usually captured in the c_D, due to both a thermal boundary layer on the walls of the nozzle and the shrinking of the nozzle due to thermal expansion of the nozzle material [23].

For the second form of c^* calculation, shown in Equation 2.11, temperature measurements can be difficult to obtain in the combustor. To survive the intense conditions, a durable thermocouple, almost always with large time constant, must be used

and even then, it must be replaced frequently [24]. Another issue is that depending on where the temperature probe is placed it will only capture a small point of the flow field temperature which may not be satisfactory depending on the type of motor [25].

The ratio of specific heats and specific gas constant frequently comes from thermochemical equilibrium software which has many assumptions included as parts of its analysis [2]. Estimates, such as the one shown in Equation 2.12, can be used in lieu of a prediction from a combustion code [18]. The coefficient of discharge has the difficulties as previously mentioned for the other form of the c^* equation.

$$\gamma = \frac{\ln(p_4/p_5)}{\ln(p_4/p_5) - \ln(T_4/T_5)} \tag{2.12}$$

2.3.4 Characteristic Velocity Efficiency

The c^* efficiency attempts to represent combustion efficiency as the ratio of a theoretical c^* vs the measured c^*. The experimental value for c^* can be obtained with Equation 2.9 or Equation 2.11 where the theoretical value is obtained with a chemical equilibrium code. Variety in the calculation methods comes from how the experimental total pressure (p_{t4}) is determined [18].

$$\eta_{c^*} = \frac{c^*}{c^*_{th}} \tag{2.13}$$

The first method relies on determining the total pressure as shown in Equation 2.5 and Equation 2.4 using knowledge of the ramjet geometry, static pressures, and specific

heats. The second and third methods presented require a measurement of thrust at the nozzle throat (F_5) to be made [18]. The formula for thrust at the nozzle throat, as it would be determined on a thrust stand, is shown in Equation 2.14 with the formula for total pressure using thrust and γ shown in Equation 2.15. In Equation 2.14, F_{LC} is the load cell measurement force and F_{PL} is the preload force on the load cell [16]. The third method for calculating the total pressure at the combustor exit is presented in Equation 2.16. This method does not make use of γ but does rely on a thermochemical code to obtain values for characteristic velocity and vacuum specific impulse [16].

$$F_5 = F_{LC} - F_{PL} - A_6(p_6 - p_\infty) \tag{2.14}$$

$$p_{t4} = \frac{F_5 + p_\infty A_5}{(1 + \gamma c_{D5})A_5}\left(\frac{\gamma + 1}{2}\right)^{\frac{\gamma}{\gamma - 1}} \tag{2.15}$$

$$p_{t4} = \left(\frac{c^*}{I_{sp,vac}}\right)_{th}\frac{F_5 + p_\infty A_5}{A_5 c_{D5}} \tag{2.16}$$

2.3.5 Vacuum Specific Impulse Efficiency

Equation 2.17 shows the formula for vacuum specific impulse efficiency. $I_{sp,vac}$ Efficiency is the more practical efficiency to obtain if thrust was measured during a motor firing since thrust is inherently present in the calculation of impulse unlike c^*. The theoretical value can be obtained from a thermochemical equilibrium code and Equation 2.18 [18].

$$\eta_{I_{sp,vac}} = \frac{I_{sp,vac}}{I_{sp,vac,th}} \tag{2.17}$$

$$I_{sp,vac,th} = \frac{\dot{m}_5 v_5 + p_5 A_5}{\dot{m}_5} \tag{2.18}$$

The methods presented here provide different methods of calculating $I_{sp,vac}$ following a similar pattern to the methods presented for p_{t4} in η_{c^*}. The first method, shown in Equation 2.19, makes use of γ as and Equations 2.4 and 2.5 to determine the total pressure at the aft end of the combustor. It effectively converts from c^* to $I_{sp,vac}$. The second method uses thrust measured from a thrust stand but does not use γ and is shown in Equation 2.20. It is very similar to Equation 2.18 but by using a measured value of thrust, it accounts for any losses or inefficiencies in the nozzle. The last method, shown in Equation 2.21, uses pressure measurements at the throat of the sonic nozzle and uses γ. It is rarely used since it is often difficult to obtain p_5 directly [18].

$$I_{sp,vac} = \frac{c^*}{c_{D5}} \left(\frac{2}{\gamma + 1}\right)^{\frac{\gamma}{\gamma-1}} (1 + \gamma c_{D5}) \tag{2.19}$$

$$I_{sp,vac} = \frac{F_5 + p_\infty A_5}{\dot{m}_5} \tag{2.20}$$

$$I_{sp,vac} = (\gamma c_{D5} + 1)\frac{p_5 A_5}{\dot{m}_5} \tag{2.21}$$

2.3.6 Temperature Rise Efficiency

The last efficiency parameter presented is the efficiency of total temperature rise. It has been shown by Blevins and Coleman to be the superior efficiency parameter, albeit indirect, due to its independence from flight altitude and its ability to range from 0 to 100% [16]. Equation 2.22 provides the definition for efficiency based on total temperature rise.

The total pressure at the inlet exit is calculated in a similar manner to the total pressure in

Equation 2.5. First the Mach number is calculated using Equation 2.4 using the inlet

geometry then Equation 2.23 is applied [18].

$$\eta_{\Delta T} = \frac{T_{t4} - T_{t2}}{T_{t4,th} - T_{t2}} \tag{2.22}$$

$$T_{t2} = T_2 \left(1 + \frac{\gamma - 1}{2} M_2^2\right) \tag{2.23}$$

Similar to previous efficiency measures, the value for total temperature at station 4

is usually obtained as static pressure and converted to total temperature. The direct

measurement of temperature in the combustor is difficult, therefore the methods presented

focus several ways to obtain the total temperature of the combustor without having a direct

temperature measurement at the end of the combustor. Should the temperature be

measured Equations 2.4 and 2.23 can be applied to determine T_{t4}.

The methods presented in Equation 2.24 and 2.25 makes use of γ. Equation 2.24

uses the characteristic velocity while Equation 2.25 uses the vacuum specific impulse.

Equations 2.26 and 2.27 present the method to calculate total temperature without using γ

but rely on predictions from a thermochemical code. The choice between the equations is

a matter of convenience and what measurements were taken [18].

$$T_{t4} = \gamma \left(\frac{2}{\gamma + 1}\right)^{\frac{\gamma + 1}{\gamma - 1}} \frac{c^{*2}}{R_4} \tag{2.24}$$

$$T_{t4} = \frac{\gamma}{2(\gamma + 1)} \frac{I_{sp,vac}^{*2}}{R_4} \tag{2.25}$$

$$T_{t4} = \left(\frac{T_{t4}R_4}{c^{*2}}\right)_{th} \frac{c^{*2}}{R_4} \tag{2.26}$$

$$T_{t4} = \left(\frac{T_{t4}R_4}{I_{sp,vac}^{*2}}\right)_{th} \frac{I_{sp,vac}^{*2}}{R_4} \tag{2.27}$$

2.3.7 Assumptions in the Calculation of Theoretical Parameters

The calculation of the theoretical characteristic velocity, specific impulse, and temperature as well as the ratio of specific heats, when not measured, typically has several major assumptions included in it. For modern engineering programs, thermochemical equilibrium codes and combustion simulation software is used to determine the propellant properties which include the characteristic velocity. Most analyses, save for highly specialized and expensive 2D and 3D codes, make several broad assumptions about the simulated combustion chamber and the nature of the combustion [2, 26].

The assumptions typically include, a reduced 1D modeling of the combustion chamber and combustion gas with its properties. Not all possible combustion products are typically used with only the most major on a mass or mole fraction basis being tracked throughout the simulated burn [2, 26].

When the combustion products pass through a nozzle, assumptions on the nature of the chemical equilibrium throughout are made. Assuming a frozen flow holds the mixture constant throughout the travel through the nozzle while the equilibrium assumption posits that the mixture reacts with itself throughout the nozzle to keep itself in a thermochemical

equilibrium. Reality usually lies in the middle of the two assumptions once all real-world effects are considered [2, 26].

The assumptions make most predictions of the theoretical characteristic velocity an ideal limit. Not all predictions accurately model or model at all the heat losses to of the motor to the propellant and the surroundings of the motor. Lost heat reduces motor performance and will lead to an overestimation of the performance parameters. Nonetheless the predictions are still useful as an upper limit for motor performance and as a comparison for the measured performance of a motor [2, 26].

2.4 Burning Rate Measurement

Burning rate, or regression rate, is a critical parameter for fuel development of SFRJs, solid rockets, and hybrid rockets. The burn rate equation, usually as a function of pressure, oxidizer flux rate, and/or temperature, governs how quickly the propellant burns which in turn adds energy and mass to the combustion chamber. The burning rate is a function of propellant composition which leads to an exploration of formulations to optimize performance without sacrificing desirable mechanical, storage, and plume signature properties [2].

2.4.1 Burning Rate Measurement Techniques

A variety of methods exist to determine the burning rate of solid propellants. They can broadly be separated into two major categories: direct and indirect measures of web displacement with time. [20].

The direct methods, such as ultrasound and x-ray, observe the burning surface directly. The X-ray method project X-rays through the propellant as it burns. They are captured by a screen or sensor where they are captured as an image. From a time history of images, a burn rate can be calculated [27]. The ultrasonic method passes ultrasonic vibration through the propellant as it burns. The ultrasound echoes off the burn surface. The time it takes to echo is proportional to the web thickness remaining. From a time, history of echoes a burn rate can be calculated [28]. Both methods require specialized equipment and setup [27, 28].

In the indirect method, the burn rate is taken to be the amount of web burned over the burning time of the motor as shown in Equation 2.28. The web is the linear amount of solid propellant measured normal to the surface of the propellant. Most methods produce an average burning rate since an instantaneous burning rate is difficult and expensive to obtain inside of a test motor. Some more advanced methods of this type include corrections based on pressure [29, 30] .

$$\bar{r} \approx \frac{\Delta(d_i/2)}{\Delta t} = \frac{w_b}{t_b} \tag{2.28}$$

One of the simplest and most common grain types is the center perforated grain. It has seen the most use in SFRJs and in the experiments presented in this work [1]. The equation for web thickness for this is presented in Equation 2.29. This form uses the measured mass burned (m_b), the mass of the propellant available before the burn (m_p), and the inner and outer diameters of the propellant (d_i, d_o) [31].

$$w_b = \frac{1}{2}\sqrt{\left(\frac{m_b}{m_p}\right)(d_o^2 - d_i^2) + d_i^2} - d_i \qquad (2.29)$$

This equation was derived assuming that only the center perforation of the grain was burned and that the burning was even down the length of the grain. The first assumption is valid for motors with thin webs relative to their lengths. The second assumption is acceptable for treating the calculated web thickness as the average web thickness burned throughout the grain.

The other category of methods for the determination of burn rate are the mass balancing methods. An example of such a method is shown in Equation 2.30. These methods generally include elements of the desired burn rate equation in them, such as the pressure coefficient a, to make estimates of the mass flow throughout the motor. They are more complicated then than the thickness versus time methods but boast greater accuracy and can account for effects not captured in the prior methods [30].

$$\dot{r}_b = \frac{w_b \overline{P_{t4}}}{a \int_0^{t_b} P_{t4} \, dt} \qquad (2.30)$$

2.4.2 Burning Time Determination

Critical to the determination of burning rate, is the determination of the burning time. The burning time is the time period from which the entirety of the surface of the grain is considered to be ignited until the flame dies out. The challenge in determining burn time comes from determining where on a pressure trace the beginning of the burn and end of the burn are located [29].

25

A variety of methods exist with the most common for starting time being constant percentage of maximum pressure, usually 10%, but 5%, 15%, 20%, and 25% are also common. The end has more variation using the same percentages of maximum pressure and the tangent bisector method. The tangent bisector method, along with the percentage of maximum pressure method, are shown graphically on a notional pressure trace in Figure 2.6 [29].
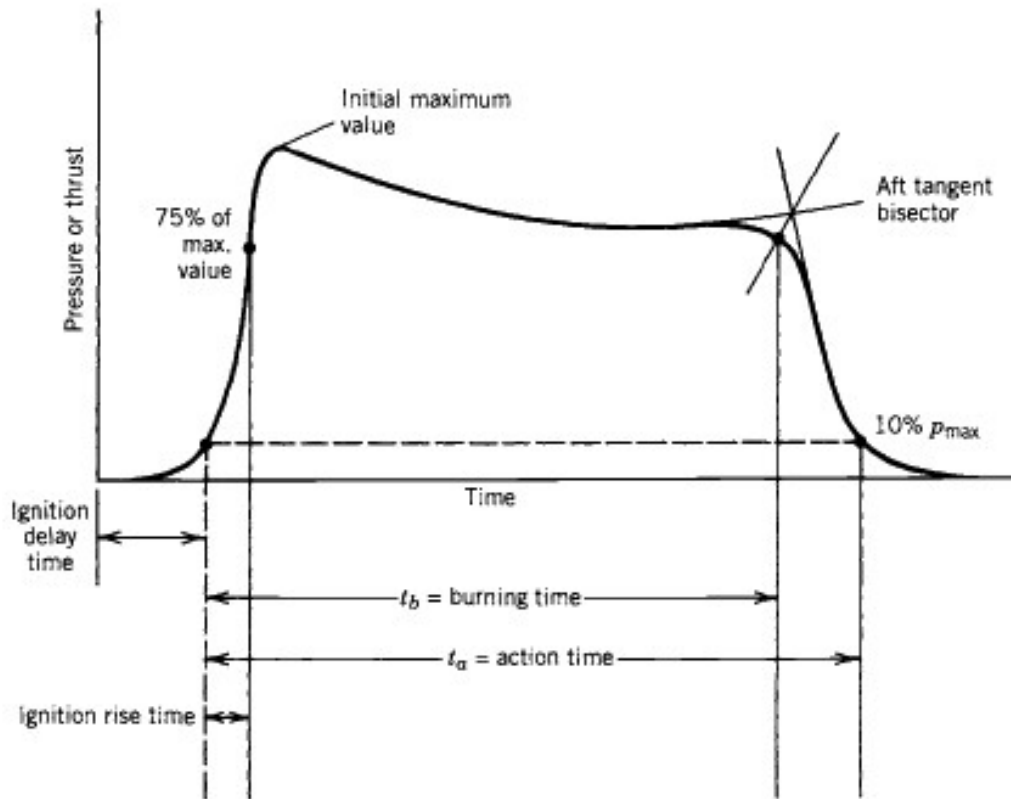
Figure 2.6: Aft-Tangent Bisector Method for Burn Time Determination [2]

The tangent bisector method draws two tangent lines on the either side of the hump towards tail off. Where the tangent lines intersect, another line is drawn to bisect them. The bisection line intersects the pressure trace. The intersection of the tangent bisector line

26

and the pressure trace is considered stop point for the burn process. This is an attempt to account for the transient flow of gases out of the combustor after the grain has been burned up [29].

More methods exist such as taking the time where the second derivative of pressure (d^2p/dt^2) is zero, the Brooks method involving the computation and comparison of pressure integrals, and the Hessler-Glick method using the sign of second derivative of pressure to mark time points [30].

Accurate determination of the burning time is essential since it scales how quickly or slowly the web is perceived to be burned. Mathematically this can be seen in Equation 2.28 where the web thickness is divided by the time of the burn. A complicating factor in all burn time methodologies is accounting for ignition and flame out transients. By accounting for, or not accounting for, these factors uncertainty in the burn time is introduced. From these factors, there exists a conceptual bias in when the start of the burn and end of the burn are taken as shown in Figure 2.7
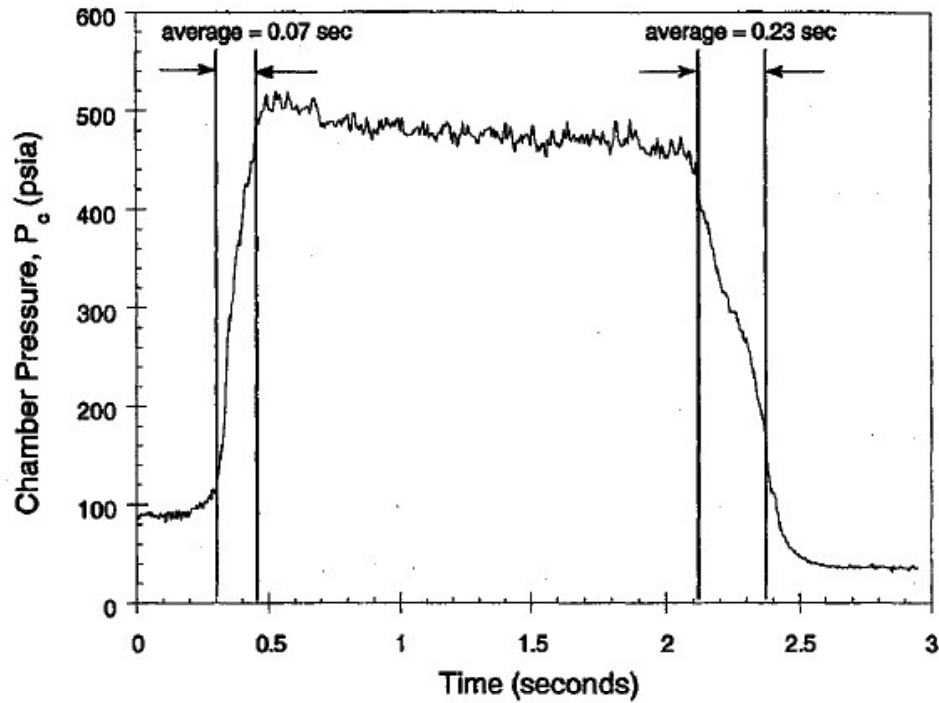
Figure 2.7: Burn Time Conceptual Bias [32]

Counter-intuitively, extending the length of a test burn does not necessarily decrease in uncertainty in the burning rate. It does decrease the relative uncertainty in burn time. The burning rate is taken to be an average of the web burned over time, however the burning rate changes as a function of time due the ever shifting burn surface. The average introduces a conceptual bias. A long burn time magnifies the conceptual bias due to nonlinearities in the burning rate. Depending on the other uncertainties inherent in the test, there is an optimum length for a test burn [32].

2.4.3 Burning Rate Equations

A burning rate equation is usually just a curve fit of driving factors for the burning rate. The constants for the chosen fit are typically determined from multiple test firings at

different the conditions. The conditions are chosen to explore the major factors in the burning rate equation. It is possible to determine the burning rate from a single test, but this is usually difficult and inaccurate [29]. The equations presented here are shown in Table 2.2.

There are many kinds of burn rate Equations than can be used. Solid rocket motors have generally used St. Robert's Law. Equation 2.31 shows this a is the burn rate coefficient, n is the burn rate exponent, and p is the pressure of the propellant during the burn [2].

Another common form of burning rate, widely used in hybrid rocketry in which SFRJs are very similar, is shown in Equation 2.32 where b is the hybrid burning rate coefficient, G is the oxidizer mass flux rate, and q is the oxidizer mass flux coefficient [2]. More discussion on the topic of regression rate is presented in 2.4 Burning Rate Measurement.

Unlike ramjets, solid rocket motors do not have an oxidizer flow through the grain. It is not uncommon for ramjet propellants to not burn by themselves invaliding St. Robert's Law. Propellants that require an oxidizer yield themselves to burning equations that contain an oxidizer mass flux term such as the one shown in Equation 2.32. The choice of burning equation is often dependent on scaling of test motors to full size motors. A wide selection of equations exists some including dependencies on length and diameter of the grain, pressure, mass flux, and temperature of incoming air to name a few. Analytical attempts at identifying burning rate equations exist but in general most burning rate equations are type of regression fits. It has been found that burning rate equations including pressure dependence tend to scale to larger motors better than those that do not. For

working within the same scale, burning rate equations with a dependence on flux perform the best [33].

Previous work by Whitehead has proposed a burning rate equation in the form of a product of pressure and oxidizer flux for a mixed oxidizer hybrid motor. Equation 2.33 shows the proposed burn rate equation [34]. Like a solid rocket motor, an increase in pressure causes an increase in the regression rate but stopping the oxidizer mass flow would extinguish the motor which is the case for the ramjet motors in this study. The coefficient a and the exponents n and q are experimentally determined values specific to the propellant. The coefficient a can show dependency on temperature also [35, 2].

Work by Mascaro has investigated a new form of regression rate equation, shown in Equation 2.34, in the form of a linear combination of St. Robert's Law (Equation 2.6) and the hybrid burring rate equation (Equation 2.7). Equation 2.32 was to be used along the bore of fuel grain with Equation 2.31 to be used for the ends of the grain where there is negligible oxidizer flow. This form does not have the advantage of forcing burn rate to zero when the oxidizer flux is set to zero as the pressure term can produce mass flow through self-deflagration like a solid rocket motor. Nonetheless, this form has seen some utility in accurately modeling hybrid motor regression rates [35].

A common form of burn rate equation that is used is derived from convective theory. It governs the burn rate through convective and radiative heat transfer in the boundary layer of the flame next to the grain in the motor. This analysis introduces a dependency on the mass transfer number (B) which is not seen in the other forms presented. The equation resulting from this modeling approach and the work done by Raghunandan et Al is shown in Equation 2.35 [36].

For small scale SFRJs it has been found that generic relation for burning rate in form shown Equation 2.36 is adequate. The work by Netzer and Gany focused on very small SFRJs with inner diameters of 10 mm (0.39 in) but the results of the study have applicability to the ramjets of the scale presented in this work. Of interest in this form is the lack of a pressure dependency. It was found that for the chamber pressures in their work, which were in the range of 0.3-1.0 MPa (44-145 psi), that pressure was found to have "practically no measurable effect on the fuel regression rate." They also introduce an area ratio term not commonly seen [37]

Examples of propellants which have seen use in SFRJs that exhibit dependencies on more that just pressure, as is common in a solid rocket motor, are those for the common fuels polymethyl methacrylate, hydroxyl-terminated polybutadiene, and polyethylene more commonly known by their acronyms PMMA, HTPB, PE. All three are characterized well by burn rate equations including dependencies in pressure, temperature, and mass flux. The equations for each are shown respectively in Equations 2.37, 2.38, and 2.39 [36, 38, 39].

Table 2.2: Burn Rate Equation Summary

Equation Number	Equation	Typical Usage	Minimum Number of Tests	Citation(s)
(2.31)	$\dot{r} = ap^n$	St. Roberts Law	2	[2]
(2.32)	$\dot{r} = bG_{ox}^q$	Hybrid Rockets	2	[2]
(2.33)	$\dot{r} = aP^n G_{ox}^q$	Hybrid Rockets	3	[2] [34] [35]
(2.34)	$\dot{r} = aP^n + bG^q$	Hybrid Rockets	3	[35]
(2.35)	$\dot{r} = aG^q P^n B^{0.23}$	Derived from heat transfer	4	[18]
(2.36)	$\dot{r} \propto G^{0.9-1.0} T_a^{0.95} \left(\dfrac{A_p}{A_{in}}\right)^{0.5}$	Small scale ramjets	3	[37]
(2.37)	$\dot{r} = cP^{0.51} G^{0.41} T^{0.34}$	PMMA	4	[36]
(2.38)	$\dot{r} = 4.44 \times 10^{-5} G^{0.53} P^{0.33} T_t^{0.71}$	HTPB	4	[38]
(2.39)	$\dot{r} = 2.78 \times 10^{-3} P_c^{0.8} G_a^{0.35} T_a^{0.36}$	PE	4	[39]

2.5 Uncertainty Analysis Overview

All measurements contain errors. There are no perfect measurements that have no errors associated with them. Therefore, it is critical to quantify the uncertainty associated with the measurements and establish a confidence interval for it. The most common confidence interval chosen, and the one used in this analysis, is the 95% confidence interval [40]. This section establishes an overview of the uncertainty analysis process beginning with the Taylor Series Methods, the standard method, and concludes with the Monte Carlo Method.

There are two general categories of elemental error sources that are introduced into measurements: random (ε) and systematic errors (β). The sum of the errors is δ. These are shown graphically in Figure 2.8. An example random error would be white noise in a measurement signal. The magnitude of a random error is different every time it is measured. Systematic errors are errors that do not vary during the measurement period. They can be constant or scale with the true value, but for the same measured value, the same systematic error would be obtained. A bias is a form of systematic uncertainty. An example would be the improper installation of a sensor or the uncertainty in measurements from a pressure transducer. It is common for systematic uncertainties to remain the same between data points, but not necessarily between separate runs [40].
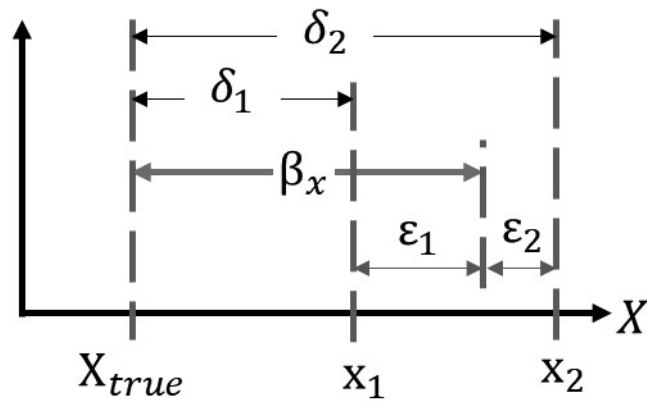
Figure 2.8: Errors in Readings of a Variable [41]

2.5.1 Uncertainty of a Single Measured Variable

Consider a series of N measurements of a single variable X. The sample standard deviation is shown in Equation 2.40 where the average of the measurements $\bar{X}$ is given by Equation 2.41 [40].

$$S_X = \left(\frac{1}{N-1} \sum_{i=1}^{N} (X_i - \bar{X})^2 \right)^{\frac{1}{2}} \tag{2.40}$$

$$\bar{X} = \frac{1}{N} \sum_{i=1}^{N} X_i \tag{2.41}$$

Equation 2.42 gives the formula the standard deviation of the mean, $\bar{S}_X$. The standard deviation of the mean represents the standard deviation of a mean taken from data that has a Gaussian distribution, S_x, embedded within it. [40].

$$\bar{S}_X = \frac{S_X}{\sqrt{N}} \tag{2.42}$$

For Gaussian distributed random errors, the random expanded uncertainty of a single variable is given by Equation 2.43 and the expanded random uncertainty of the mean is given by Equation 2.44. The expanded uncertainty includes the confidence interval whereas the uncertainty without a confidence interval is called the standard uncertainty. Capital letters denote expanded uncertainties. t is from the student's t distribution [40]. For this analysis, t is always equal to 2 to obtain a desired 95% confidence interval since the degrees of freedom, v, are always greater than 9.

$$P_X = tS_X \tag{2.43}$$

$$\bar{P}_X = t\bar{S}_X \tag{2.44}$$

The scatter in a measured variable is only a result of the random errors. The systematic errors are constant across repeated measurements, they do not affect the scatter. This makes the standard deviation of a repeated measurement an appropriate measure of random uncertainty while the systematic uncertainty must still be made.

From the random uncertainty and systematic uncertainty (B_x) a total uncertainty can be obtained. This is shown in Equation 2.45 for the single measured variable X and in Equation 2.46 for the mean. The systematic errors do not change with repeated measurements, therefore there is no difference between the systematic uncertainty for the measurement and of the mean [40].

$$U_X = \sqrt{P_X^2 + B_X^2} \tag{2.45}$$

$$\overline{U}_X = \sqrt{\overline{P}_X^2 + B_X^2} \tag{2.46}$$

2.5.2 Uncertainty of a Result Determined from Multiple Variables

In many real-world applications, the desired information is a result, r, calculated from several measured variables $(X_1, X_2, \ldots, X_i)$, in the form of Equation 2.47. For this case, the systematic and random errors in each measured variable will contribute to an error in the result. The determination of uncertainty of the result requires an uncertainty propagation to be performed [40].

$$r = r(X_1, X_2, \ldots, X_i) \tag{2.47}$$

Following an uncertainty propagation, Equation 2.48 results for the expanded combined uncertainty. This can be broken down into its random and systematic parts [40].

$$U_r = \left(\sum_{i=1}^{N} \left(\frac{\partial r}{\partial X_i} \right)^2 U_i^2 \right)^{\frac{1}{2}} \tag{2.48}$$

Equation 2.49 shows the expanded systematic uncertainty with B_{X_i} being the systematic uncertainty for the ith variable. The first term accounts for the contribution of the expanded systematic uncertainties for each individual variable. The last term of Equation 2.51 accounts for correlated systematic uncertainties between different variables if those variables share an error source. For example, if multiple sensors were calibrated against the same standard, then a correlated systematic error would exist. [40].

$$B_r^2 = \sum_{i=1}^{N} \left(\frac{\partial r}{\partial X_i} \right)^2 B_{X_i}^2 + \sum_{i=1}^{N-1} \sum_{k=i+1}^{N} 2 \left(\frac{\partial r}{\partial X_i} \right) \left(\frac{\partial r}{\partial X_k} \right) B_{X_i X_k} \tag{2.49}$$

The random uncertainty component is shown in Equation 2.50 and takes on the same form as the expanded systematic uncertainty. It also includes a term for correlated uncertainty, however there is not an established method for estimating the magnitude of the correlated random uncertainty, and this term is usually assumed to be zero [40].

$$P_r^2 = \sum_{i=1}^{N} \left(\frac{\partial r}{\partial X_i} \right)^2 P_{X_i}^2 + \sum_{i=1}^{N-1} \sum_{k=i+1}^{N} 2 \left(\frac{\partial r}{\partial X_i} \right) \left(\frac{\partial r}{\partial X_k} \right) P_{X_i X_k} \tag{2.50}$$

Equation 2.50 is not the only way to calculate the contribution from random uncertainty. The random uncertainty of a result may also be estimated through a more direct calculation method. For cases of multiple measurements at the same steady state condition, the result r is computed for each set of measurements of the variables resulting in a set of results. Equations 2.43 and 2.44 are then used to estimate the random uncertainty. The resulting expanded uncertainties are shown in Equations 2.51 and 2.52. This methodology does not produce the same results as Equation 2.50 if correlated random uncertainties are present [40].

$$U_r = \sqrt{P_r^2 + B_r^2} \qquad (2.51)$$

$$\overline{U}_r = \sqrt{\overline{P}_r^2 + B_r^2} \qquad (2.52)$$

2.5.3 Uncertainty Percentage Contribution

Uncertainty Percentage Contributions (UPCs) can be calculated to provide an assessment of the relative contributions of elemental uncertainty estimates to the total uncertainty estimate They are a value ranging from 0% to 100% that demonstrates how large of a contribution to the total uncertainty a specific uncertainty was. The sum of all UPCs is unitary. Equations 2.53 shows the UPC for uncertainty an expanded uncertainty of a variable part of the resultant variable. Equations 2.54 and 2.55 show the UPCs for systematic and random uncertainties of each variable [40].

$$UPC_{U_i} = \frac{\left(\frac{\partial r}{\partial X_i}\right)^2 (U_i)^2}{(U_r)^2} \cdot 100 \tag{2.53}$$

$$UPC_{B_{X_i}} = \frac{\left(\frac{\partial r}{\partial X_i}\right)^2 (B_{X_i})^2}{(U_r)^2} \cdot 100 \tag{2.54}$$

$$UPC_{P_{X_i}} = \frac{\left(\frac{\partial r}{\partial X_i}\right)^2 (P_{X_i})^2}{(U_r)^2} \cdot 100 \tag{2.55}$$

Equations 2.56, 2.57, and 2.58 show the UPCs of the mean for the expanded uncertainty, systematic uncertainty, and random uncertainty. If correlated uncertainty terms exist, relevant UPCs also exist and can be constructed in a similar manner to the ones presented here [40].

$$\overline{UPC}_{U_i} = \frac{\left(\frac{\partial r}{\partial X_i}\right)^2 (\overline{U}_i)^2}{(\overline{U}_r)^2} \cdot 100 \tag{2.56}$$

$$\overline{UPC}_{B_{X_i}} = \frac{\left(\frac{\partial r}{\partial X_i}\right)^2 (B_{X_i})^2}{(\overline{U}_r)^2} \cdot 100 \tag{2.57}$$

$$\overline{UPC}_{P_{X_i}} = \frac{\left(\frac{\partial r}{\partial X_i}\right)^2 (\overline{P}_{X_i})^2}{(\overline{U}_r)^2} \cdot 100 \tag{2.58}$$

With the calculation of the UPCs for an experiment, it is possible to identify the dominant uncertainty sources which can then be minimized if reasonable. It is wise to perform an UPC analysis beforehand to identify which are the largest sources of uncertainty in an experiment and build it appropriately [40].

2.5.4 Monte Carlo Method

The Monte Carlo method (MCM) is an elegant and powerful method for uncertainty analysis. The method is general enough and powerful enough to handle uncertainty of a single variable up to very complex nonlinear equations. With the MCM, the uncertainty analysis of a result determined from several variables the process is straight forward. Unlike the previous method, the MCM is a numerical method. The process is graphically depicted in Figure 2.9 [40].

First the data from the variables are taken to be the $(X_{m,i})$. Next each of the elemental random (ε_{ia}) and systematic errors (b_{ib}) are input and assumed to be the standard deviation of a probability distribution of the analyst's choice. For example, random uncertainty is best handled with the Gaussian distribution. If one believes that the uncertainty is random within a set bound a rectangular distribution is appropriate. A triangular distribution allows for the setting of the mode and end points [40].

The MCM enters the main loop where at each iteration an uncertainty from each elemental uncertainty distribution is assigned to the measured variable at that iteration. Correlated error can be introduced here easily by having the same error added to multiple variables. The result of interest, r, is then calculated using the modified variables. This is done in a loop until the standard deviation of the result (u_r) has converged to an acceptable level. If the result is a collection of points, such as a pressure trace, the random uncertainty can be taken directly from the data (ε_r) instead of using elemental random uncertainties as shown in Equation 2.59. It is added directly to the result. [40].
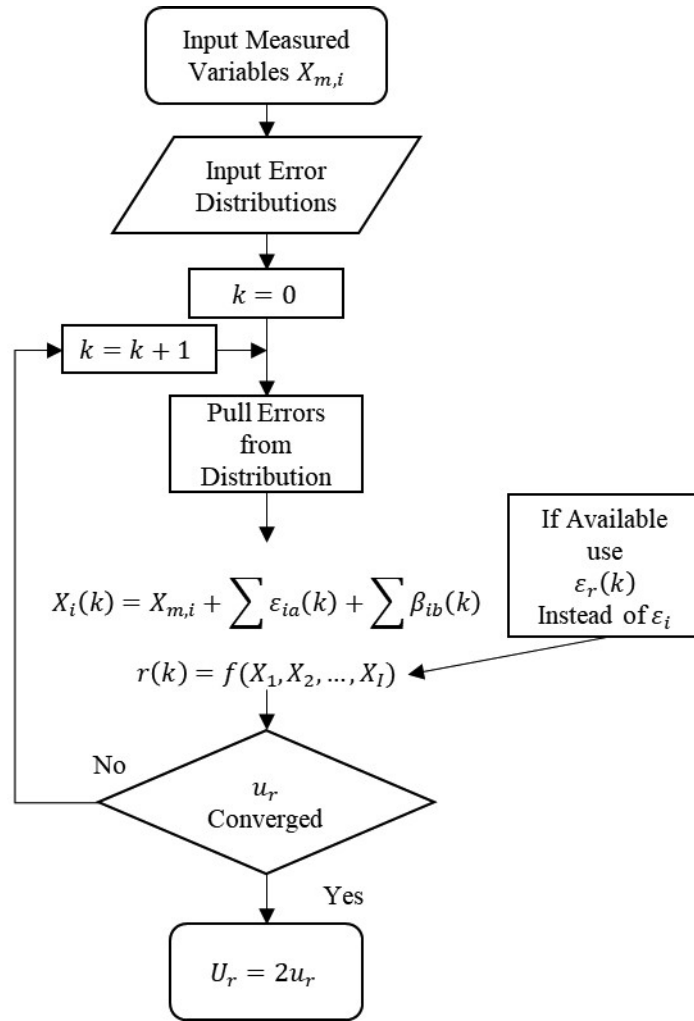
Figure 2.9: Monte Carlo Method

$$\varepsilon_r = \sqrt{\frac{1}{N-1}\sum_{i=1}^{N}(r_i - \bar{r})^2} \tag{2.59}$$

The output of the MCM process returns a distribution of values for the result r. This distribution may not necessarily match any common probability distribution. It is possible for it to be skewed such as in the example Figure 2.10 or multimodal. In these cases, it is normal for the expanded uncertainty bounds to be chosen to be probabilistically

symmetric so that a desired coverage interval is obtained. The upper and lower confidence intervals are chosen to capture the same probability from the distribution. The MCM does not force the result to conform to a Gaussian or t distribution unlike the uncertainty analysis presented in the previous section. In principle this will produce the most accurate result. The TSM assumes all distributions are normal which is nonphysical for many systems [40].
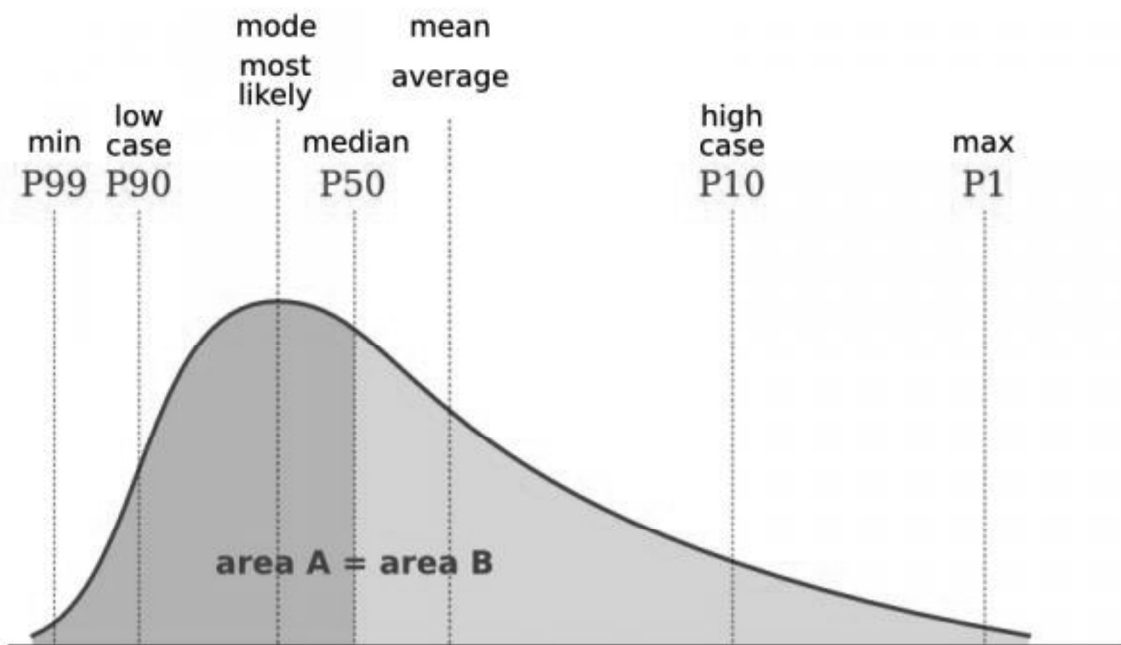
Figure 2.10: Skewed Distribution [42]

2.5.5 Uncertainty Percentage Contribution for Monte Carlo

Like with the Taylor Series Method, an uncertainty percentage contribution can be calculated. Like the TSM, it ranges from 0% to 100%. In the MCM the equations for uncertainty are not available. Instead, the UPC is taken as the difference of the squares of the expanded uncertainty of the result and the expanded uncertainty of the result when the

uncertainty of interest is set to zero all over the square expanded uncertainty of the result. The Monte Carlo UPCs may be seen in Equation 2.60 – Equation 2.65.

$$UPC_{U_i} = \frac{(U_r)^2 - \left(U_{r,U_i=0}\right)^2}{(U_r)^2} \cdot 100 \tag{2.60}$$

$$UPC_{B_{X_i}} = \frac{(U_r)^2 - \left(U_{r,B_{X_i}=0}\right)^2}{(U_r)^2} \cdot 100 \tag{2.61}$$

$$UPC_{P_{X_i}} = \frac{(U_r)^2 - \left(U_{r,P_{X_i}=0}\right)^2}{(U_r)^2} \cdot 100 \tag{2.62}$$

$$\overline{UPC}_{U_i} = \frac{(\overline{U}_r)^2 - \left(\overline{U}_{r,\overline{U}_i=0}\right)^2}{(\overline{U}_r)^2} \cdot 100 \tag{2.63}$$

$$\overline{UPC}_{B_{X_i}} = \frac{(\overline{U}_r)^2 - \left(\overline{U}_{r,\overline{B}_{X_i}=0}\right)^2}{(\overline{U}_r)^2} \cdot 100 \tag{2.64}$$

$$\overline{UPC}_{P_{X_i}} = \frac{(\overline{U}_r)^2 - \left(\overline{U}_{r,\overline{P}_{X_i}=0}\right)^2}{(\overline{U}_r)^2} \cdot 100 \tag{2.65}$$

2.5.6 Uncertainty of Regressions

The process for the MCM uncertainty of linear and multiple linear regressions are fundamentally the same process as MCM for as any other equation. Figure 2.11 outlines the process. It is possible to perform an uncertainty analysis with the TSM, but it is much more complicated in comparison [43].

For the MCM, measured data points $(X_{m,i}, Y_{m,i})$ and their elemental error distributions are provided to the routine. In each iteration, the data points are perturbed and then used to calculate regression constants which are the slope and intercept for a

simple linear regression. A new line is constructed with the new regression coefficients and fed the independent data set $(X_{m,i})$ to produce new outputs $(Y_{new,i}(k))$. This is repeated until the new outputs at each data point have converged. Following the closure of the main loop, an uncertainty interval in Y is constructed at each of the data points using the standard deviation in the new outputs $Y_{new}(k)$ [43].

This method produces a different kind of uncertainty than the statistical method. The statistical method produces uncertainty values on the regression constants themselves whereas this method produces uncertainty bands at each point. The statistical method uses the residuals and standard error to calculate the uncertainty values without directly considering the uncertainty in each data point. The statistical method has been proven to be inferior to the MCM method for regressions in the research done by Brown. The statistical method is better suited as an indicator of the goodness of fit but a poor indicator of the uncertainty [43].
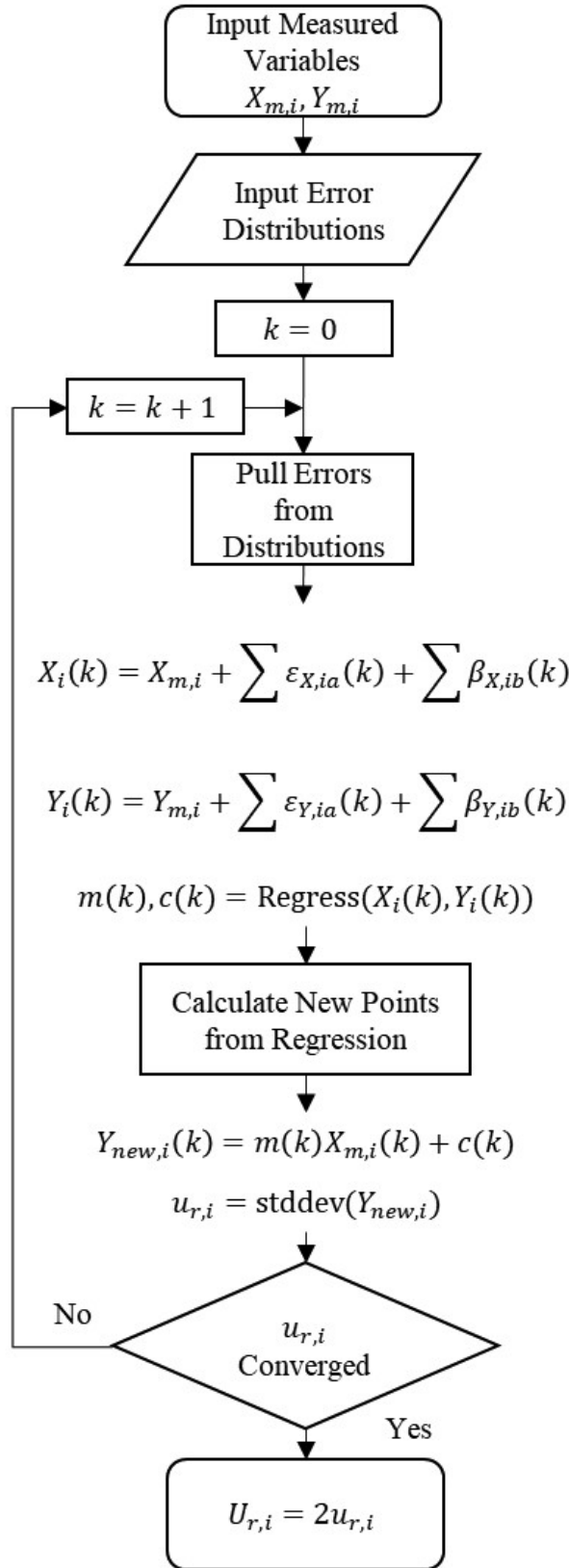
Figure 2.11: Monte Carlo Flowchart for Simple Linear Regressions

44

2.6 Assessment of SFRJ Analysis and Uncertainty Methodologies

The goal of the testing that was occurring at the PRC was to characterize the performance parameters of characteristic velocity (c^*), combustion efficiency (η_{comb}), thrust (F), specific impulse (I_{sp}), and vacuum specific impulse ($I_{sp,vac}$) for SFRJ propellants. Data from this testing was provided for the analysis presented in this thesis. Not all of the measurements discussed in the previous sections were taken, such as a direct thrust measurement. This limits the selection of methods to what data was available and which were the best methods within that subset.

The fuel testing occurred in a connected pipe SFRJ. The test article was not mounted to the thrust load cells on the thrust stand at the PRC. Static pressures at the air inlet, combustor head, and combustor end were measured. Pressure at the nozzle throat was not measured. No temperatures in the combustor or nozzle were measured.

Table 2.3 shows a summary of the different methods that may use in the determination of the performance parameters with their advantages and disadvantages. The chosen methods for the analysis are shown in highlighted in green. The decision for each was determined by the test data that was provided for this thesis.

Table 2.3: Summary of Performance Parameter Methods

Parameter	Equation	Advantages	Disadvantages	Citations
F	2.1	Most Direct Mathematical Form	Hard to measure variables directly	[19]
	2.2	Easy to measure pressure	Needs p_{t4} and γ	[19]
	2.14	Direct measurement, avoids γ	Requires a thrust stand	[18] [16]
p_{t4}	2.5	Uses measured pressure	Needs γ	[2] [18] [16]
	2.15, 2.16	Uses thrust stand data	Requires a thrust stand, γ	[18] [16]
I_{sp}	2.7	Direct	Magnifies errors in thrust	[2]
	2.8	Direct	Magnifies errors in thrust	[2]
$I_{sp,vac}$	2.19	Uses c^*	Magnifies errors in c^*	[18]
	2.20	Direct using thrust stand	Requires a thrust stand	[18]
	2.21	Direct using p_5	Hard to measure p_5	[18]
c^*	2.9	Uses measured quantities	Need p_{t4}, mass flows	[2]
	2.11	Uses only temperature measurement	Needs T_{t4}, R and γ	[2] [18]
η_{comb}	2.13	Low uncertainty with measured p_4	Not as reliable or broad as $\eta_{\Delta T}$	[18] [16]
	2.17	Low uncertainty with thrust stand	Requires a thrust stand to be good	[18] [16]
	2.22	Superior Efficiency measure	Hard to measure temperatures	[18] [16]

A burn rate equation was chosen based on a curve fit and its goodness of fit to the available data. A three-term model in combustor pressure, air mass flux, and air temperature was desired. This is the standard form used for propellants in literature.

A summary of the two uncertainty analysis methods is shown in Table 2.4. The MCM was chosen for the uncertainty analysis in this work. This choice was based on the relative ease to implement compared to the TSM. This was especially important for the uncertainty of the multiple linear regression required for the burn rate equation.

Table 2.4: Summary of Uncertainty Methodologies

Methodology	Advantages	Disadvantages	Citations
Taylor Series Method	Is the standard analytical method for uncertainty analysis	Complicated to implement for complex problems Assumes or fits normal distributions for all uncertainties Determination of correlated uncertainties is nontrivial Uncertainty of linear regressions is complicated process	[40]
Monte Carlo Method	Simple to implement Handles all forms of distribution of inputs and outputs easily Handles correlated uncertainties easily Handles linear regressions easily compared to TSM	Requires a computer with adequate processing power (not much of an issue today for most problems) Calculating UPCs are complicated	[40] [43]

CHAPTER 3

EXPERIMENTAL SETUP

The setup of the experiment concerns the layout and data acquisition from the test article. Solid fuel grains were supplied for testing on the PRC's connected pipe ramjet. The data acquired during a test firing requires a pretest and posttest analysis to determine the results of the test. The process for this is described and results of the process presented in subsequent sections.

3.1 Propellant and Test Conditions

Two formulations of propellants were tested. Due to the sensitive nature of the recipes, the propellants will be identified by the labels A and B. The burn rate equations of the propellants were desired and thus a test matrix was devised that varied the mass flow and temperature of the air. A factorial experiment with two replications was used for a total of 8 tests for each propellant for a total of 16 tests overall. Figure 3.1 shows the test matrix with the set points and the designation for the tests. The test designations provided in Figure 3.1 will be used throughout this thesis to identify a particular test. The designations list the propellant used with the subscript referring to the high (H) or the low state (L) of the mass flow and temperature, in that order, with the number indicating the replication.

Temperature [°F]

	0.146	0.238
800	A_{LH1} A_{LH2} B_{LH1} B_{LH2}	A_{HH1} A_{HH2} B_{HH1} B_{HH2}
662	A_{LL1} A_{LL2} B_{LL1} B_{LL2}	A_{HL1} A_{HL2} B_{HL1} B_{HL2}

Mass Flow [lb$_m$/s]

Figure 3.1: Test Matrix with Test Designations

3.2 Overview of UAH PRC Heated Air Flow Facility

A schematic of the facility for pipe connected ramjet testing is shown in Figure 3.2. The major components and measurements are shown. Dehumidified compressed air is stored in tanks. During testing, air from the tanks is passed from the tanks to the test article. An inline heater is used to preheat the air before introduction into the test article. The mass flow of the air is measured by a Coriolis flow meter before the heater and by a sonic nozzle after the heater. Both should produce the same mass flow by continuity throughout the system. Thermocouples exist in the heater and immediately before the test article for control of the incoming air temperature. A hydrogen/oxygen igniter is used to start the burn. The hydrogen and oxygen lines have their own pressure transducers and orifice plates for control. The test article, the ramjet itself, has two pressure transducers. One is located on the head end before fuel grain and the other is located on the aft end immediately before the nozzle [44].
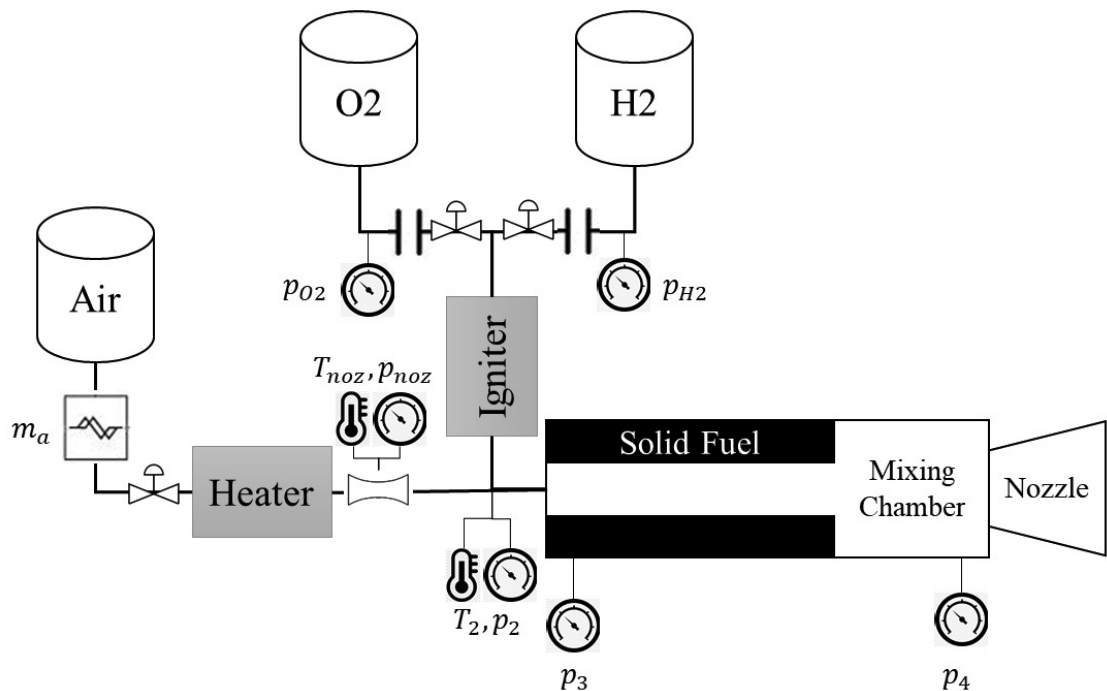
Figure 3.2: SFRJ Functional Drawing

The test stand is controlled remotely from a room away from the test cell. Commands are issued through National Instruments LabView to a National Instruments PXI chassis which controls the various systems. The chassis has pressure and temperature cards installed to accurately capture the test data.

Many transducers were mounted on the test cell, but only the few are relevant ones are discussed here. Complete schematics may be seen in Appendix A.

The port connector transducer (p_2), head end transducer (p_3), and aft end transducers (p_4) are near one another and report similar pressures. This was used to cross check the aft end transducer which tended to clog with solid combustion products. If it was clogged for a test, the head end pressure was used instead.

The port temperature (T_2) was taken to be the temperature of the air (T_a).

3.3 SFRJ Test Article

The ramjet test article is shown in Figure 3.3. It is attached to a sled which is strapped to a concrete wall of the PRC test cell. The heater for the system is stored on the platform underneath the test article. A blue diverter valve may be seen immediately before the head end of the motor. The port temperature and pressure sensors are located between the diverter valve and head end of the ramjet.
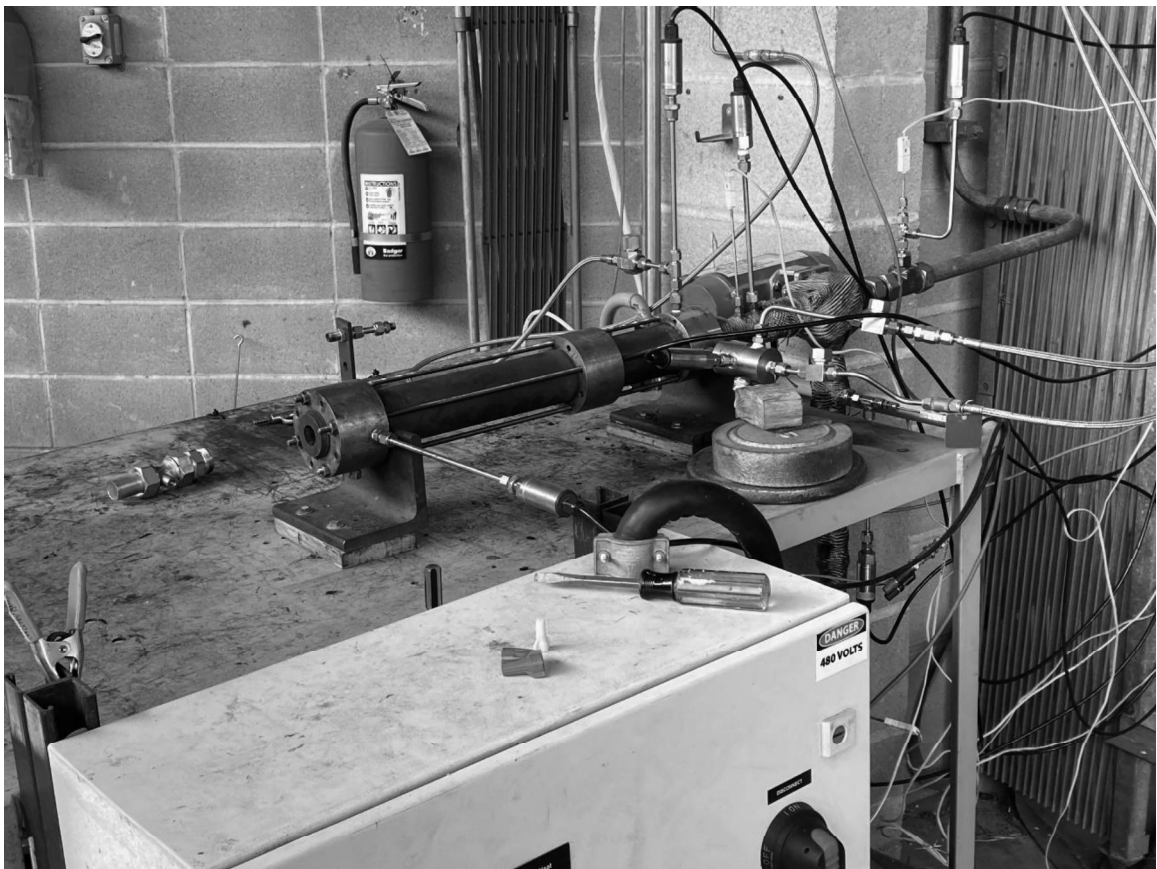
Figure 3.3: Ramjet Test Article

A cross section of the test article is shown in Figure 3.4. The test article is comprised of the two major sections, the combustion chamber, and the mixing chamber,

connected by a coupler and capped on both ends. The combustion chamber and mixing chamber are made of carbon steel. The head end fits a 1" NPT pipe for connecting to the test cell air supply. The head end also accepts an insert, shown in red, which is either made of phenolic or stainless steel. The insert has slots to allow the igniter gases to enter the combustion chamber and for a pressure tap to be mounted on the head end. Care has been taken to ensure the correct clocking of the insert during testing. The aft end accepts a nozzle. The nozzles are made of copper with a several nozzles being made with a variety of throat sizes. The nozzles have a groove to allow gasses to reach the aft end pressure transducer.
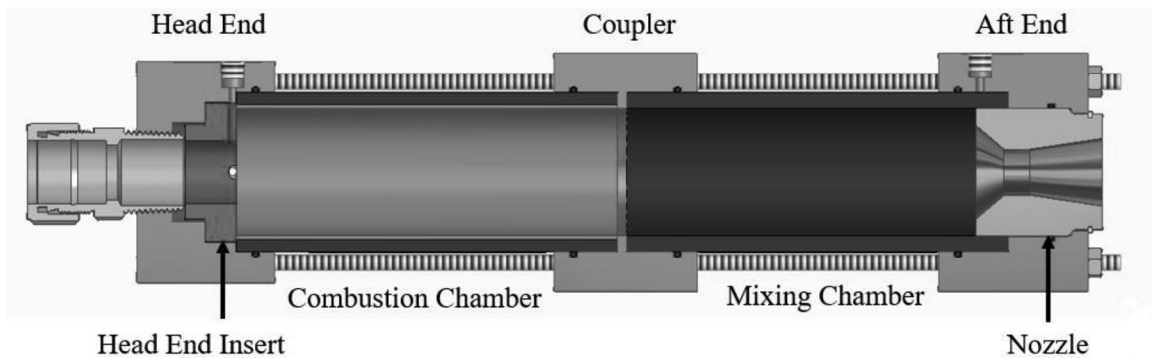
Figure 3.4: Test Article Cross Section

The mixing chamber has a phenolic liner to protect the steel. It is assumed that the phenolic does not contribute to the combustion process.

The fuel grain is composed of a phenolic liner and the propellant cast within it. The propellant is shown in orange in Figure 3.4. As with the mixing chamber, the phenolic is assumed to not participate in the combustion process. Usually, the propellant is not completely spent after a test, so none of the case was exposed.

The igniter is shown in the head end test article in Figure 3.3 and Figure 3.5. It uses hydrogen and oxygen to produce a fuel rich flame for starting the combustion process in the test article. The hydrogen and oxygen lines include a sonic orifice for control of flow. The igniter flame is started by an automotive style spark plug which can be seen as the white protrusion. The igniter contributes mass flow to the ramjet during its brief firing window.
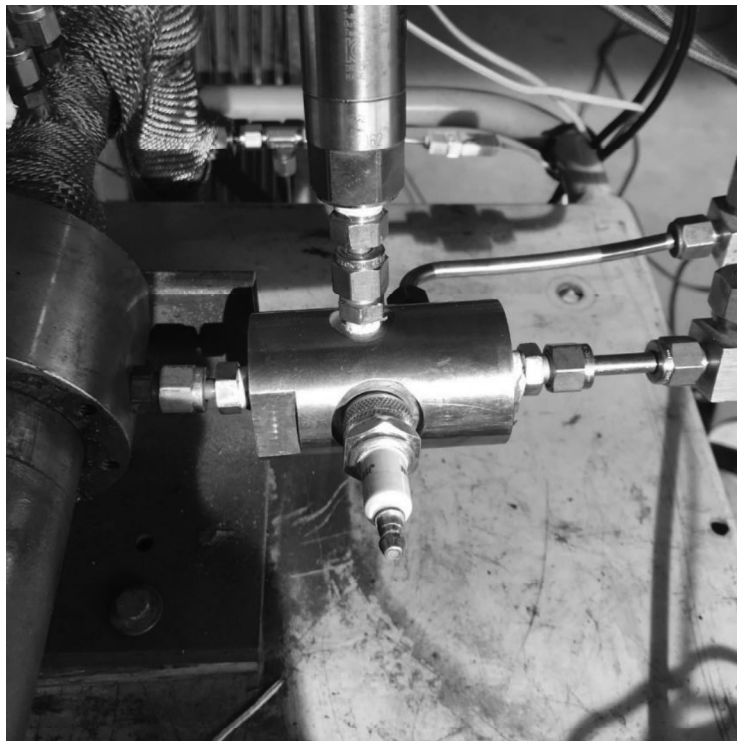
Figure 3.5: Igniter

3.4 Test Sequencing

The test sequence is shown graphically in Figure 3.6. The first sequence is the warmup phase. This time is used for the heater to increase up to temperature. Air is passed through the heater and exhausted to the atmosphere.
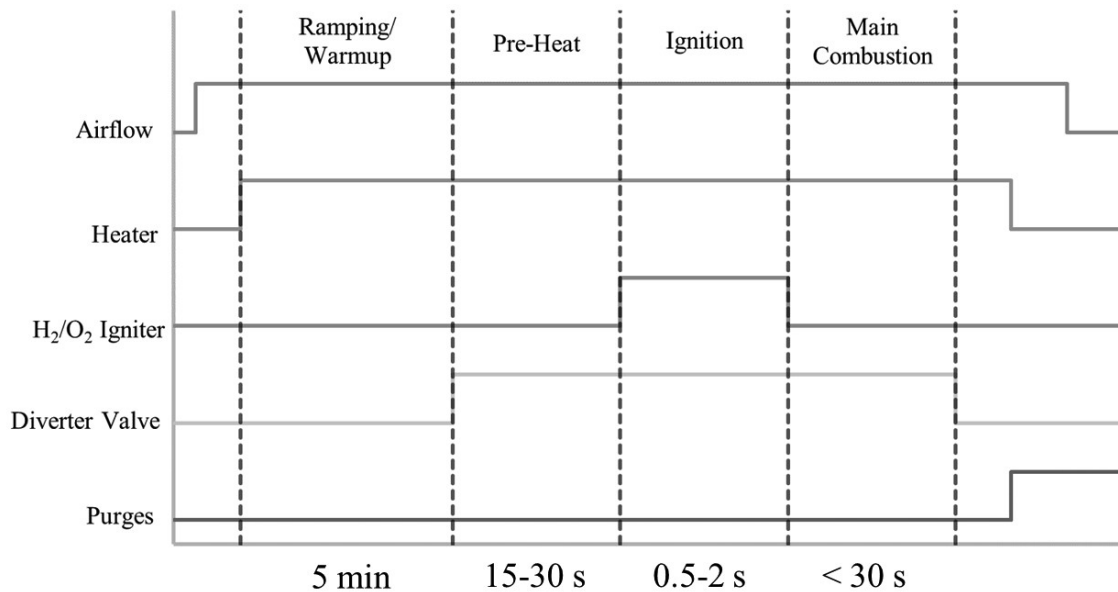
Figure 3.6: Test Sequencing

During the pre-heat phase, the heater has risen to the desired temperature and the diverter valve is set to allow heated air to be passed through the ramjet. This pre-heats the fuel grain. Heated air is left running throughout the motor for the remainder of the test.

In the ignition phase, the igniter gases are flowed and ignited. The igniter gas flow is left running for the duration of the ignition phase to ensure the grain is uniformly lit. Igniter gas flows are stopped at the end of the ignition phase.

In the main combustion phase, the combustion of the fuel grain is allowed to commence unbothered. After the flame out event is observed, a nitrogen purge is turned quench any residual flame and clear any harmful combustion gases. Following a successful test, the test crew retrieves the spend solid fuel grain for posttest analysis and prepares the motor for another test.

54

3.5 Mass Flow Measurement Techniques

Two different mass flow measurements of the ramjet air were taken. A sonic nozzle has been traditionally how mass flow was measured. A Coriolis flow meter was installed for the current set of SFRJ tests for greater accuracy. Both systems are installed in line with one another. Both should report the same mass flow by continuity unless there is a loss of mass such as a leak in a joint. This was investigated as part of this thesis.

3.5.1 Sonic Nozzles

Sonic nozzles are a common type of mass flow measurement. They only require one pressure measurement unlike the common differential pressure flow measurement systems which require two to obtain a differential pressure measurement. The total pressure immediately upstream of the sonic nozzle is taken in addition to the temperature and they are fed into Equation 3.1 for the calculation of the mass flow. Knowledge of the ratio of the specific heats is required which is widely available and accurate for air. The throat area (A_{throat}) is what sets the mass flow regime with an understanding of expected pressures.

$$\dot{m} = c_D p_t A_{throat} \sqrt{\frac{\gamma}{RT_t}} \left(\frac{2}{\gamma+1}\right)^{\frac{\gamma+1}{2(\gamma-1)}} \qquad (3.1)$$

Choked nozzles decouple the upstream and downstream flow by accelerating the flow to Mach 1. This allows a steady mass flow regardless of the downstream pressure so

long as the downstream pressure does not grow so large as to unchoke the nozzle. These issues are handled in the design phase of experiments.

A coefficient of discharge is associated with a nozzle which captures flow inefficiencies such as the vena contracta, frictional losses, and other sources. Temperature has an influence due to the thermal boundary layer in the nozzle, the thermal expansion of the nozzle material, and the gas dynamic properties of the flow [23]. Often data of the coefficient of discharge does not exist in the range required for experiments, so estimates must be made.

The sonic nozzle assembly used in this experiment is shown in Figure 3.7. It is a FlowMaxx sonic venturi. In the figure, it does not have its pressure transducer attached [44]. The throat diameter used for the tests in the work is 0.255 in.

Figure 3.7: FlowMaxx Sonic Nozzle Assembly

3.5.2 Coriolis Flow Meters

Coriolis flow meters work on an entirely separate principle from sonic nozzles. They use the Coriolis effect of fluid traveling through a tube to determine mass flow and fluid density. A diagram of the tube with sensors is shown in Figure 3.8. The fluid of interest is passed through a tube which is energized by a known vibration. The momentum

of the fluid passing through the tube causes a change in the vibration and results in a phase shift which is proportional to the mass flow through the meter. There is also a change in the natural frequency which is proportional to the density of the fluid in the flow meter. With mass flow and density known, volumetric flow rate can be easily calculated. Temperature of the fluid, which affects the components of the flow meter, is measured and taken into account for the measurements by the flow meter [45].
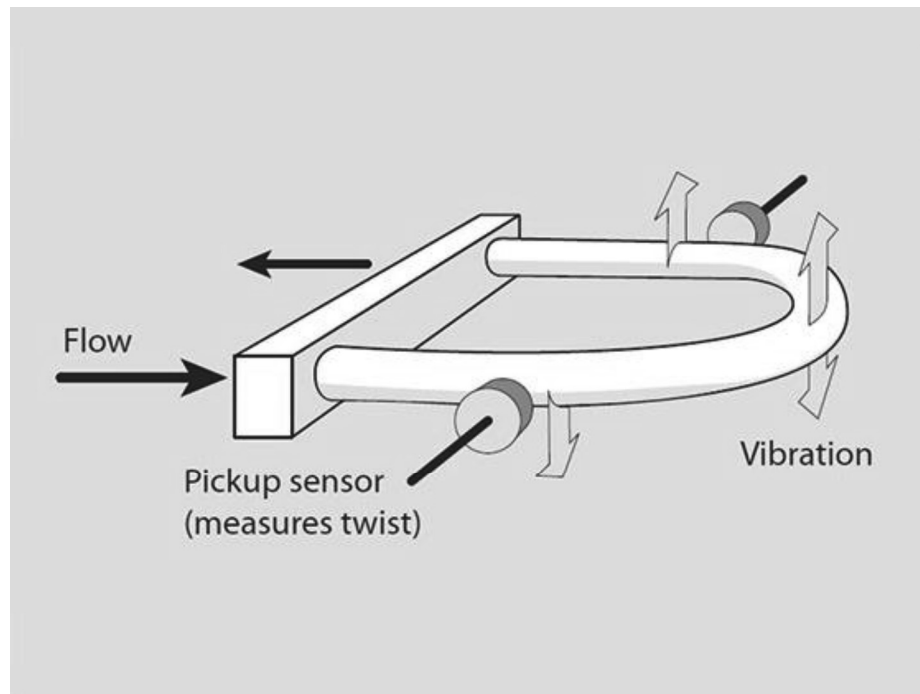
Figure 3.8: Coriolis Flow Meter Notional Operation

Coriolis flow meters work for all fluids which includes liquids, gases, and even supercritical fluids. They directly measure mass flow unlike sonic nozzles and differential pressure flow meters allowing highly accurate measurements. They require no knowledge of the fluid of interest in order to make accurate measurements unlike pressure-based mass flow measurements which typically require knowledge of the specific heats and densities

measured by other devices. This property also makes them ideal for measuring the mass

flow of mixtures whose composition is unknown [45]. Figure 3.9 shows the Micro Motion

Elite Coriolis Flow Meter CMFS025P used during the tests. They are generally larger than

sonic nozzle flow measurement devices though not necessarily massive.
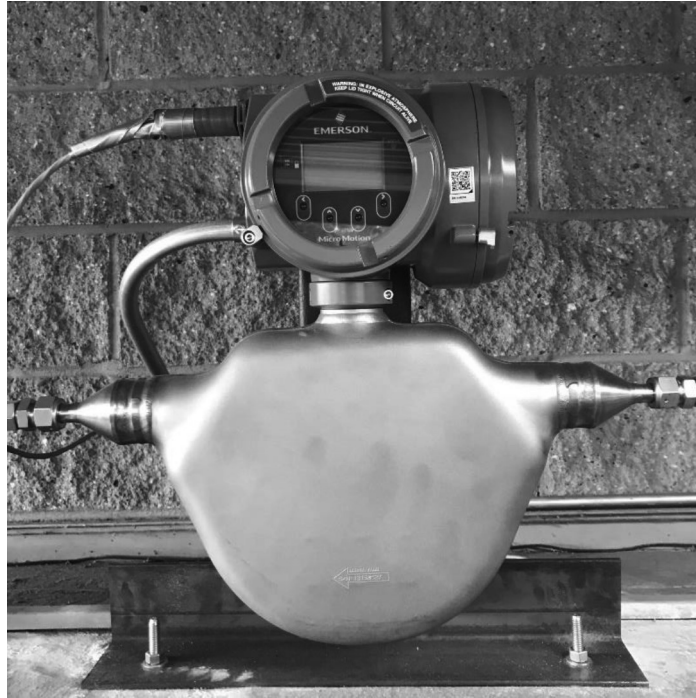
Figure 3.9: Micro Motion Elite Coriolis Flow Meter CMFS025P

CHAPTER 4

DATA REDUCTION METHOD

The data collected before, during, and after a test firing does not directly contain the desired performance parameters and their uncertainties. A data reduction scheme following guidance from established literature was developed to first produce the key performance parameters of thrust (F), specific impulse (I_{sp}), vacuum specific impulse ($I_{sp,vac}$), specific impulse efficiency ($\eta_{i_{sp}}$) characteristic velocity (c^*), characteristic velocity efficiency (η_{c^*}), as well as burn rate (r), and a burning rate equation. Following establishment of the performance parameter data reduction equations, a Monte Carlo routine was implemented to establish confidence intervals on the results as well as other intermediate calculated parameters. Data from a representative test are shown to illustrate measurements and methods used to determine results. Details for all the tests are shown in the cited appendices.

4.1 Collected Data

The data collected for a test is grouped into three categories. They are the pretest, test, and posttest data sets. The pretest data set includes information about the configuration of the test cell, configuration of the test article, and thermochemical properties. The test data set is the collection pressures, temperatures, and mass flow parameters recorded during an experiment. The post test data set is the final mass of the grain after being fired.

4.1.1 Pretest and Posttest Calculations, Measurements, and Data

Table 4.1 and Table 4.2 show the variables that were part of the pretest and posttest data collection. The pretest dataset consists of the weights and geometry of the grains, theoretical propellant properties from a thermochemical solver, and test hardware dimensions. The posttest consists of the weight of the spent fuel grain assembly. The measurement sources are listed.

Before the test, the weight of the empty liners and weight of loaded grain assemblies were measured. The inner and outer diameters of the propellant were measured as well as the length of the propellant in the liner.

Dimensions of the test hardware is taken such as the diameter of the test article nozzle, the diameter of the sonic nozzle, and the sonic orifice diameters for the hydrogen and oxygen lines for the igniter, and inlet diameter for the test article. The discharge coefficient estimates for the nozzles and orifices are included using a American Society of Mechanical Engineers guide [46]. Ambient pressure was recorded using data from a local weather station data [47].

Theoretical values for the c^* and ratio of the specific heats are calculated at the measured oxidizer to fuel ratio (O/F) for the test. A thermochemical code was used to produce curves of c^* and γ as a function of O/F. A table of the thermochemical inputs and outputs may be seen in Appendix B. These curves were polled at the measured O/F to get the theoretical values. These codes and the assumptions therein introduce a source of error.

Table 4.1: Pretest Variables

Variable	Units	Description	Source
$c_{D,H2}$	-	Hydrogen Orifice Coefficient of Discharge	Literature
$c_{D,noz}$	-	Sonic Nozzle Coefficient of Discharge	Literature
$c_{D,O2}$	-	Oxygen Orifice Coefficient of Discharge	Literature
c_{D5}	-	Nozzle Coefficient of Discharge	Literature
d_{H2}	in	Hydrogen Orifice Diameter	Datasheet
d_i	in	Grain Inner Diameter	Calipers
$d_{H2,tube}$	in	Hydrogen Tube Diameter	Calipers
d_{noz}	in	Sonic Nozzle Diameter	Datasheet
d_o	in	Grain Outer Diameter	Calipers
d_{O2}	in	Oxygen Orifice Diameter	Datasheet
$d_{O2,tube}$	in	Oxygen Tube Diameter	Calipers
d_5	in	Nozzle Throat Diameter	Calipers
d_6	in	Nozzle Exit Diameter	Datasheet
L	in	Grain Length	Calipers
m_{assy}	lbm	Fuel Grain Assembly Mass	Scale
m_{liner}	lbm	Fuel Grain Liner Mass	Scale
p_∞	psia	Ambient Pressure	Weather Station
R_a	$\dfrac{\text{ft lb}}{\text{slug °R}}$	Specific Gas Constant of Air	Literature
R_{H2}	$\dfrac{\text{ft lb}}{\text{slug °R}}$	Specific Gas Constant for Hydrogen	Literature
R_{O2}	$\dfrac{\text{ft lb}}{\text{slug °R}}$	Specific Gas Constant for Oxygen	Literature
t_{burn}	s	Burn Phase Time	Test Sequence
t_{ign}	s	Igniter Phase Time	Test Sequence
$t_{preheat}$	s	Preheat Phase Time	Test Sequence
T_{H2}	°F	Hydrogen Temperature	Estimate
T_{O2}	°F	Oxygen Temperature	Estimate
γ	-	Ratio of the Specific Heats for the Combustion Gasses	Thermochemical Code
θ	°	Nozzle Half Angle	Datasheet

Table 4.2: Posttest Variable

Variable	Units	Description	Source
m_{post}	lbm	Fuel Grain Assembly Post Test Mass	Scale

The program has the specific heats as function of temperature for the propellants and combustion products. The ratio of the specific heats and specific gas constants for air, oxygen, and hydrogen are calculated based on these data [48]. The igniter hydrogen and oxygen lines do not have a temperature probe installed, and the ratio of their specific heats is a function of temperature, so a temperature was assumed. The propellant temperature values for the ignitor and their uncertainties were estimated based on the experience of the resident test engineer [41]. The phase time durations come from the times allotted in the test sequencing.

The posttest data consists of the weight of the spent fuel grain. The mass of the fuel is a critical measurement and care was taken to ensure that an accurate measurement was obtained. The grain was greased for easy insertion into the test article and required a thorough cleaning afterwards. Any grease left on the spent fuel grain would bias the burned propellant mass calculation lower which would cause a perceived increase in characteristic velocity and specific impulse.

4.1.2 Test Data

The data collected during the tests comes the pressure transducers, thermocouples, and Coriolis flow meter. Table 4.3 shows the variables that were measured and that appear in the data reduction process. The sensor models for each may be found in Appendix A. They were all collected as time series data but were condensed into averages. This is discussed in Section 4.2.

Table 4.3: Measured Variables from Test Firing that Appear in Data Reduction

Variable	Units	Name	Sensor
p_4	psia	Combustor Static Pressure	Aft End Pressure Transducer
T_a	°F	Air Temperature	Port Thermocouple
p_{noz}	psia	Sonic Nozzle Pressure	Sonic Nozzle Transducer
T_{noz}	°F	Sonic Nozzle Temperature	Sonic Nozzle Thermocouple
$\dot{m}_a$	lbm/s	Air Mass Flow	Coriolis Flow Meter
p_{O2}	psia	Oxygen Orifice Pressure	Ox Orifice Transducer
p_{H2}	psia	Hydrogen Orifice Pressure	H2 Orifice Transducer

The transducers are sampled at 90 times a second to record a trace. An example pressure trace, temperature trace, and mass flow trace from A_{LH1} are shown in Figure 4.1, Figure 4.2, and Figure 4.3 respectively. All 16 of the tests' respective traces have similar overall characteristics. All the test data is shown in Appendix C.
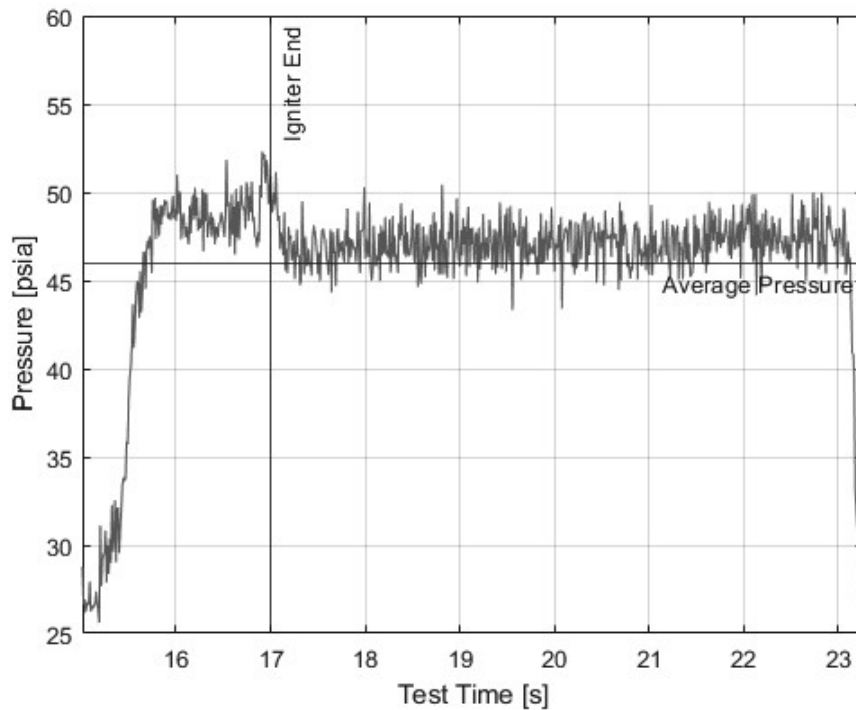
Figure 4.1: A_{HL1} Pressure Trace
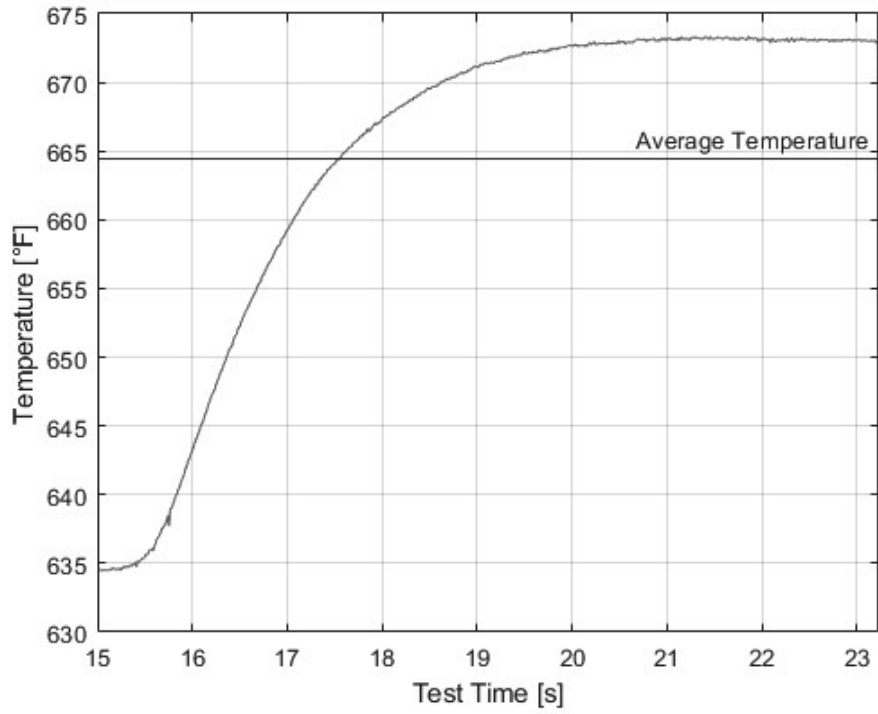
Figure 4.2: A_{HL1} Air Temperature ($T_a = Average$) Trace
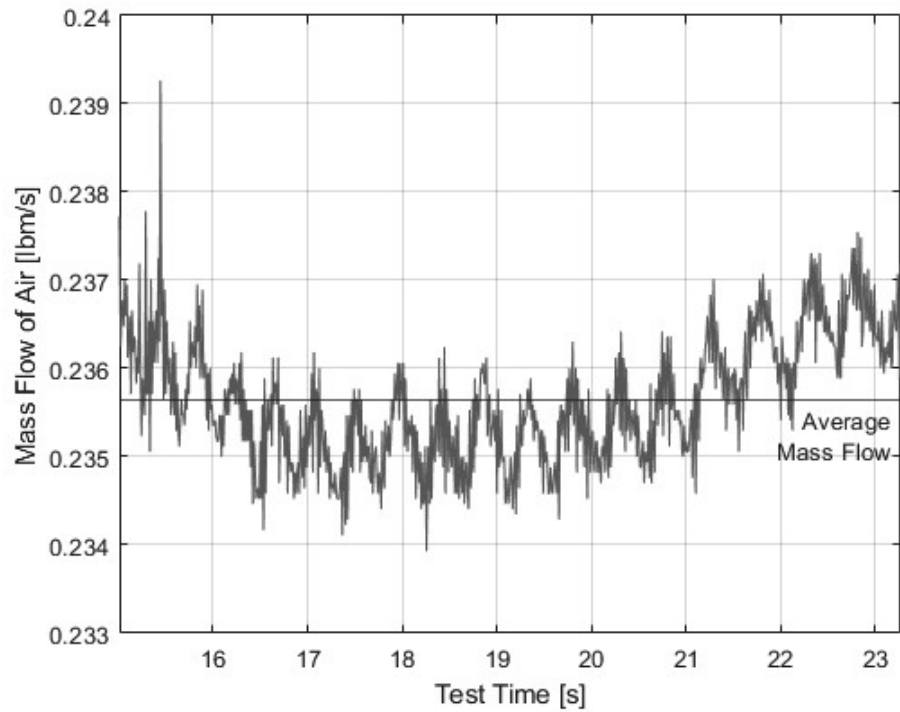
Figure 4.3: A_{HL1} Air Mass Flow Trace

Figure 4.1 shows the initial ignition transient, and initial elevation in pressure during the igniter burn, and then a level portion until flame out. The igniter was turned on at 15 seconds. The vertical black line shows where the igniter was turned off. The horizontal line shows the average pressure. The chamber pressure has a higher level during the igniter, which drops at the time of igniter shutoff. This effect is accounted for by including its mass flow and combustion contributions in the theoretical calculations and the data reduction equations.

Figure 4.2 shows that the temperature trace exhibits a first-order response. The rise in temperature above the set point is due to either the combustion which heats up the incoming air in addition to any heat soaking through piping or to the combustion products in the chamber slowing down the flow of air, increasing the heat the thermocouple can absorb. The horizontal line shows the average temperature.

The Coriolis mass flow traces all show periodic instability. They frequency is not the same test to test. It should not be a result of combustion instability since the ramjet is decoupled by the sonic nozzle. The horizontal line shows the average mass flow.

4.2 Data Reduction Process

The first step in the data reduction process is to find the burn time for a test. The burn time is merely the difference of the burn start time and burn end time as shown Equation 4.1.

$$t_b = t_{b,f} - t_{b,s} \qquad (4.1)$$

The method chosen was to take the start of the burn as the time when the aft end pressure transducer reaches 10% of the maximum the end time as the point when it passes back through this value. The pressure traces and burn start and times can be seen in Appendix C. An example of the data with the burn start and end time is shown in Figure 4.4. All subsequent figures and tables presented use truncated data in a time window between the start and stop time unless explicitly stated otherwise. Burn times were compared between replications and adjusted if any irregularities were discovered. This is discussed in greater detail in Appendix C.
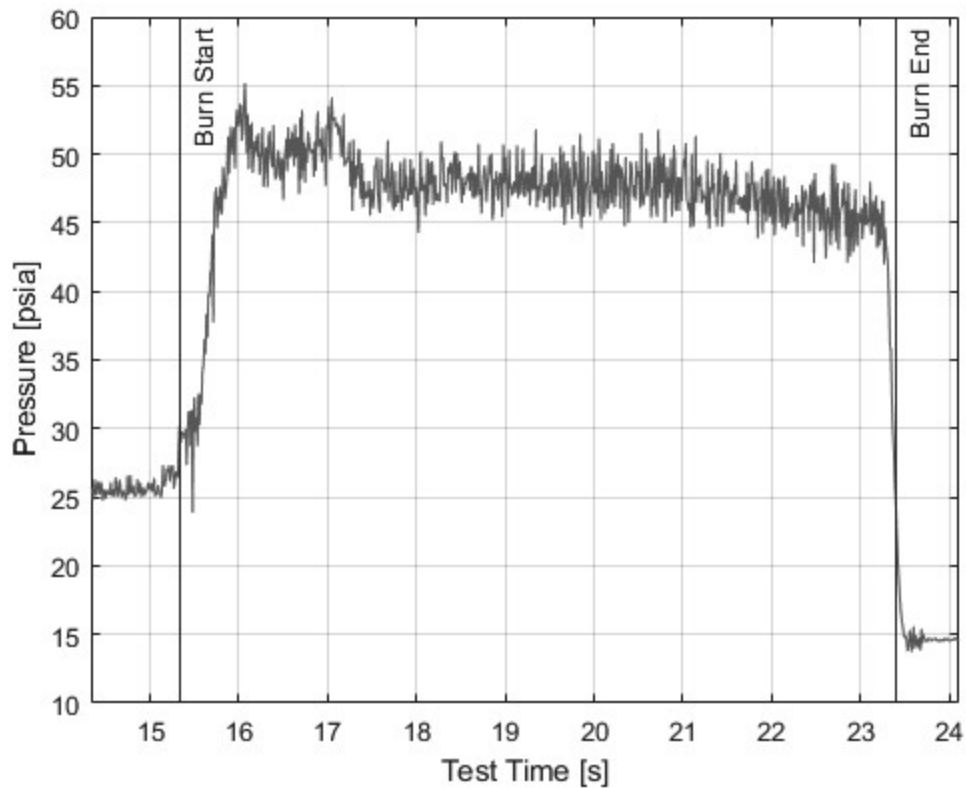
Figure 4.4: Burn Time Example

The truncated time results collected during the test such as the combustor pressures and mass flow were reduced into a single point by computing their averages. This was done with the average value theorem shown in Equation 4. The trapezoidal method used for the integration.

$$\bar{X} = \frac{1}{t_b} \int_0^{t_b} X(t) \, dt \qquad (4.1)$$

Table 4.3 shows the variables that were measured during the test firing that were reduced into their averages that also appear in the following data reduction process. The averaged variables do not use the bar notation which normally signifies that they are an average. Instead all of the data reduction equations moving forward assume an average is used and produce an average value.

The averaging process also has an advantage of smoothing out any known or unknown disturbances or irregularities in any of the time series data. Using averages eliminates the need to construct time series data estimates of web burned, flow area, and mass flow of the fuel. Their assumed profiles would introduce conceptual bias into the data reduction equations.

The mass of the propellant and mass burned are shown by Equation 4.2 and Equation 4.3, respectively. The mass of the propellant (m_p) is the difference of the loaded grain assembly (m_{assy}), a phenolic liner with propellant cast inside, and the mass of the phenolic liner (m_{liner}). The mass burned during the test (m_b) is the difference of the loaded grain assembly and the posttest grain assembly mass (m_{post}). Using the calculated masses, the web thickness burned may be calculated using Equation 2.29.

67

$$m_p = m_{assy} - m_{liner} \tag{4.2}$$

$$m_b = m_{assy} - m_{post} \tag{4.3}$$

The propellant density was calculated using Equation 4.5.

$$\rho_p = \frac{4m_p}{\pi(d_o^2 - d_i^2)L} \tag{4.5}$$

The measured pressures for the test article, sonic nozzle, and igniter sonic orifices were converted to their stagnation pressures. This is done using Equations 2.4 and 2.5.

$$M_4 = \frac{c_{D5}A_5}{A_4}\left(\frac{2}{\gamma + 1} + \frac{\gamma - 1}{\gamma + 1}M_4^2\right)^{\frac{\gamma - 1}{2(\gamma + 1)}} \tag{2.4}$$

$$p_{t4} = p_4\left(1 + \frac{\gamma - 1}{2}M_4^2\right)^{\frac{\gamma}{\gamma - 1}} \tag{2.5}$$

Equation 2.4 has two solutions, and the subsonic solution is taken because the flow is upstream of the nozzle throat.

The determination of the air mass flow is done through two different means. The Coriolis flow meter is the preferred method, but the sonic nozzle mass flow calculated for comparison. The Coriolis flow meter directly reports mass flow the DAQ. The sonic nozzle utilizes Equation 3.1. The hydrogen and oxygen orifices are also governed by Equation 3.1.

$$\dot{m} = c_D p_t A_t \sqrt{\frac{\gamma}{RT_t}} \left(\frac{2}{\gamma + 1}\right)^{\frac{\gamma+1}{2(\gamma-1)}} \tag{3.1}$$

The air flux was calculated using Equation 4.8. The mass flow of the air was normalized against the average port area of the fuel grain for the burn. The denominator shows how the average port area was calculated.

$$G_a = \frac{\dot{m}_a}{\frac{\pi}{4}(d_i + 2w_b)^2} \tag{4.8}$$

The fuel mass flow rate is determined simply as the mass of burned fuel divided by the time of the burn as shown in Equation 4.9. There are no direct measurements in the test article to determine exactly how it behaves as a function of time.

$$\dot{m}_f = \frac{m_b}{t_b} \tag{4.9}$$

The total mass flow is a sum of all of the component mass flows. This can be seen in Equation 4.10. The fuel and air mass flows are present throughout the duration of the burn. The hydrogen and oxygen mass flows are only active during the time the igniter is on (t_{ign}). The igniter contribution is averaged out over the duration of the burn so that the components may be added to the others.

$$\dot{m}_4 = \dot{m}_f + \dot{m}_a + \frac{t_{ign}}{t_b}(\dot{m}_{H2} + \dot{m}_{O2}) \qquad (4.10)$$

The average burn rate, not to be confused with the burn rate equation that governs it, is calculated by Equation 4.11. It is implicitly an average burn rate similar to how the mass flow of the fuel is calculated. Using the burn rates for each test, a burn rate equation was fit.

$$\dot{r} = \frac{w_b}{t_b} \qquad (4.11)$$

The oxidizer to fuel ratio is calculated as shown in Equation 4.12. It is taken as the ratio of the mass flow of air to the mass flow of fuel.

$$\frac{O}{F} = \frac{\dot{m}_a}{\dot{m}_f} \qquad (4.12)$$

Thrust was calculated using Equation 2.2. The coefficient of thrust was calculated with Equation 2.3.

$$F_6 = C_F p_{t4} A_5 \qquad (2.2)$$

$$C_F = \frac{1 + \cos\theta}{2} \sqrt{\frac{2\gamma^2}{\gamma - 1}\left(\frac{2}{\gamma + 1}\right)^{\frac{\gamma+1}{\gamma-1}}\left[1 - \left(\frac{p_6}{p_{t4}}\right)^{\frac{\gamma-1}{\gamma}}\right]} + \frac{(p_6 - p_\infty)A_6}{p_{t4} A_5} \qquad (2.3)$$

The impulse, specific impulse, and vacuum specific impulse are calculated with Equations 2.6, 2.7, and 2.8 respectively.

$$I_t = F_6 t_b \qquad (2.6)$$

$$I_{sp} = \frac{I_t}{m_b g_0} \qquad (2.7)$$

$$I_{isp,vac} = \frac{I_t + p_\infty A_6 t_b}{m_p g_0} \qquad (2.8)$$

The equations for characteristic velocity and the characteristic velocity efficiency are presented in Equations 2.9 and 2.13. The theoretical characteristic velocity is part of the pretest data set that comes from a thermochemical equilibrium code.

4.3 Uncertainty Analysis

The MCM was the chosen uncertainty analysis method for this work. This section details the elemental errors used for the performance parameters. This includes how the pressure transducer errors were obtained. It also explains the setup of the performance parameter and burn rate equation Monte Carlo routines.

4.3.1 Uncertainty Sources

The elemental systematic errors for the pretest and posttest data are shown in Table 4.4. The mass measurement errors were taken to be the half of the least significant digit of the scale.

The diameter and length errors of the propellant were taken to be the accuracy of the of measurement tool. For the diameters, a random component was included, shown in Table 4.5, to include the difficulty in measuring a round object with calipers with irregularities in the circular profile.

For the preheat, ignition, and burn sequence times, an asymmetric error was included. The valves that control the flow of air and igniter gases have lag times. They will actuate before their time in the sequence, only later. Therefore, a triangular distribution with its mean and mode after the nominal value were applied.

For the nozzle diameters and angle, the manufacturing tolerances were applied. For the nozzle throat, there were slag deposits observed. These were not able to be removed completely between tests. They were also not measured. A best estimate is included to account for their presence. An asymmetric distribution that skews the throat diameter small was used. The coefficient of discharge for the nozzle is an estimate from AGARD [18].

The sonic nozzle diameter has its manufacturing tolerance applied. The coefficient of discharge is an estimate from an American Society of Mechanical Engineers Guide [46].

The error in the ambient pressure is taken to be the least significant digit in the available weather data.

The error in the ratio of specific heats for the combustion products is an estimate at a reasonable order of magnitude.

The errors in the diameters of the igniter sonic orifices are from the manufacturing tolerances. Their coefficients of discharge errors that were taken are estimates in their pressure ratio range. The error in temperature of the igniter lines is an estimate based on test engineer experience [41].

72

Table 4.4: Systematic Uncertainties for Pretest and Post Test Data

Variable	Distribution	μ	2σ		Units	Description
		a	b	c		
$c_{D,H2}$	Normal	0	0.03		-	Combined Estimate
$c_{D,noz}$	Normal	0	0.025		-	Combined Estimate
$c_{D,O2}$	Normal	0	0.03		-	Combined Estimate
c_{D5}	Normal	0	0.01		-	Combined Estimate
d_{H2}	Normal	0	0.0001		in	Manufacturing Tolerance
d_i	Normal	0	0.001		in	Measurement Accuracy
$d_{H2,tube}$	Normal	0	0.010		in	Manufacturing Tolerance
d_{noz}	Normal	0	0.001		in	Manufacturing Tolerance
d_o	Normal	0	0.001		in	Measurement Accuracy
d_{O2}	Normal	0	0.0001		in	Manufacturing Tolerance
$d_{O2,tube}$	Normal	0	0.010		in	Manufacturing Tolerance
d_5	Normal	0	0.010		in	Manufacturing Tolerance
	Triangular	-1/16	0	0	in	Throat Deposits
d_6	Normal	0	0.010		in	Manufacturing Tolerance
L	Normal	0	0.039		in	Measurement Accuracy
m_{assy}	Normal	0	0.0011		lbm	Half of Least Significant Digit
m_{liner}	Normal	0	0.0011		lbm	Half of Least Significant Digit
m_{post}	Normal	0	0.0011		lbm	Half of Least Significant Digit
p_∞	Normal	0	0.005		psi	Half of Least Significant Digit
t_{burn}	Triangular	0	0.25	0.5	s	Slow Valve Actuation
t_{ign}	Triangular	0	0.25	0.5	s	Slow Valve Actuation
$t_{preheat}$	Triangular	0	0.25	0.5	s	Slow Valve Actuation
T_{O2}	Normal	0	10		°F	Operator Estimate
T_{H2}	Normal	0	10		°F	Operator Estimate
γ	Normal	0	0.01		-	Estimate
θ	Normal	0	1		deg	Manufacturing Tolerance

Table 4.5: Random Uncertainties for Pretest and Post Test Data

Variable	Distribution	μ	2σ	Units	Description
d_i	Normal	0	0.010	in	Eccentricity in Fuel Grain
d_o	Normal	0	0.010	in	Eccentricity in Fuel Grain

For the time series test data, the random uncertainties were calculated using the direct method using Equation 2.59. The systematic uncertainties are shown in Table 4.6.

For each of the pressure transducers, there is calibration error, temperature error, and long-term stability error. The temperature errors and long-term stability errors were pulled from the transducer's datasheets. The calibration error includes the effects for nonlinearity, hysteresis, repeatability, zero offset, and span. The calibration accounts for these effects. The error of the calibration is smaller than each effect alone. The calculation of the calibration errors is detailed in Appendix D.

The errors for the thermocouples and Coriolis flow meter are the manufacturer specified tolerances. These errors are multiplicative instead of fixed values. Each test has a different distribution in temperature and mass flow based on its nominal value.

$$\varepsilon_r = \sqrt{\frac{1}{N-1}\sum_{i=1}^{N}(r_i - \bar{r})^2} \qquad (2.59)$$

Table 4.6: Systematic Uncertainties for Test Data

Variable	Distribution	μ	2σ	Units	Description
	Normal	0	1.77		Calibration
p_4	Normal	0	1.13	psi	Temperature Effects
	Normal	0	0.30		Long Term Stability
	Normal	0	4.32		Calibration
p_{noz}	Normal	0	3.75	psi	Temperature Effects
	Normal	0	2.50		Long Term Stability
	Normal	0	4.00		Calibration
p_{O2}	Normal	0	7.50	psi	Temperature Effects
	Normal	0	1.50		Long Term Stability
	Normal	0	4.00		Calibration
p_{H2}	Normal	0	7.50	psi	Temperature Effects
	Normal	0	1.50		Long Term Stability
T_{noz}	Normal	0	1.35	%	Manufacturer Specification at Average Process Temperature
T_a	Normal	0	1.35	%	Manufacturer Specification at Average Process Temperature
$\dot{m}_a$	Normal	0	0.20	%	Manufacturer Specification Accuracy at Average Mass Flow Rate
	Normal	0	0.25		Manufacturer Specification Repeatability at Average Mass Flow Rate

4.3.2 Monte Carlo Procedure for Performance Parameters

For the performance parameters the MCM process outlined in 2.5.4 was used. The measured variables were taken to be the pretest, test, posttest data sets. The errors distributions for each measured variable are show in Section 4.3.1. The result variables were the performance parameters.

4.3.3 Monte Carlo Procedure for Burn Rate Equation

The MCM uncertainty calculation for the burn rate equation is outlined in Section 2.5.5 except generalized to a multiple linear regression. The inputs are the burn rate and predictors at each test. The error distribution for each is their confidence interval from the performance parameter MCM. The output is a set of points that is the confidence interval

of the burn rate equation at each test point. A curve fit can be applied to the points to form

a confidence envelope, typically surfaces or hypersurfaces.

CHAPTER 5

RESULTS

This chapter details the results of the application of the data reduction and uncertainty analysis processes described previously. Theoretical performance in the characteristic velocity is established for comparison against test data. The uncertainty intervals are calculated for the performance/efficiency parameters and solid fuel burn rate equations.

5.1 Mass Flow Rate Method Comparison

A Coriolis flow meter was installed in line with the sonic nozzle flow meter that has historically been used in the test facility for the SFRJ experiment. With no mass flow loss in the tubes, the flow meter and sonic nozzle should measure the same mass flow. A comparison of the air mass flow rates from the Coriolis flow meter and the sonic nozzle are shown in Table 5.1 and Figure 5.1. The MCM outlined in Section 2.5.4 was used.

Table 5.1: Coriolis Flow Meter and Sonic Nozzle Mass Flow Rates

| Test	$\dot{m}_{cor}$ $[\frac{lbm}{s}]$	$\dot{m}_{cor}\%$ Uncertainty	$\dot{m}_{noz}$ $[\frac{lbm}{s}]$	$\dot{m}_{noz}\%$ Uncertainty
A_{LL1}	0.1419	0.32	0.1340	5.98
A_{LL2}	0.1419	0.32	0.1339	6.24
A_{LH1}	0.1422	0.32	0.1323	6.12
A_{LH2}	0.1425	0.31	0.1331	6.05
A_{HL1}	0.2358	0.33	0.2240	5.82
A_{HL2}	0.2354	0.31	0.2230	5.85
A_{HH1}	0.2407	0.32	0.2294	5.61
A_{HH2}	0.2401	0.33	0.2287	5.66
B_{LL1}	0.1520	0.32	0.1440	6.10
B_{LL2}	0.1416	0.31	0.1333	6.19
B_{LH1}	0.1423	0.32	0.1329	5.93
B_{LH2}	0.1423	0.31	0.1330	6.28
B_{HL1}	0.2353	0.33	0.2234	5.77
B_{HL2}	0.2359	0.33	0.2250	5.45
B_{HH1}	0.2389	0.32	0.2273	5.53
B_{HH2}	0.2387	0.32	0.2260	5.54
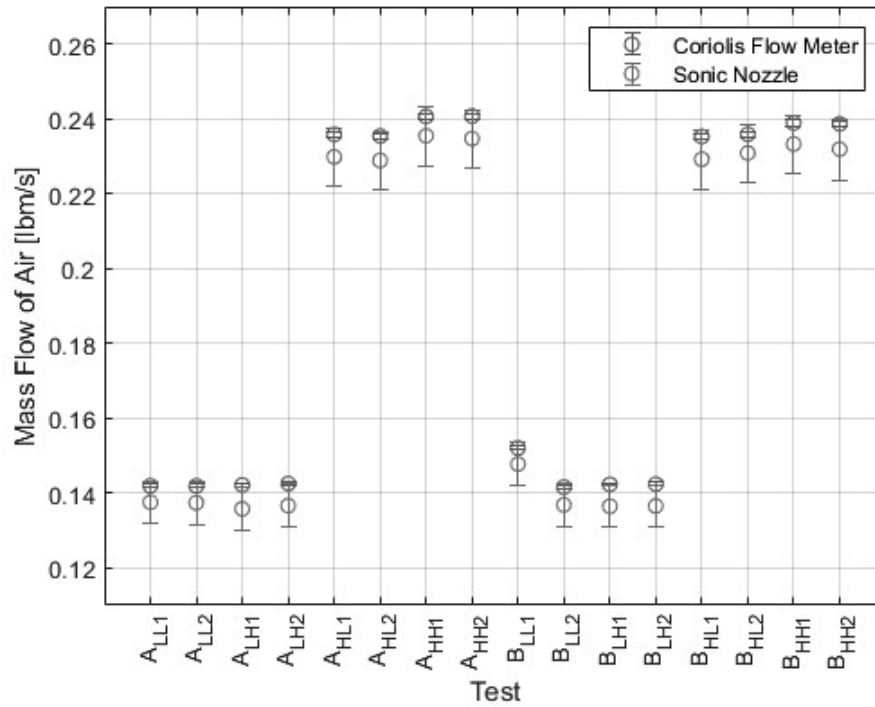
Figure 5.1: Coriolis Flow Meter vs Sonic Nozzle

Figure 5.5 shows different nominal values for each measurement at all the set points, with the sonic nozzle results being consistently lower. With the uncertainty bands in place, it can be seen their confidence intervals overlap. This indicates the systems are in possible agreement, but a bias such as incorrect discharge coefficient for the sonic nozzle or a leak could be present.

Assuming the Coriolis mass flow rate measurements are most accurate, the nominal value for the sonic nozzle measurements could be biased lower for the following reasons. First, the assumed discharge coefficient could be too low. Second, biases in the pressure transducer from heating, which cannot be captured with the current calibration scheme. The large confidence intervals in the sonic nozzle account for the potential variation in these parameters. The nominal value and confidence intervals could be improved with better knowledge of the discharge coefficient at the test conditions. The current discharge coefficient is taken to be an estimate from literature [46]. Currently the Propulsion Research Center does not have methods to do this in house.

For the time series test data, the random uncertainties were calculated using the direct method using Equation 2.59. The systematic uncertainties are shown in Table 4.6.

$$\varepsilon_r = \sqrt{\frac{1}{N-1}\sum_{i=1}^{N}(r_i - \bar{r})^2} \qquad (2.59)$$

For the Coriolis flow meter there is a manufacturer specified accuracy error. and manufacturer specified precision error. They are very small compared the errors in the pressure transducers for the sonic nozzle.

For each of the pressure transducers, there is calibration error, temperature error, and long-term stability error. They are the major driver of uncertainty in the sonic nozzle. The temperature errors and long-term stability errors were pulled from the transducer's datasheets. The calibration error includes the effects for nonlinearity, hysteresis, repeatability, zero offset, and span. The calibration accounts for these effects. The error of the calibration is smaller than each effect alone. The calculation of the calibration errors is detailed in Appendix D.

The errors for the thermocouples and Coriolis flow meter are the manufacturer specified tolerances. These errors are multiplicative instead of fixed values. Each test has a different distribution in temperature and mass flow based on its nominal value.

The uncertainties are so small that they are hard to discern on plots. It will be shown later that, the other measurement uncertainties dominate the data reduction equations. The uncertainty analysis and comparison of the results of the Coriolis flow meter and sonic nozzle determined that the mass flow from the Coriolis flow meter was used for applicable calculations.

5.2 Experiment Set Points

The two formulations were tested using a two-by-two test matrix shown in Figure 3.1. The air mass flow and air temperature were varied to obtain four distinct test points. The values for the test points are shown in Table 5.2 and depicted graphically in Figure 5.2. The temperature and mass flows were taken to be their averages over the burn time. It may be seen that the test placed near their desired set points. The exact location is not

overly critical so long as temperature and mass flow are explored. Knowing the actual values of temperature and mass flow allows for the calculation of the desired results.

Formulation A's test pairs have lower variance than Formulation B's. Temperature was the hardest to control with the high temperature tests being slightly too cold and the low temperature tests being slightly too warm. Mass flow was much easier to set consistently as shown by the tight spreads in Figure 5.2.

The uncertainty in the mass flow rates and temperatures are small. The uncertainty in the flow rate and temperature is dominated by the systematic uncertainties which make contribute 0.31% and 0.75% respectively. The random uncertainty in temperature is more prominent than for mass flow. The random uncertainty in temperature is more prominent than for mass flow. The random uncertainties in mass flow and temperature are effectively negligible.

Table 5.2: Set Point Uncertainty

| Test	$\dot{m}_a\ [\frac{\text{lbm}}{\text{s}}]$	$\dot{m}_a\%$ Uncertainty	$T_a\ [°F]$	$T_a\ \%$ Uncertainty
A_{LL1}	0.1419	0.31	665.3	0.78
A_{LL2}	0.1419	0.32	664.0	0.78
A_{LH1}	0.1422	0.32	791.7	0.80
A_{LH2}	0.1425	0.31	791.0	0.87
A_{HL1}	0.2358	0.32	664.4	0.78
A_{HL2}	0.2354	0.33	661.3	0.81
A_{HH1}	0.2407	0.32	766.5	0.82
A_{HH2}	0.2407	0.31	770.2	0.86
B_{LL1}	0.1520	0.32	665.3	0.80
B_{LL2}	0.1416	0.31	674.3	0.82
B_{LH1}	0.1423	0.33	794.9	0.85
B_{LH2}	0.1423	0.32	805.5	0.87
B_{HL1}	0.2353	0.32	664.4	0.77
B_{HL2}	0.2359	0.32	668.7	0.79
B_{HH1}	0.2389	0.33	779.7	0.86
B_{HH2}	0.2387	0.31	794.7	0.84
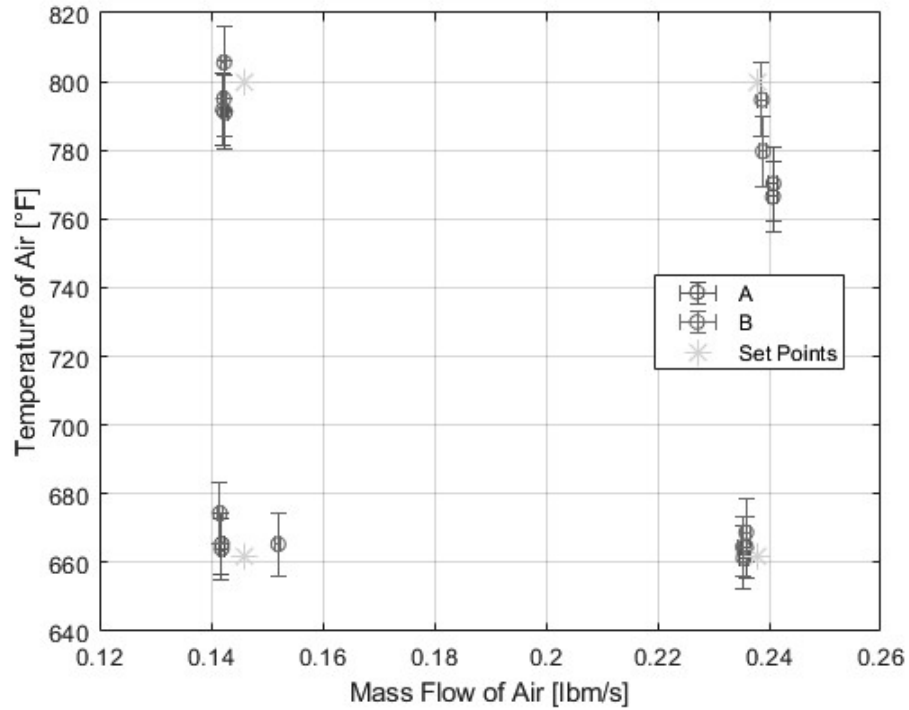
Figure 5.2: Set Point Uncertainty

5.3 Performance Parameters

Following the data reduction scheme previously outlined, the performance parameters and their combined expanded uncertainties were determined. An overview of the effects of the nozzle slag correction are presented. The conceptual bias in burn time determination is also discussed with possible effects on the results detailed.

5.3.1 Nozzle Slag Correction Effects

During testing, it was observed that there was slag deposited of the nozzle, but the change in the throat area was not measured between tests. An estimate was used assuming a worst-case throat diameter shrinkage of 1/16 in. The best case would be that there were no slag deposits which would require the deposits observed to be blown off during a test. This assumed uncertainty, as well as the manufacturing tolerance of the nozzle, produces an area distribution shown in Figure 5.3. The nominal value for the nozzle is captured within the distribution and is located at the 93.8 percentile. The assumed area distribution is used to help explain some irregularly high values obtained during the tests.
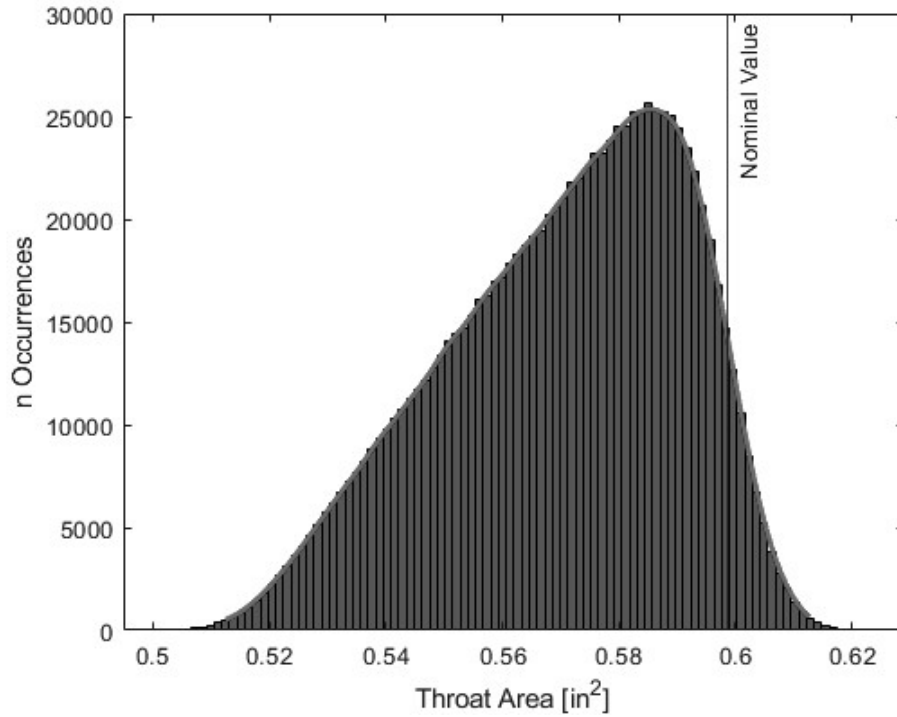
Figure 5.3: Ramjet Throat Combined Area Distribution

It was found that the nozzle correction, while needed to bring c^* values into alignment with theory, is a dominant contributor to uncertainty in all of the performance parameters. The effects of on the uncertainty on an example case are show in Figure 5.4. The nozzle correction was scaled from 100% to 0% to demonstrate its influence on the example case. Scaling down the correction reduced the overall uncertainty.
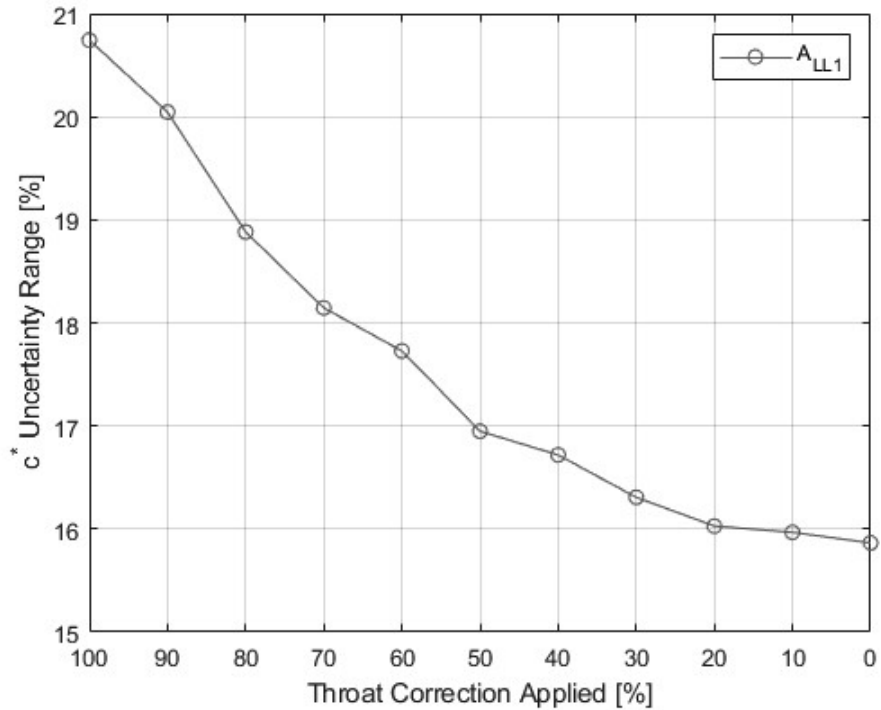
Figure 5.4: Throat Correction Effect

5.3.2 Characteristic Velocity

The characteristic velocities for each formulation were calculated with Equation 4.19 and the O/F ratios were calculated with Equation 4.12. The theoretical characteristic velocities were obtained from a curve fit CEQUEL predictions polled at the measured oxidizer to fuel ratio. The characteristic velocity efficiency was calculated using the measured value divided by the predicted value. The values for the tests are shown in Table 5.3. The characteristic velocities and oxidizer to fuel ratios may be seen for Formulation A in Figure 5.5 and Formulation B in Figure 5.6. The relative uncertainties were found to have a slight inverse proportionality to mass flow and temperature.

Table 5.3: Characteristic Velocity Results

Test	c_{th}^* $\left[\frac{ft}{s}\right]$	c^* $\left[\frac{ft}{s}\right]$	c^* Lower Uncertainty [%]	c^* Upper Uncertainty [%]	O/F	O/F Uncertainty [%]	η_{c^*}
A_{LL1}	3842	4131	-14.33	4.48	18.04	5.36	1.102
A_{LL2}	3921	4217	-14.36	3.97	16.83	5.05	1.118
A_{LH1}	4168	4386	-13.83	3.34	14.24	3.62	1.111
A_{LH2}	4165	4373	-14.50	3.26	14.24	3.64	1.095
A_{HL1}	3747	3977	-16.02	5.03	19.61	3.17	1.009
A_{HL2}	3773	4104	-14.22	4.81	19.18	2.77	1.067
A_{HH1}	3947	4226	-16.13	4.94	17.16	2.84	0.997
A_{HH2}	3994	4508	-15.32	3.98	16.47	2.40	1.065
B_{LL1}	3942	3906	-14.46	4.44	14.69	3.79	1.016
B_{LL2}	3846	4149	-14.12	4.10	15.84	4.20	1.056
B_{LH1}	4240	4352	-13.69	3.34	11.62	3.65	1.057
B_{LH2}	4231	4538	-13.83	3.61	11.68	2.68	1.097
B_{HL1}	3844	4131	-14.33	4.48	16.02	2.65	1.102
B_{HL2}	3927	4217	-14.36	3.97	14.89	2.43	1.118
B_{HH1}	4116	4386	-13.83	3.34	13.05	2.10	1.111
B_{HH2}	4138	4373	-14.50	3.26	12.78	2.12	1.095

The uncertainties in characteristic velocity are asymmetric about the nominal value due to the throat diameter correction distribution was assumed. Without a correction, the uncertainty bands would have not always captured the theoretical characteristic velocity. The predictions from CEQUEL, or any thermochemical code, are not perfect, but they are not generally highly divergent from reality.

Formulation A's test pairs were closer to one another than Formulation B's. For all pairs in Formulation A, the uncertainty bands overlapped. In Formulation B, only the LH and HH pairs overlapped themselves. This is a result of the inaccuracies in the set points for the tests. Formulation B's test pairs had a wider spread than Formulation A.
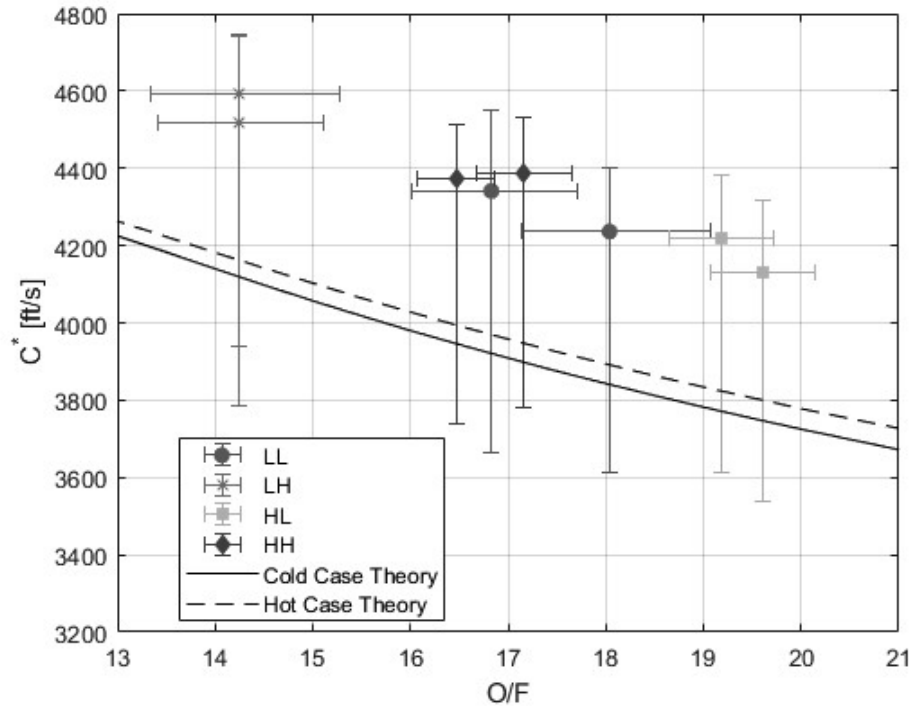
Figure 5.5: Formulation A c^* vs O/F

In Figure 5.5 it may be seen that the LL and HH sets overlap considerably. The uncertainty of the LL set almost completely envelopes the HH sets. This indicates an inability to measure a test-to-test difference between the two cases. A similar phenomenon occurs in Figure 5.6 where the LL set and HL set intermingles. The same conclusion can be drawn for those two sets in Formulation B that it is practically impossible to measure test-to-test differences between the sets. In both formulations, the LL set has the largest uncertainty bands in O/F. This is a result of a proportionally larger burned fuel mass uncertainty for the low air mass flow and temperature case. The lowest O/F uncertainties are found in the HH cases, where the most fuel mass is burned, making the constant systematic uncertainty proportionally smaller.
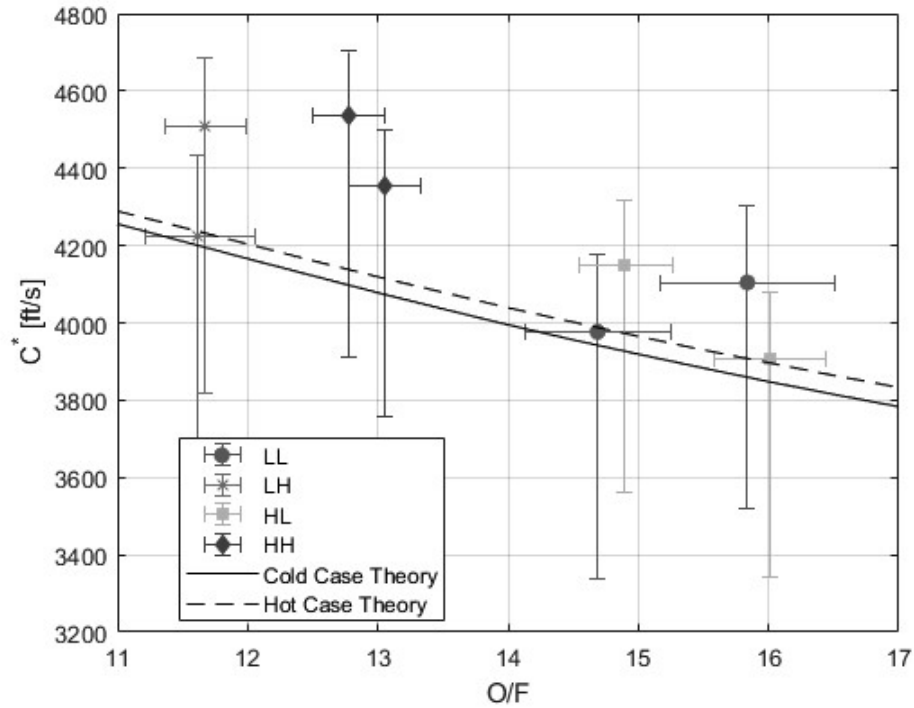
Figure 5.6: Formulation B c^* vs O/F

The efficiencies and their uncertainties may be seen in Figure 5.8. The characteristic velocity efficiencies act as a proxy for the combustion efficiency which is the ideal figure of merit. All of the efficiencies for Formulation A and seven of the efficiencies for Formulation B were greater than 1. This is highly atypical for nominal values. It is thought to be mostly a result of nozzle clogging. A clogged nozzle would drive up chamber pressure, which would drive up characteristic velocity. An asymmetric correction for the presumably clogged nozzle was applied which pushed the confidence interval lower. All of the tests have their theoretical values within the confidence intervals with the application of the nozzle correction.
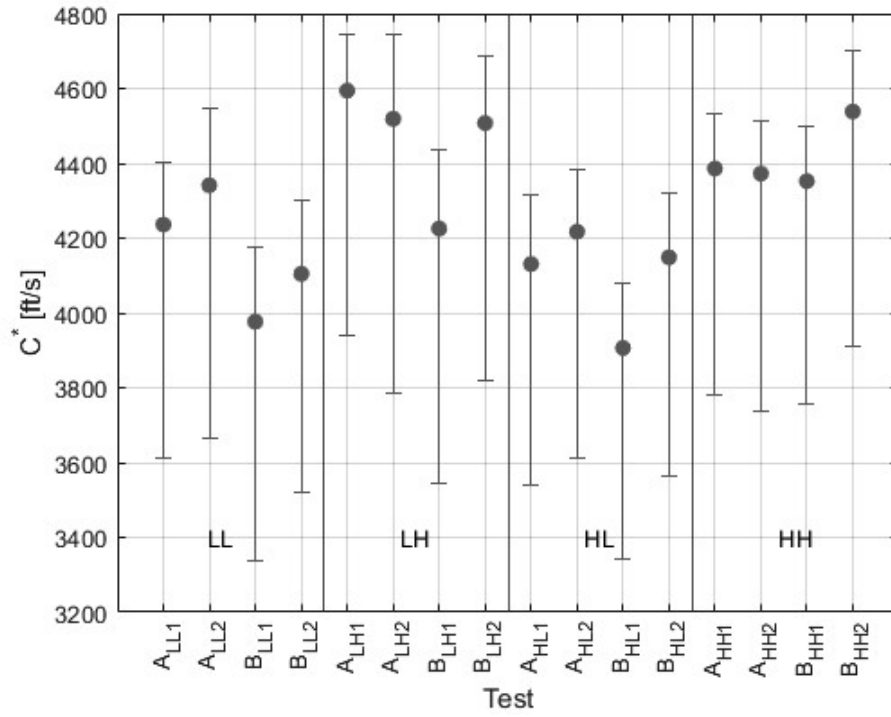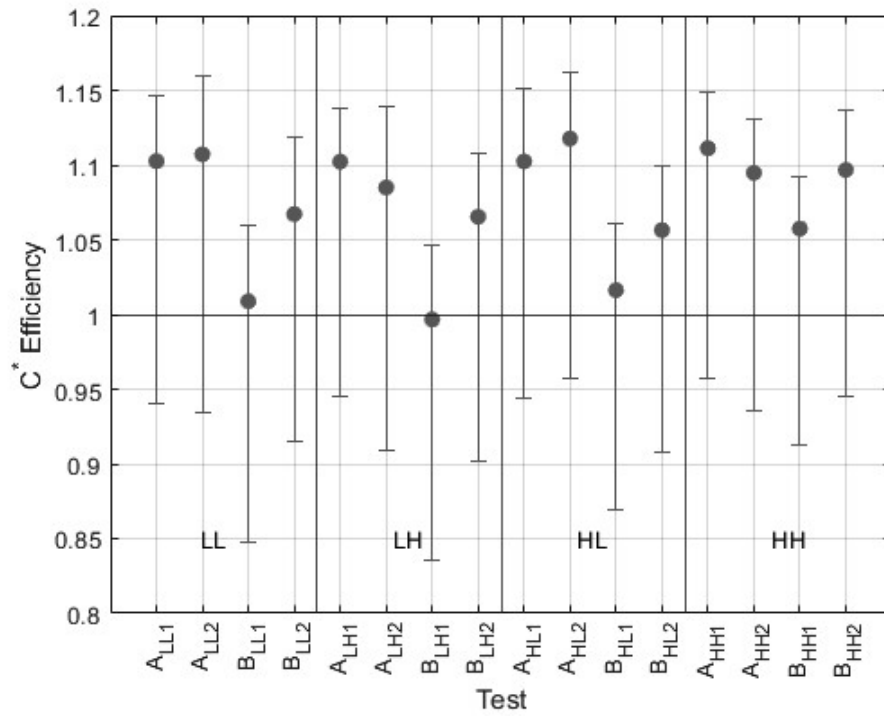
Figure 5.7: c^*

Figure 5.8: c^* Efficiencies

Some other sources of uncertainty that could be influencing the efficiencies to be are the thermochemistry, the formulation ingredient mixing ratios, and phenolic liner burned from the mixing chamber. As previously mentioned, the thermochemical calculations are not perfect. The heats of formation for the ingredients were calculated from group theory, and there are currently not any measured values for them. Even assuming the calculations used are correct, the mixing ratios have some unknown error. The ingredient ratios use to determine the theoretical propellant properties assume a perfect mix. Lastly, the phenolic liner for the mixing chamber likely participated in the combustion. It was not observed to be severely damaged, but it could contribute and impact the O/F ratio and potentially add energy and mass flow to the combustion. Before and after tests, the phenolic was not measured so the exact contribution cannot be known with certainty.

Figure 5.9 shows the dominant UPCs for c^* and η_c^* calculated using Equation 2.63. They share the same UPCs. The uncertainty in combustor pressure and the nozzle throat diameter accounted for the majority (70+%) of the known uncertainty in all the tests for both formulations. All of the other uncertainties that were accounted for fit in the remaining space. Errors from the thermochemical codes could not be estimated and are not included. The importance of pressure error decreases with an increase in pressure which occurs when moving to higher mass flow and temperature tests whereas the nozzle contribution increases.
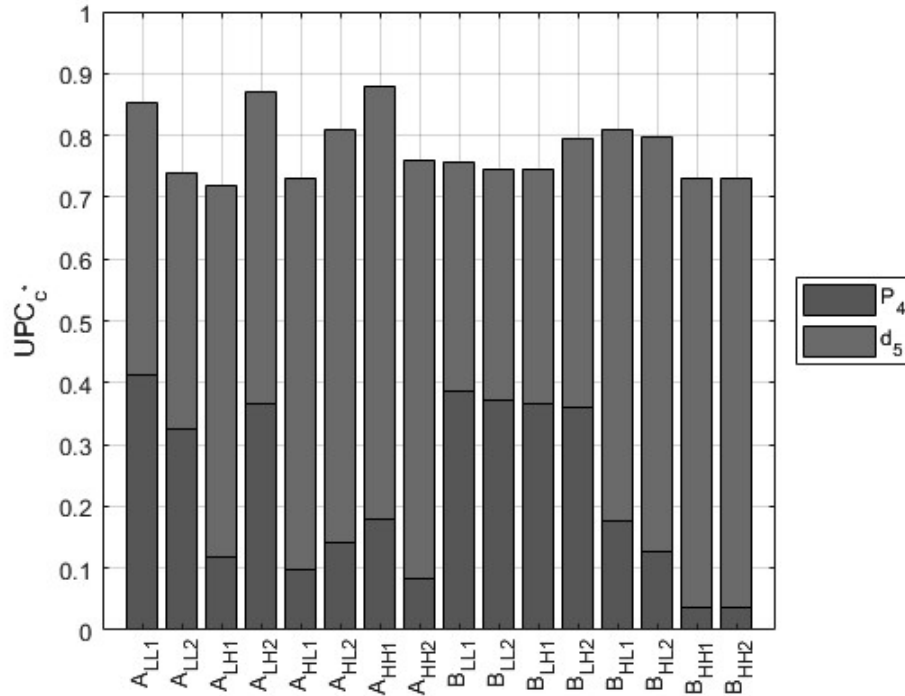
Figure 5.9: c^* UPCs

5.3.3 Conceptual Bias in Burn Time Determination

A major uncertainty in all of the performance parameters is the conceptual bias of the burn time. It is introduced by the selection of burn start and burn end methods [32]. To explore the effects of the conceptual bias, c^* vs O/F for both formulations were obtained using an 80% maximum pressure cutoff for both the start and end of the burn whereas a 10% maximum pressure the chosen method for this work. Plots illustrating the effects are shown in Figure 5.10 and Figure 5.11 for Formulation A and Figure 5.12 and

Figure 5.13 for Formulation B. The pressure traces with burn times for both methods may
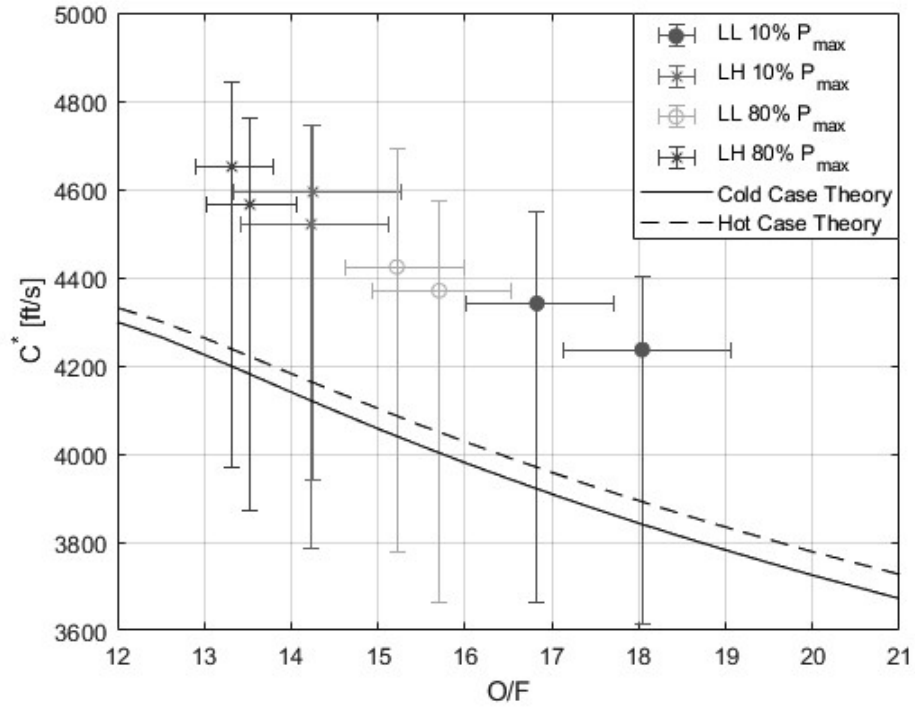
be seen in Appendix C.

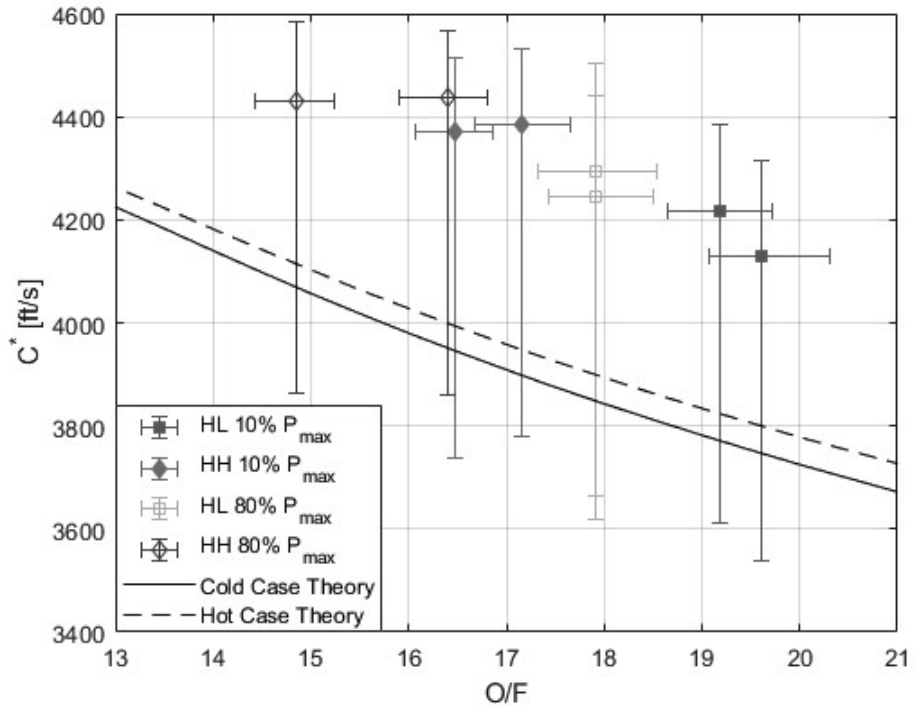Figure 5.10: Formulation A LL and LH Conceptual Bias in Burn Time

Figure 5.11: Formulation A HL and HH Conceptual Bias in Burn Time
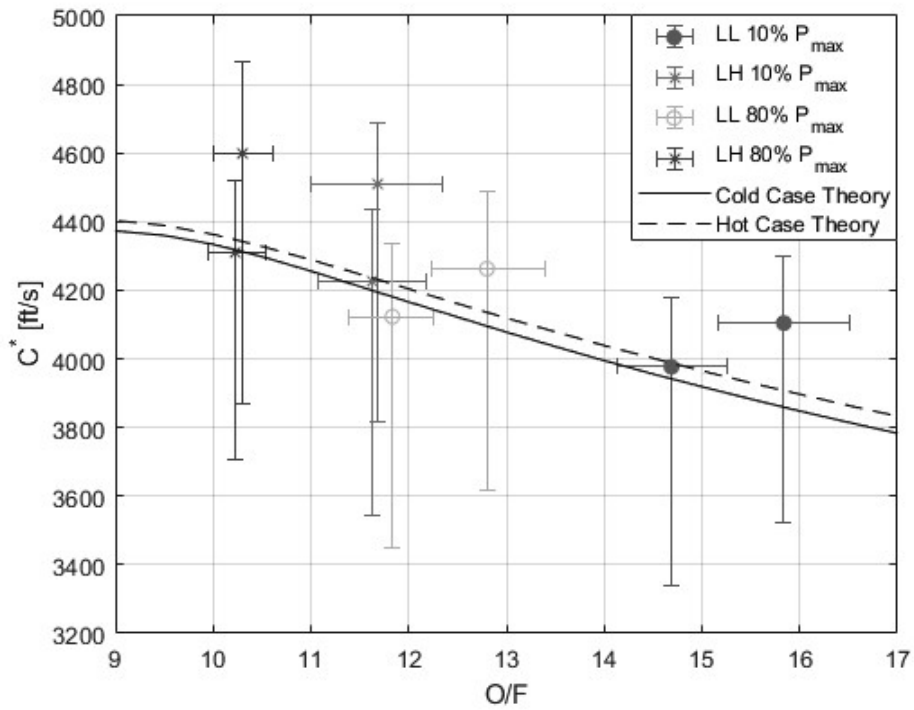

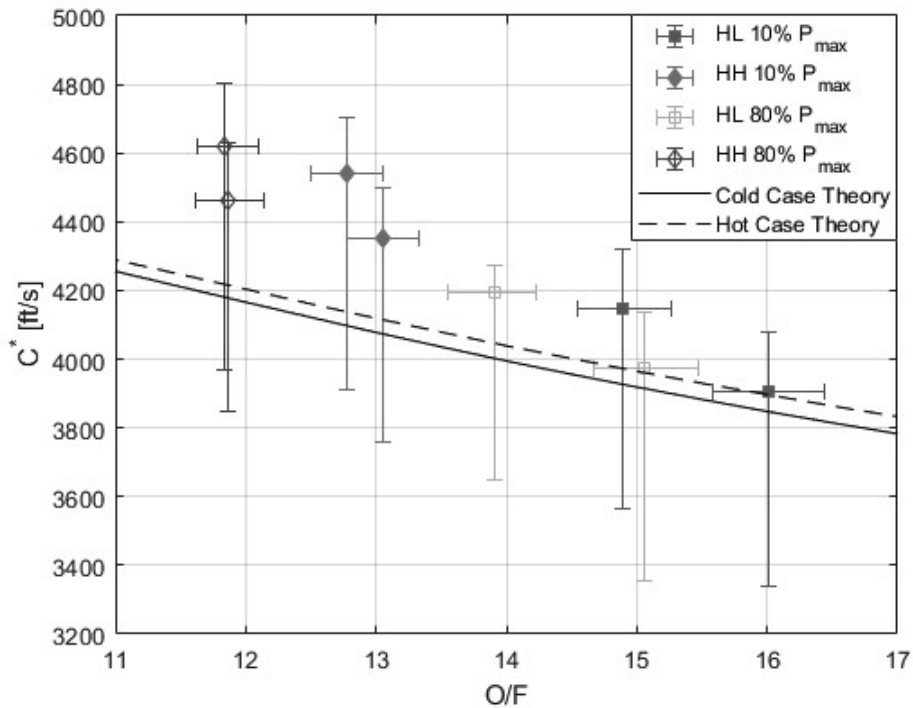Figure 5.12: Formulation B LL and LH Conceptual Bias in Burn Time

Figure 5.13: Formulation B HL and HH Conceptual Bias in Burn Time

In both formulations, the different burn time determination method made a large enough difference to force the 80% results outside of the uncertainty bands of the baseline data in most cases. Should a conceptual bias uncertainty taken from the plots presented be included as part of the uncertainty, they would overwhelmingly dominate all of the uncertainties investigated. As such, a bias term is not included in the list of errors, but its effects are demonstrated with the aforementioned plots. To mitigate the conceptual bias when comparing tests to one another, the same burning time method must be used on both.

The conceptual bias accounts for the error inherent in the selection of burn time determination method, but not in the error in selecting the times using the chosen method. It was found that there was no appreciable error in the chosen method (10% maximum pressure cutoffs).

5.3.4 Pressure and Thrust

The remaining performance parameters are based on thrust which has a large dependency on total pressure. It is directly present the equation for thrust. Table 5.4 shows the tabulated for chamber pressure and thrust. The ramjet nozzle throat area is present in the calculation for total pressure in the determination of Mach number (Equation 4.7) in the combustion chamber and in the formula for thrust (Equation 4.13).

Table 5.4: Total Combustor Pressure and Thrust Results

Test	p_{t4} [psia]	p_{t4} Lower Uncertainty [%]	p_{t4} Upper Uncertainty [%]	F [lbf]	F Lower Uncertainty [%]	F Upper Uncertainty [%]
A_{LL1}	33.59	-8.06	6.43	14.44	-24.89	8.15
A_{LL2}	34.53	-7.78	7.38	15.22	-25.52	9.48
A_{LH1}	36.95	-4.96	4.19	17.19	-21.07	5.48
A_{LH2}	36.47	-8.36	7.68	16.79	-25.46	9.50
A_{HL1}	54.00	-5.12	5.07	31.06	-17.61	6.35
A_{HL2}	55.05	-4.88	4.07	31.90	-17.23	5.30
A_{HH1}	58.87	-4.45	3.61	35.02	-16.12	4.24
A_{HH2}	58.83	-4.67	3.50	34.99	-16.94	4.21
B_{LL1}	34.16	-7.63	6.38	14.91	-26.27	9.43
B_{LL2}	32.70	-7.33	6.80	13.72	-24.42	9.70
B_{LH1}	34.58	-8.21	7.00	15.25	-26.17	9.19
B_{LH2}	36.84	-6.61	5.61	17.09	-23.17	6.99
B_{HL1}	51.46	-4.53	4.89	28.98	-17.86	6.22
B_{HL2}	55.04	-4.78	4.18	31.90	-16.89	5.34
B_{HH1}	58.99	-4.49	3.96	35.11	-16.07	4.51
B_{HH2}	61.56	-4.90	3.92	37.21	-15.95	4.61

Total pressure and thrust increase with an increase in air mass flow and air temperature. The larger factor is mass flow. The total pressure is not drastically sensitive to the throat area, but there is a minor influence. The thrust has a very skewed uncertainty band as a result of its sensitivity to the throat area. The plots of total pressure and thrust may be see in Figure 5.14 and Figure 5.15. From inspection of the figures, it may be seen

that in both formulations only a change in mass flow makes enough of a difference to overcome the uncertainty in the tests. The chamber pressures and thrust of both formulations are very similar, and with their expanded uncertainties, they are effectively identical.
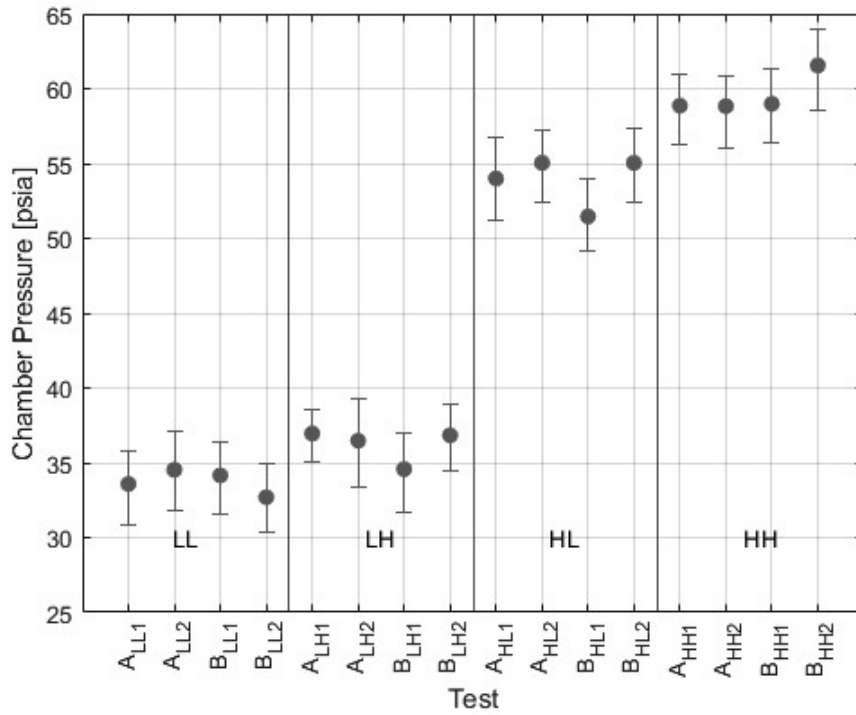

Figure 5.14: Total Chamber Pressure
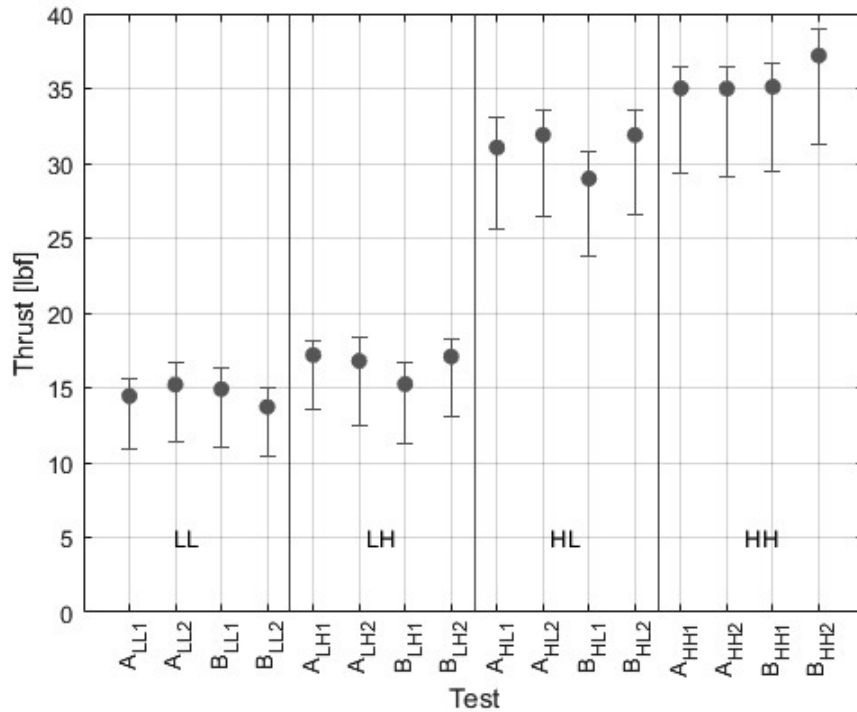
Figure 5.15: Thrust

Figure 5.16 shows the dominant UPCs for *F* calculated using Equation 2.63. Like with c^*, the uncertainty in combustor pressure and the nozzle throat diameter accounted for the majority (70+%) of the uncertainty in all the tests for both formulations. All of the other uncertainties that were accounted for fit in the remaining space. Like c^* the importance of pressure is generally inversely proportional to air temperature and air mass flow while the nozzle contribution is generally proportional to them.
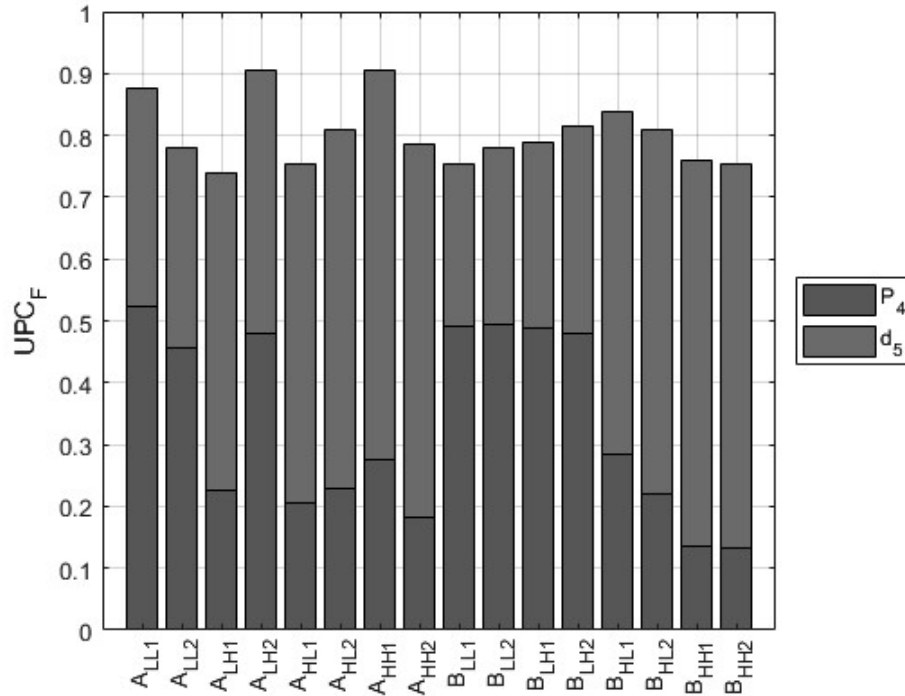
Figure 5.16: *F* UPCs

5.3.5 Specific Impulse and Vacuum Specific Impulse

Specific impulse and vacuum specific impulse were calculated with Equations 4.17 and 4.18. In both formulations an increase in mass flow increases both of their specific impulses. An increase in temperature had the opposite effect and reduced both of their specific impulses, but like pressure and thrust, the performance was dominated by the mass flow of air. Relative uncertainties for both decreased with an increase of mass flow and with temperature. Since the specific impulses are based on thrust, they are skewed by the corrective area distribution.

Table 5.5: Specific Impulse and Vacuum Specific Impulse Results

Test	I_{sp} [s]	I_{sp} Lower Uncertainty [%]	I_{sp} Upper Uncertainty [%]	$I_{sp,vac}$ [s]	$I_{sp,vac}$ Lower Uncertainty [%]	$I_{sp,vac}$ Upper Uncertainty [%]
A_{LL1}	1837	-25.89	9.82	3489	-14.66	6.47
A_{LL2}	1805	-25.92	10.16	3347	-14.64	6.15
A_{LH1}	1723	-21.39	5.69	3025	-12.76	3.75
A_{LH2}	1678	-26.24	9.03	2977	-15.41	5.08
A_{HL1}	2583	-17.37	6.84	3664	-12.21	5.06
A_{HL2}	2600	-17.30	5.44	3659	-12.55	4.03
A_{HH1}	2497	-16.46	4.71	3424	-12.27	3.77
A_{HH2}	2394	-17.04	4.19	3283	-12.52	3.11
B_{LL1}	1441	-26.33	9.53	2697	-14.35	5.44
B_{LL2}	1536	-24.91	10.20	2990	-13.52	6.04
B_{LH1}	1246	-27.06	10.37	2307	-15.31	6.48
B_{LH2}	1402	-23.31	7.09	2469	-13.50	4.18
B_{HL1}	1974	-17.83	6.07	2858	-12.40	4.33
B_{HL2}	2014	-17.05	5.80	2834	-12.12	4.24
B_{HH1}	1919	-16.26	4.66	2629	-12.03	3.55
B_{HH2}	1993	-16.06	4.69	2688	-11.98	3.57

Figure 5.17 and Figure 5.18 show the plots for the specific impulses. The trends described can be seen. Formulation A is shown to be superior at every set point. Both formulations do worse at their higher temperature set points than at their lower temperature ones for the same mass flow.
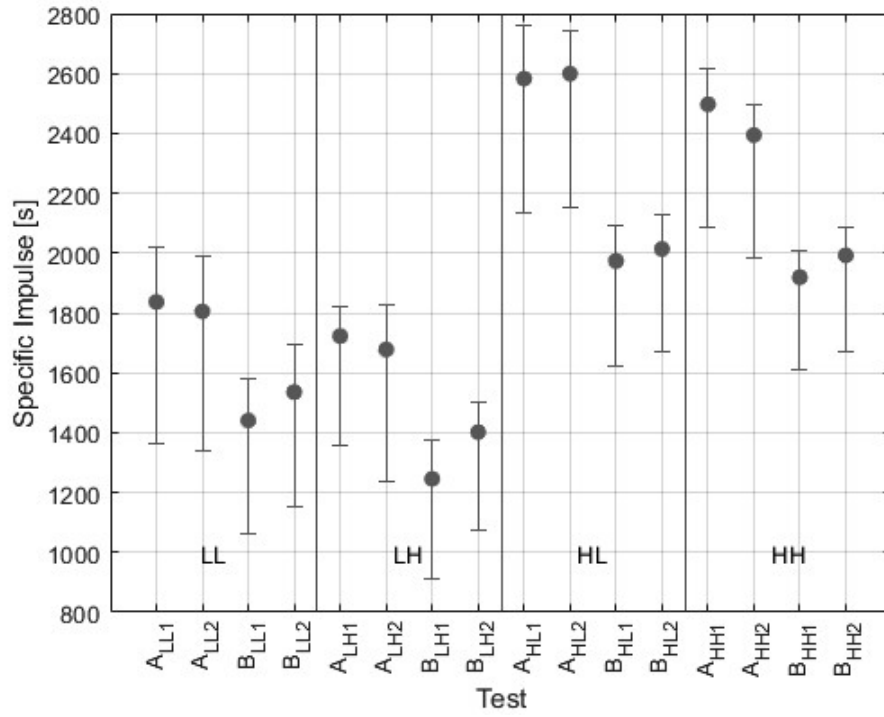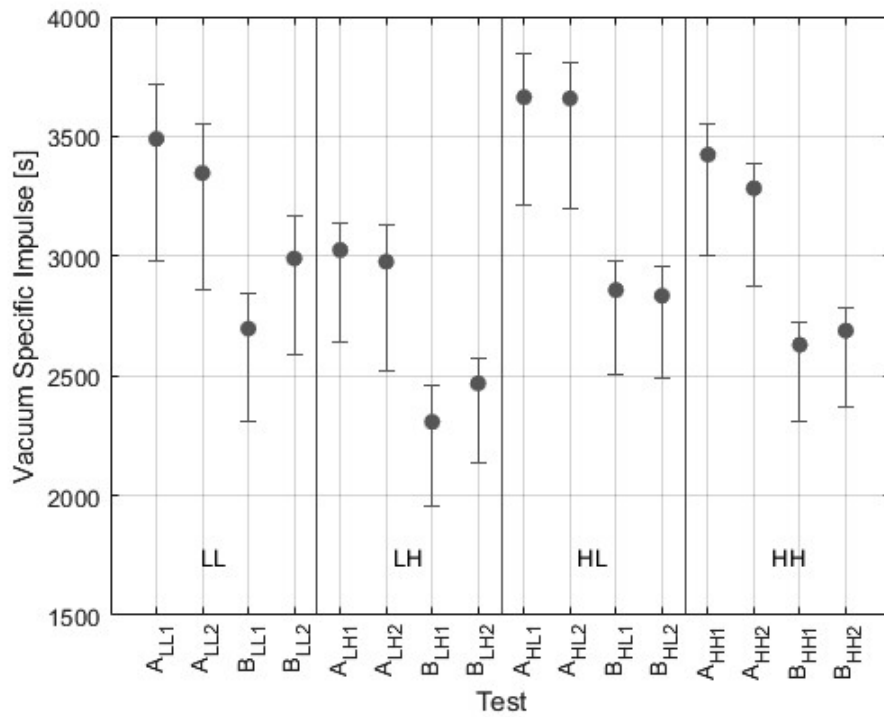
Figure 5.17: I_{sp}

Figure 5.18: $I_{sp,vac}$

100

Figure 5.19 shows the dominant UPCs for I_{sp} and Figure 5.20 for $I_{sp,vac}$. The uncertainty was dominated by the combustor pressure and nozzle like in previous performance parameters. Compared to thrust and characteristic velocity, the combustor pressure and nozzle have less effect.
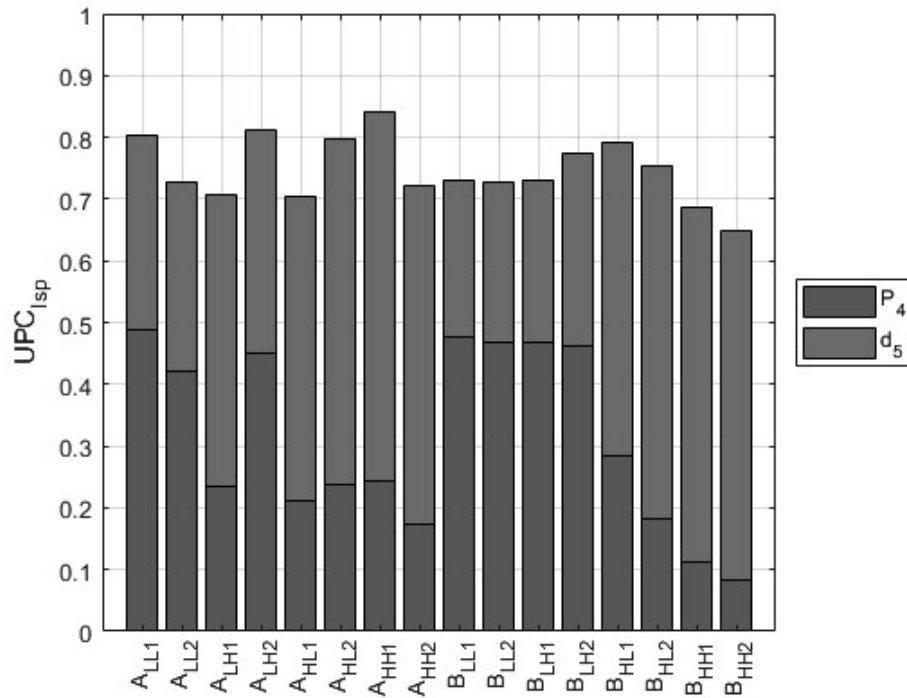

Figure 5.19: I_{sp} UPCs
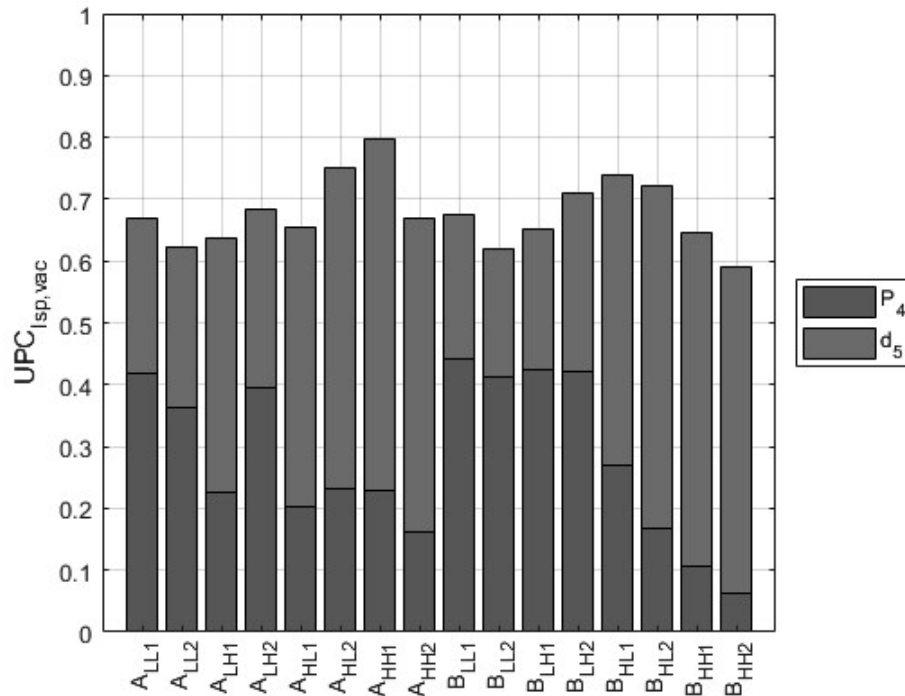
Figure 5.20: $I_{sp,vac}$ UPCs

5.4 Burn Rate and Equation

In addition to the performance parameters relating to combustion efficiency and thrust, the burning rate equation of the formulations were desired. The eight test firings for each formulation were used in a multiple linear regression to find the constants for the burning rate equation. The burning rate does not make use of any calculation involving the throat area and is therefore decoupled from the skewed uncertainty bands in the previous section. A summary of the mass fluxes, temperatures, and burn rates for tests is shown in Table 5.6. The uncertainty in the mass flux is larger than the mass flow due to the contribution of uncertainties from the geometry of the grain. However, the uncertainties for the mass flux and for the temperature are small. The uncertainty in the

burn rate is significant and dominated by the uncertainty in the grain geometry which is used to calculate the web burned.

Table 5.6: Ballistic Test Results

Test	$G_a \left[\dfrac{\text{lbm}}{\text{in}^2\,\text{s}}\right]$	G_a % Uncertainty	T_a [°F]	T_a % Uncertainty	$\dot{r} \left[\dfrac{\text{in}}{\text{s}}\right]$	$\dot{r}$ % Uncertainty
A_{LL1}	0.0526	0.91	665.3	0.78	0.0067	8.34
A_{LL2}	0.0522	0.89	664.0	0.78	0.0074	8.26
A_{LH1}	0.0516	0.88	791.7	0.80	0.0087	7.92
A_{LH2}	0.0518	0.88	791.0	0.87	0.0087	7.69
A_{HL1}	0.0842	0.85	664.4	0.78	0.0108	7.92
A_{HL2}	0.0843	0.87	661.3	0.81	0.0106	7.78
A_{HH1}	0.0852	0.88	766.5	0.82	0.0120	7.55
A_{HH2}	0.0846	0.87	770.2	0.86	0.0130	7.60
B_{LL1}	0.0565	0.91	665.3	0.80	0.0063	8.01
B_{LL2}	0.0529	0.93	674.3	0.82	0.0055	7.96
B_{LH1}	0.0524	0.90	794.9	0.85	0.0073	7.76
B_{LH2}	0.0524	0.88	805.5	0.87	0.0074	7.36
B_{HL1}	0.0852	0.82	664.4	0.77	0.0092	7.34
B_{HL2}	0.0850	0.83	668.7	0.79	0.0099	7.54
B_{HH1}	0.0849	0.83	779.7	0.86	0.0116	7.32
B_{HH2}	0.0856	0.84	794.7	0.84	0.0105	7.61

Figure 5.21 show the burn rate and their uncertainties for the tests. Overall, Formulation has a higher burn rate that Formulation B at the same set point. The burn rates are slow compared to solid propellants, which typically burn between 0.05-2 in/s [49]. The dominant UPCs are shown in Figure 5.22 which were the inner and outer diameters of the grain.
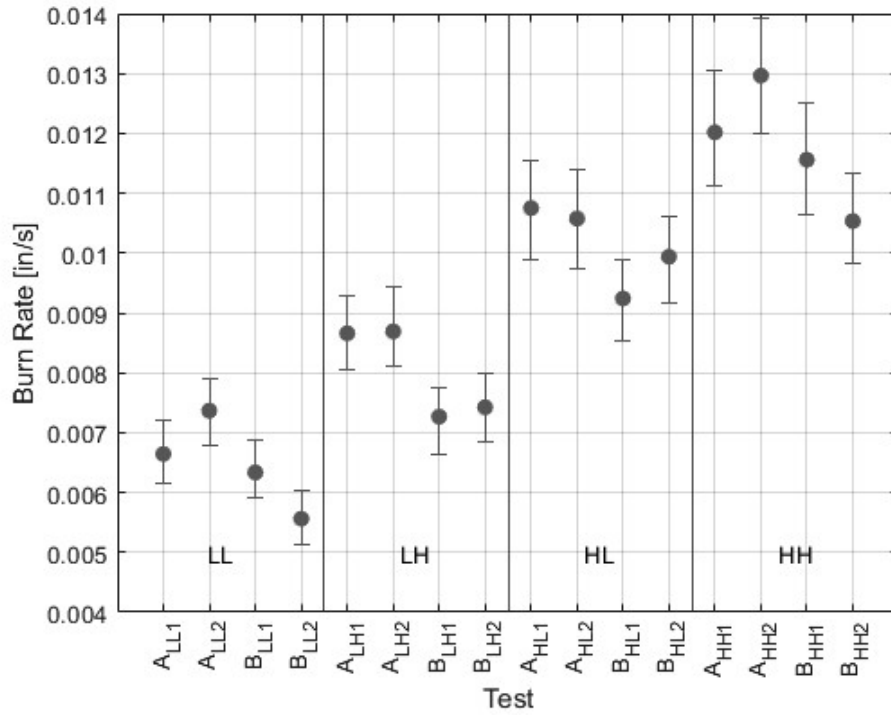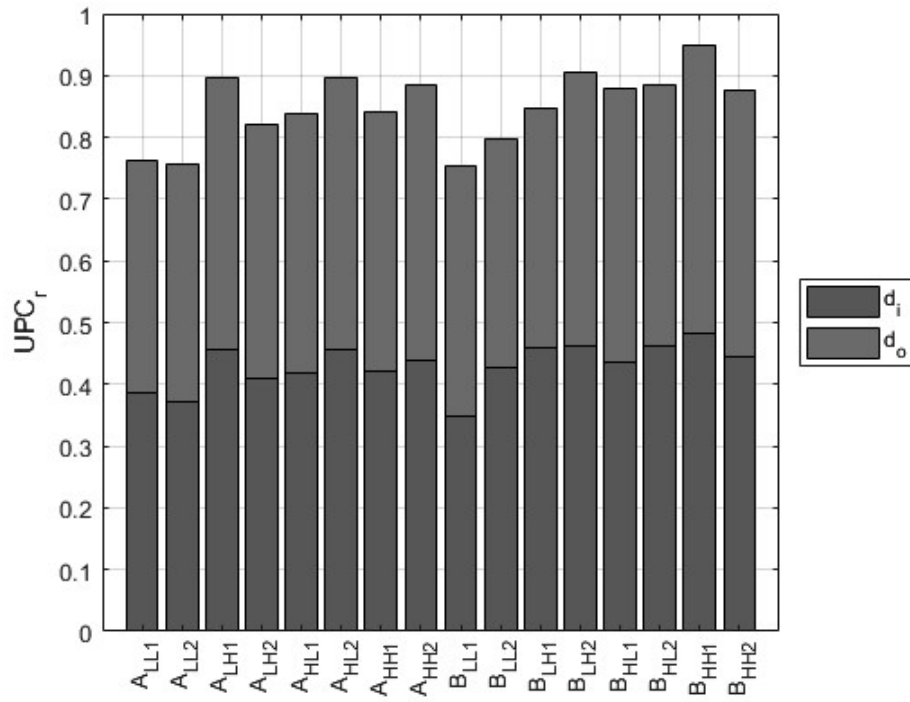
Figure 5.21: Burn Rate Uncertainty

Figure 5.22: Burn Rate UPC

A three-term burn rate equation was originally obtained with a low variance. However, the p values for the predictors, a measure of the probability that the observation was random, was very high. This made the three-term model ill-suited to this data set. Instead, a two-term model was chosen as shown in Equation 5.1. It had a low variance and low p values for the predicter variables. Like the three-term models, the constants were obtained using a multiple linear regression in the log space.

$$\dot{r} = aG_a^m T_a^q \qquad (5.1)$$

The Oxidizer mass flux and the temperature are the independent variables, and the regression rate is the measured outcome. The regression coefficient (a), mass flux of air exponent (m), and temperature of the air exponent (q) are determined by performing on at least three tests, and in this case, all tests for an individual propellant formulation.

Applying the regression to the burn rate constants in Table 5.7 were obtained. Formulation B exhibited a greater dependency on mass flux and Formulation A and the opposite is true for pressure. Compared to the three factor models presented in 2.4.3, the exponents are high. This is likely because the lack of a pressure term increases the significance of the two remaining terms for the model presented here. The other likely explanation is that the three factor models' propellants do not accurately compare to the two formulations presented here.

Table 5.7: Burn Rate Equation Constants

Formulation	$a \left[\dfrac{\text{in}^{2m+1}\text{s}^{m-1}}{\text{lbm}^m\,^\circ\text{F}^q}\right]$	m	q
A	2.3461E-05	0.7913	1.1162
B	2.9892E-05	0.9229	1.0887

To calculate the confidence intervals on the burn rate equations, the procedure outlined in 4.3.3 was utilized. Values for the uncertainty intervals were obtained at every test point. To interpolate between the points, a curve fit was constructed using Equation 5.1 which shares the same form as the burn rate equation. The formula is an exact fit for the eight data points provided. Two fits are used per burn rate equation, one for the upper and lower uncertainty interval. The values of for the constants are tabulated in Table 5.8.

$$\dot{r}_{conf} = aG_a^m T_a^q \qquad (5.1)$$

Table 5.8: Burn Rate Equation Confidence Intervals Constants

Confidence Interval	$a \left[\dfrac{\text{in}^{2m+1}\text{s}^{m-1}}{\text{lbm}^m\,^\circ\text{F}^q}\right]$	m	q
$\dot{r}_{A,+}$	2.3465E-05	0.7814	1.120
$\dot{r}_{A,-}$	2.4180E-05	0.7999	1.107
$\dot{r}_{B,+}$	3.0130E-05	0.9197	1.093
$\dot{r}_{B,-}$	2.8948E-05	0.9273	1.087

The burn rate equation, upper confidence intervals (+), and lower confidence intervals (−) for Formulation A are shown in Figure 5.23, Figure 5.24, Figure 5.25. The red dots on the plots indicate the test set points. The uncertainty intervals decrease with increasing mass flux and decreasing temperature. The uncertainty ranges between 4.0% - 4.6%.
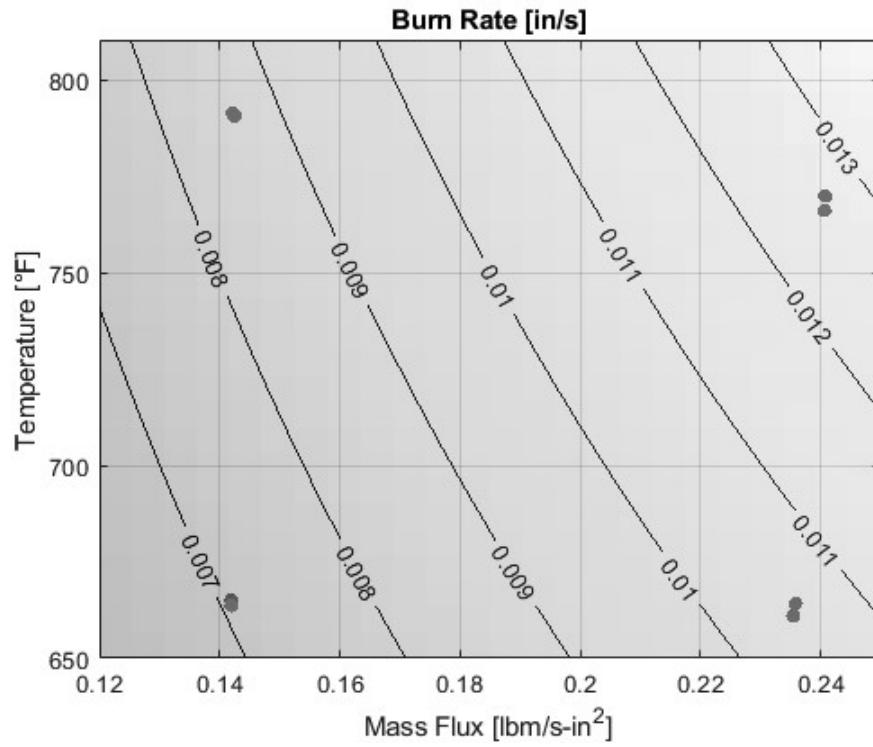
Figure 5.23: Formulation A Burn Rate Equation

Figure 5.24: Formulation A Burn Rate Equation Upper Confidence Interval

Figure 5.25: Formulation A Burn Rate Equation Lower Confidence Interval

The burn rate equation, upper confidence interval, and lower confidence intervals for Formulation B are shown in Figure 5.26, Figure 5.27, and Figure 5.28. The red dots on the plots indicate the test set points. Like Formulation A, the uncertainty decreases with increasing mass flux and decreasing temperature. The uncertainty ranges between 4.85% - 5.1%:
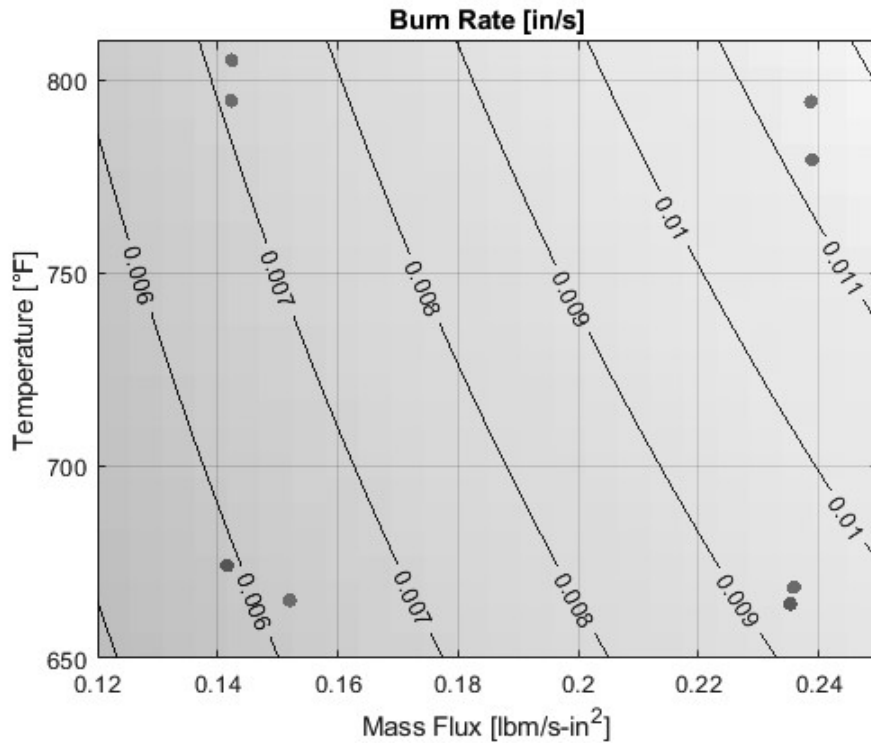
Figure 5.26: Formulation B Burn Rate Equation
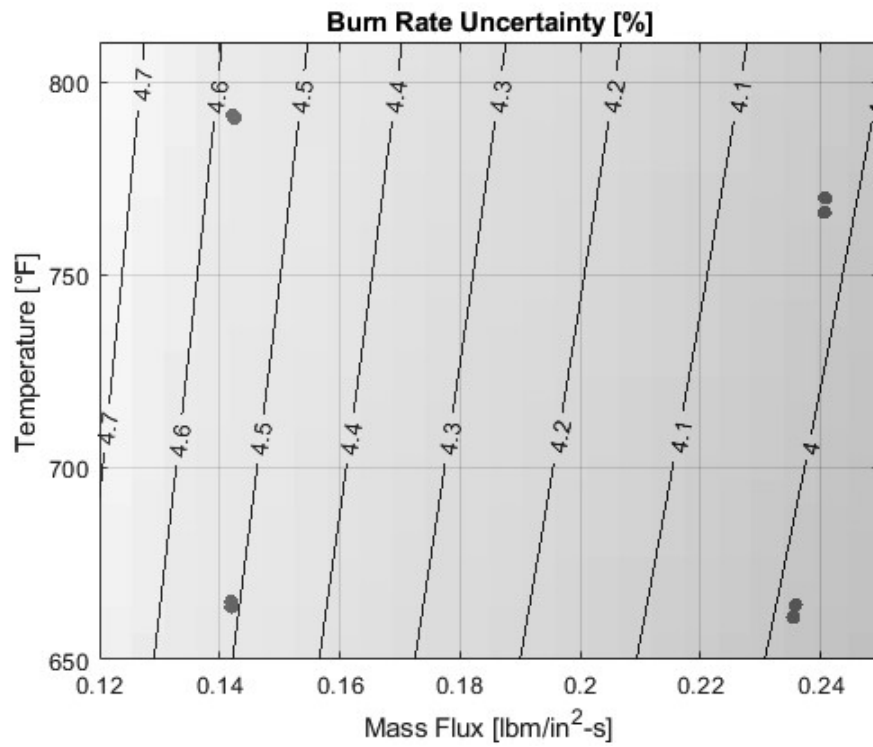

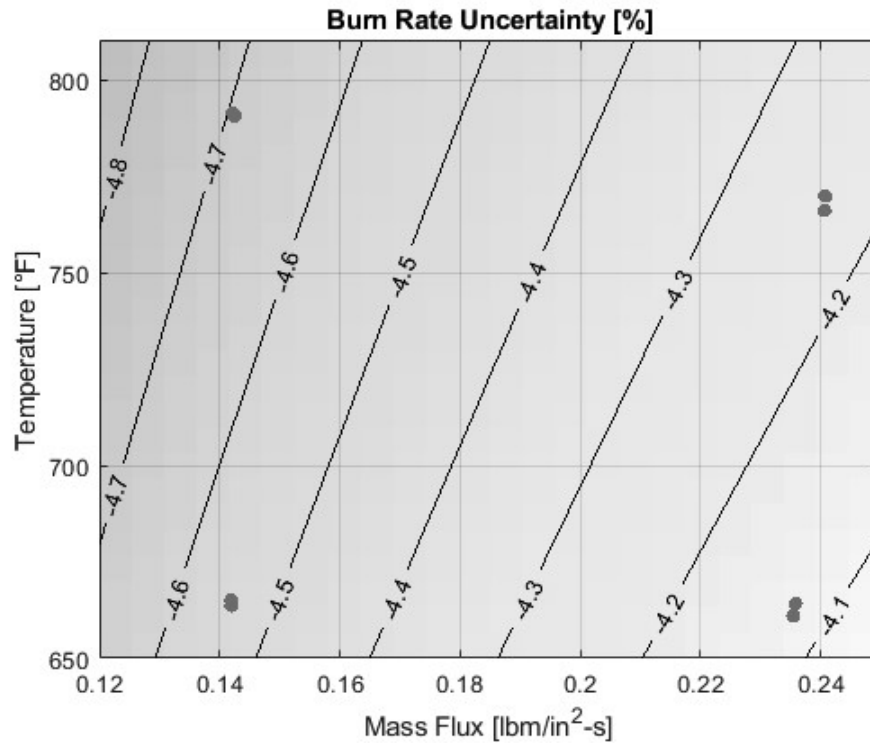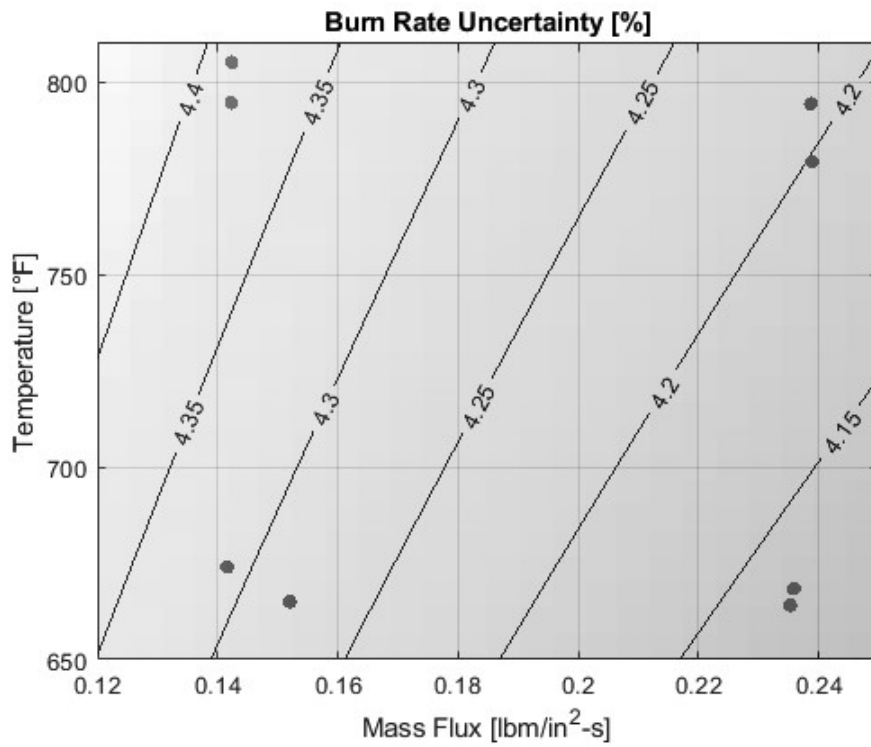Figure 5.27: Formulation B Burn Rate Equation Upper Confidence Interval
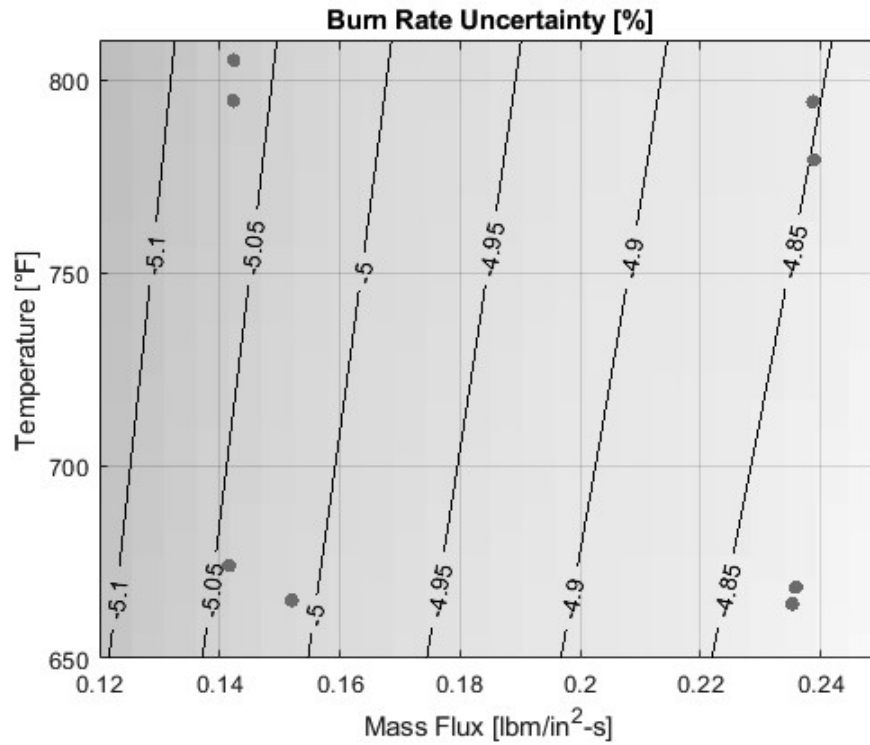
Figure 5.28: Formulation B Burn Rate Equation Lower Confidence Interval

Formulation A and B have roughly the same relative uncertainty at the set points, and similar confidence interval geometries. The uncertainty in Formulation B changes less across the interval than Formulation A. The uncertainty intervals are tighter that the uncertainties on the burning rates from the individual tests. The uncertainty intervals capture the possible variation in burning equation as opposed to the individual points.

CHAPTER 6

CONCLUSIONS

The goal of this work was to determine uncertainty estimates of characteristic velocity (c^*), characteristic velocity efficiency (η_{c^*}), thrust (F), specific impulse (I_{sp}), and vacuum specific impulse ($I_{sp,vac}$), specific impulse efficiency ($\eta_{i_{sp}}$) as well as burning rate (r), and a burning rate equation for a solid fuel ramjet test engine.. This was done using test data and applicable date reduction equations for two propellants in an ongoing research program at the PRC.

6.1 Performance Parameters

It was found that the difference in uncertainties between formulations was negligible. For a performance parameter, Formulation A and Formulation B effectively shared the same relative uncertainty.

The results show a c^* uncertainty of 17% - 20% for Formulation A tests and 18% - 19% for Formulation B tests. The uncertainty is the same for the η_{c^*}. The nominal values Formulation A were higher than Formulation B in all tests except for the second replication of the high temperature high mass flow set point. However, there was considerable overlap in their uncertainty intervals as shown in Figure 5.7. For the low mass flow tests, there was enough of a difference between the two confidence intervals, to conclude that Formulation A was superior from Figure 5.7. For the two high mass flow set points, a meaningful distinction cannot be made.

111

The uncertainties in η_{c^*} are the same as c^*. Like in c^*, the nominal values Formulation A were higher than Formulation B in all tests except for the second replication of the high temperature high mass flow set point. Unlike in c^*, there is a discernable difference between the propellant at every set point. The high mass flow high temperature set point had the most overlap.

The results show a F uncertainty of 20% - 35% for Formulation A tests and 21% - 36% for Formulation B tests. The differences in the propellant's uncertainty ranges are marginal. The two formulations were effectively indistinguishable with the uncertainty bands applied. The nominal values for the formulations are close for the same set points. This can be in Figure 5.15.

The results show a I_{sp} uncertainty of 21% - 36% for Formulation A tests and 21% - 37% for Formulation B tests. The $I_{sp,vac}$ uncertainty of 16% - 21% for Formulation A tests and 16% - 22% for Formulation B tests. The nominal values for both were better for Formulation A. This can be seen in Figure 5.17 and Figure 5.18. Formulation A stands out in both specific impulses even with uncertainty bands applied, though there is still overlap. At the low mass flow set points, there is the most overlap between them. At the high mass flow set points, the overlap is minimized and, in some tests, eliminated. The superior specific impulse performance comes from its lower weight. The thrust both propellants delivered was effectively the same, but Formulation A was the lighter of the two.

In all of Formulation A and seven tests of Formulation B, the c^* values were higher than their theoretical predictions. This also makes their η_{c^*} greater than 1. The one test in Formulation B that is not greater than its theoretical value is still very close to it. In general,

112

this is irregular. Losses are expected in a propulsion system such as energy losses to heat transfer into the walls of the motor. The aft pressure transducer was cross checked with other pressure transducers to verify its valid operation. Slag deposits were observed in the nozzle throat during testing, and it is believed that they elevated c^*. A smaller nozzle throat would have increased the pressure. The nominal values for c^* do not include any corrections for the slag deposits since no measurements of the throat diameter or area were taken during the tests for which the increase in pressure cannot accurately be compensated.

A correction in the uncertainty analysis was applied to demonstrate the effects of a clogged nozzle. The correction skewed and grew the uncertainty intervals for c^* as well as lowering all of the other performance parameters. After the correction was applied, the lower portion of the c^* uncertainty intervals were below their theoretical values. While needed to bring down the η_{c^*}, the correction factor applied to the nozzle throat diameter, was a dominant uncertainty source as evidenced by all of the performance parameter UPCs.

For c^* and η_{c^*}, the dominant uncertainties were in combustor pressure p_4 and the nozzle throat diameter d_5 This is shown by the UPCs in Figure 5.9. In all cases these account for over 70% of the uncertainty present in the calculation. To improve the uncertainty in the measurement, one of these uncertainties needs to be addressed. The easiest would be to measure the value of either the diameter or area of the nozzle throat between each test.

The nominal values measure for c^*, while high, did follow the trend of the theoretical data as shown in Figure 5.5 and Figure 5.6. Taking the uncertainty bands into account, it is difficult to prove such a trend. The wide uncertainty bands allow trends to be fit that are in disagreement with the theoretical data. However, the channel formed by

113

taking trendline of the upper confidence intervals and a trendline of the lower confidence intervals follows the theoretical trend.

The O/F for the tests frequently overlapped one another. In Formulation A the LL and HH sets overlapped in both O/F and c^*. In Formulation B the LL and HL sets did the same. The uncertainties in the O/F were between 2.1% - 5.4% which are not enormous. In the tests where considerable overlap is present, it is difficult/impossible to determine the effects of their set points on c^*. More accurate testing could help to resolve this issue.

The dominant uncertainties in thrust were the chamber pressure and nozzle throat diameter due the correction as shown by the UPCs in Figure 5.16. The total range of uncertainty in thrust was large. The relative uncertainties decreased with an increase in either air temperature or air mass flow. The decrease in relative uncertainty at a higher thrust shows the uncertainties are of relatively constant value. It is easier to measure a higher value of thrust.

Much like thrust, uncertainty in the specific impulses is driven by the uncertainties in the combustor pressure and nozzle throat. The specific impulses have a third major uncertainty which is the uncertainty in the mass of propellant burned. Vacuum specific impulse is more sensitive to this as evidenced by the UPCs in Figure 5.19 and Figure 5.20. The relative uncertainties in I_{sp} and $I_{sp,vac}$ decreased with an increase in either setpoint air temperature or air mass flow like F and c^*. The uncertainties are of relatively constant magnitude, so an increase in the specific impulses decreases relative uncertainty.

The uncertainty ranges of I_{sp} are the same as F. The uncertainty ranges for $I_{sp,vac}$ are smaller than both. This is due to low uncertainty in the second term of Equation 2.8 that adjusts the specific impulse to vacuum level. The boost in specific impulse without a

proportional increase in uncertainty, decreases the relative uncertainty in $I_{sp,vac}$. The absolute uncertainty did not decrease.

Overall, it was possible to discern between the formulations in for all tests in η_{c^*}, I_{sp} and $I_{sp,vac}$ and half of them in c^*. It was not possible to discern between the F tests and the high mass flow c^* tests of the formulations.

6.2 Burn Rates and Equations

The dominant uncertainties of the burn rates were the grain diameters as shown by the UPCs in Figure 5.22. The uncertainty ranged from 7.3% - 8.3%. The temperature and mass flux measurements were found to have low uncertainties (<1%) as shown in Table 5.6. The burn rates were decoupled from the errors in c^* and the other performance parameters. The burn rates are a function of grain geometry and mass of the propellant before and after a test firing. The burn rates are accurate for the combustor conditions they endured which was accurately captured by the mass flow meters, thermocouples, and pressure transducers. The troublesome nozzle throat does not appear in the burn rate or burn rate equations.

A burn rate equation with predictors in air mass flux and air temperature was constructed for both formulations. The test data did not support a standard three term model with predictors in pressure, temperature, and mass flux. A three-term equation with a low variance could be fit, but the p values were very high. The two-term model provided a low variance and low p values. The burn rate equation exponents were similar to the values predicted by Netzer and Gany [37].

Uncertainty intervals on the burn rate equations were determined. It was found that burn rate equation uncertainties at the test points between 4.0% - 5.1%. The uncertainty on the burn rate equation was lower than the uncertainties of the burn rates. The uncertainties between test points were lower than at the test points. The uncertainty grew when extrapolated past the test points. The equation for the uncertainty intervals is shown in Equation 5.1 with values for the constants shown in Table 5.8.

The choice of fit for the burn rate equations confidence intervals was chosen to provide a good representation at the test points where data was available. Data in the middle of the test points is required to flesh out the uncertainty intervals. With just the four test set points at the corners of the uncertainty intervals, the geometry in the middle of the surface is ill defined.

6.3 Future Work and Recommendations

The data presented in this thesis is part of an ongoing test program. The following recommendations are made to improve the quality results obtained from future tests.

Slag is thought to be possible reason for abnormally high measured c^* values. These issues could have been resolved if a measurement of the throat diameter or the throat area had been taken between tests. It is recommended that this becomes standard procedure for future tests. Procedures also need to be implemented to keep the transducers clear of slag. Having accurate nozzle throat areas would reduce the uncertainty of the nozzle by 64%.

Temperature and age effects of the combustor pressure transducer was not included in the calibration uncertainty. The transducer was calibrated two years ago. Recalibrating

before a test within a month or two could drastically reduce the amount of age-related uncertainty present. Temperature effects would be the hardest remove. Heating up the transducer while applying a known pressure could allow for a temperature response of the transducer to be obtained. Removing these errors could reduce the transducer uncertainty by up to 45%.

The choice of burn time method introduced a conceptual bias. It was found that using a conservative estimate of bias of 10% maximum pressure - 80% maximum pressure for the burn time method causes the conceptual bias to dominate the uncertainty in the performance parameters. The 10% maximum pressure was believed to the good method for this data and was used. Further study and method for the determination of the conceptual bias is required to form an accurate estimate. Burn time bias is likely a strong factor and warrants further investigation.

Values for the discharge coefficients of the ramjet nozzle, sonic nozzle, and igniter gas orifice need to be obtained for the temperatures and pressures that they experience. The ramjet nozzle is the most important of these since it has the largest impact. Alternatively, a pressure tap could be placed at the throat. Direct knowledge of the throat conditions eliminates the need for the discharge coefficient. Knowledge of the sonic nozzle discharge coeffect could allow the nominal values of the Coriolis flow meter and the sonic nozzle to be brought into a tighter agreement.

The flow meter had a rhythmic disturbance in all of its data that did not obviously appear to be combustion instability. Further investigation on this could reveal instabilities in the system not previously known.
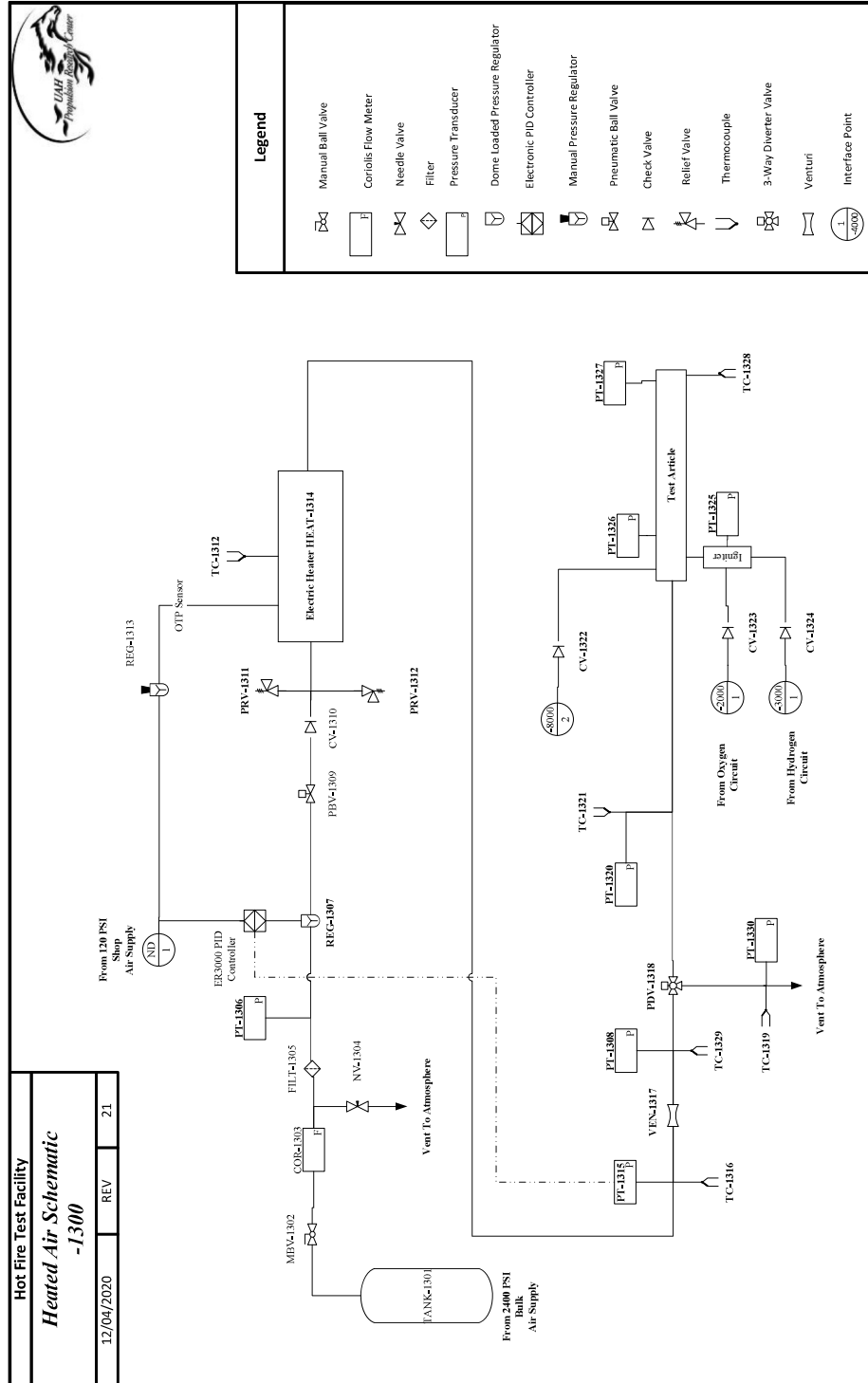
APPENDIX A: PRC FACILITY SETUP
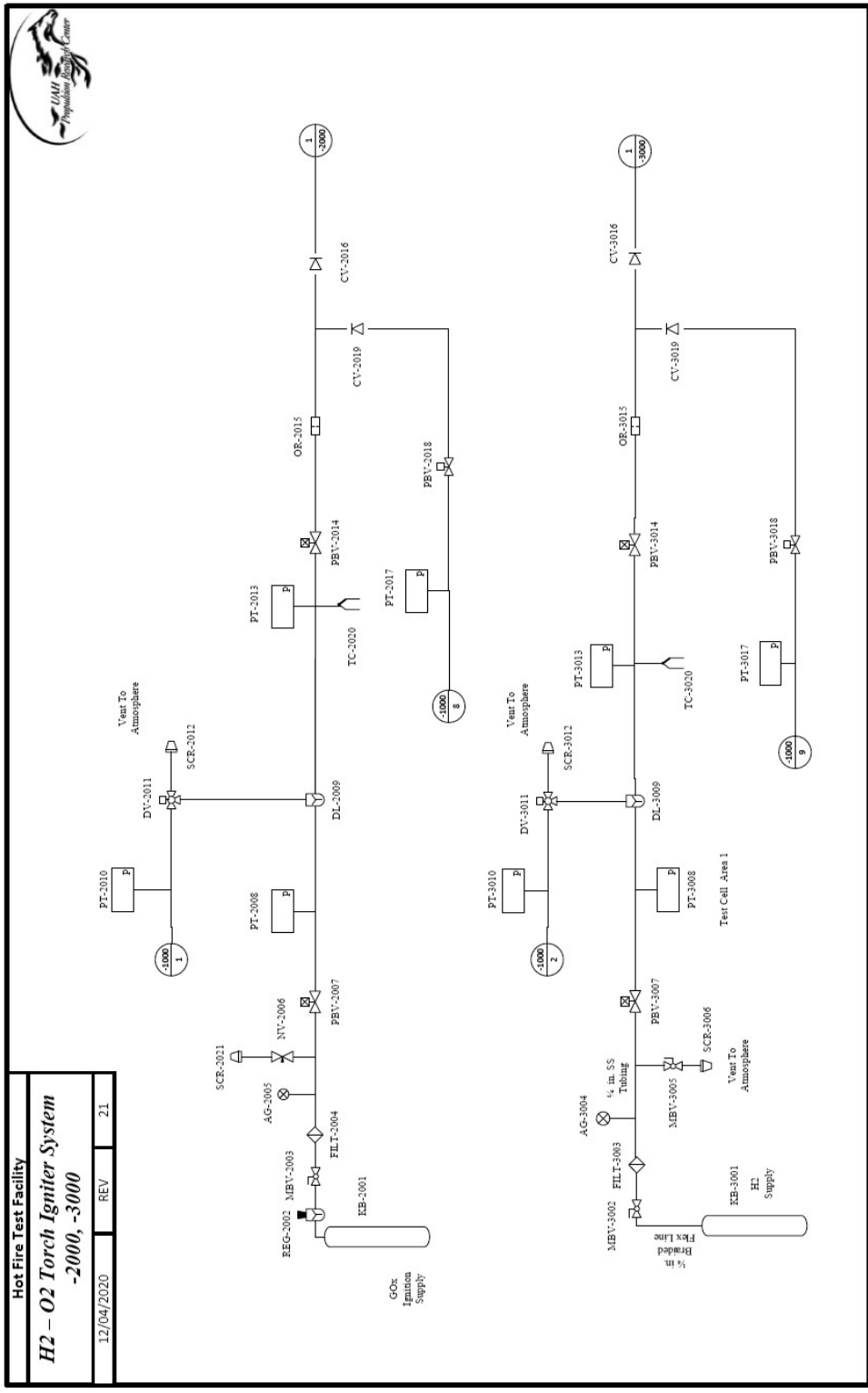

Figure A.1: PRC Heated Air Schematic [44]

Figure A.2: PRC Torch Igniter Schematic [44]

Table A.1: SFRJ Test Cell Schematic Sensor Numbers

| Designation	Model	Name
PT-1306	Unik 5000	Filter Transducer
PT-1315	Unik 5000	Sonic Nozzle Transducer
PT-1320	Unik 5000	Port Connector Transducer
PT-1326	Unik 5000	Head End Transducer
PT-1325	Unik 5000	Ignitor Transducer
PT-1327	Unik 5000	Aft End Transducer
PT-1330	Unik 5000	Dump Transducer
PT-1308	Unik 5000	PVT Transducer
TC-1319	Omega K Type	Dump Thermocouple
TC-1312	Omega K Type	Heater Body Thermocouple
TC-1316	Omega K Type	Sonic Nozzle Thermocouple
TC-1321	Omega K Type	Port Connector Thermocouple
TC-1328	Omega K Type	Aft Thermocouple
HEAT-1314	Tutco-SureHeat: SFI-3D-48-48	Electric Heater
VEN-1317	FlowMaxx	Sonic Nozzle
COR-1303	Micro Motion Elite CMFS025P	Coriolis Flow Meter
PDV-1318	PBM PAVCL453S-0085	Diverter Valve
OR-2015		Oxygen Orifice
OR-3015		Hydrogen Orifice
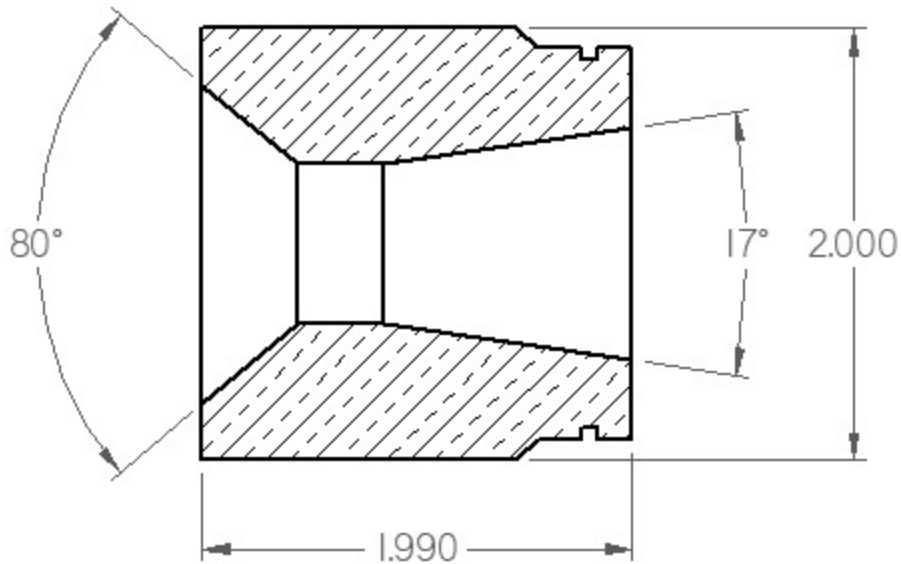
Figure A.3: Nozzle Drawing

APPENDIX B: THEORETICAL PROPELLANT PROPERTIES

The theoretical performances and properties of the two formulations were calculated in Chemical Equilibrium in Excel (CEQUEL) a thermochemical solver in Microsoft EXCEL based on NASA's Chemical Equilibrium with Applications (CEA). The rocket problem option calculated combustion and thermodynamics properties of the combustion gases for each propellant at the two test matrix temperatures and over a range of oxygen to fuel ratios. Equilibrium flow in the nozzle analysis was assumed.

The densities for the propellants are shown in Table B.1. Formulation B is the denser of two propellants and is 34% heavier than Formulation A. The theoretical densities are high water marks which are difficult to obtain in practice.

Table B.1: Theoretical Densities

Propellant	Density [lbm/ft^3]
A	64.47
B	86.96

The characteristic velocity vs oxidizer to fuel ration (O/F) for the two propellant combinations are shown in Figure B.1 and Figure B.2. Formulation A has its stoichiometric O/F, the point of maximum c^*, at a higher O/F than Formulation B. In both formulations, an increase in air temperature increases the characteristic velocity as a result of more energy being brought into the combustion chamber. Formulation B has a slightly higher ($< 1.5\%$) maximum c^* for both air temperatures analyzed. When burning fuel rich (lower O/F), Formulation B has a higher c^* with second peak at around O/F at

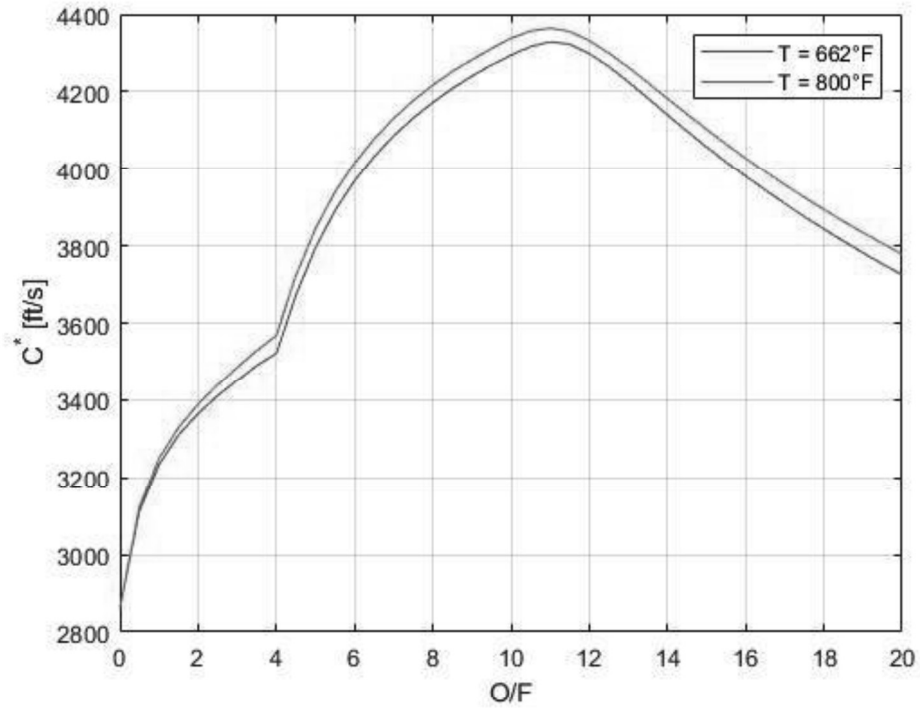3.5. When burning lean (higher O/F), Formulation A has a higher c^* since it tapers off slower.
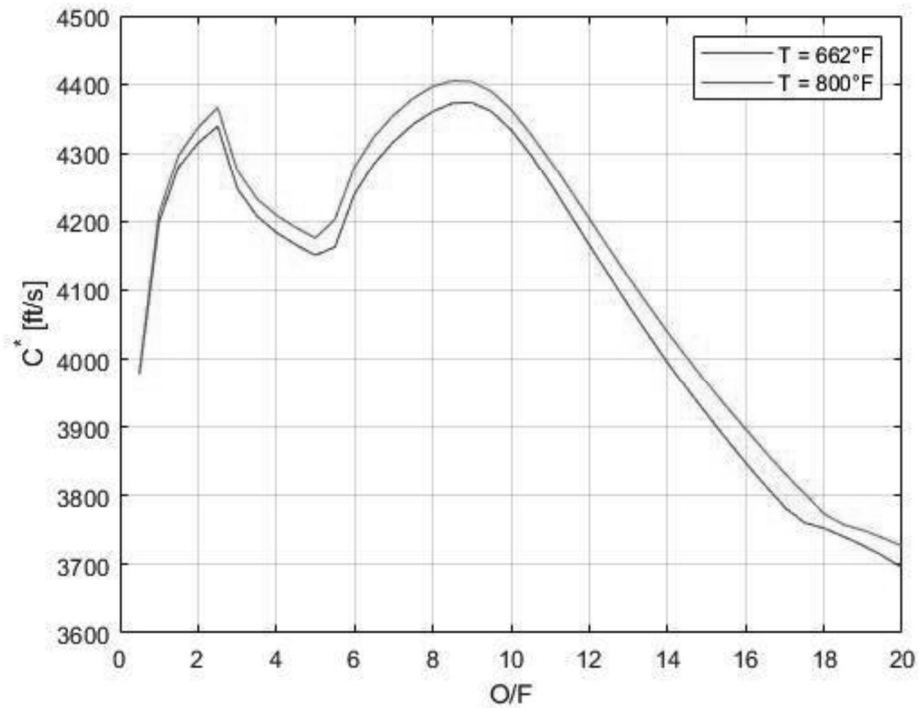

Figure B.1: Formulation A C^* vs O/F

Figure B.2: Formulation B C^* vs O/F

The specific heat ratios, γ, for each formulation are shown in Figure B.3 and Figure B.4. In both propellants, the difference of air temperature between test set points makes almost no difference with the most divergence at the lean end of the spectrum. The range of values for the specific heats is not huge especially considering the insensitivity of the reduction equations to them. Excepting the lowest end of the O/F range, the two formulations follow very similar curves with similar values. During the data reduction process, the ratio of specific heats in the combustor is determined from these plots.
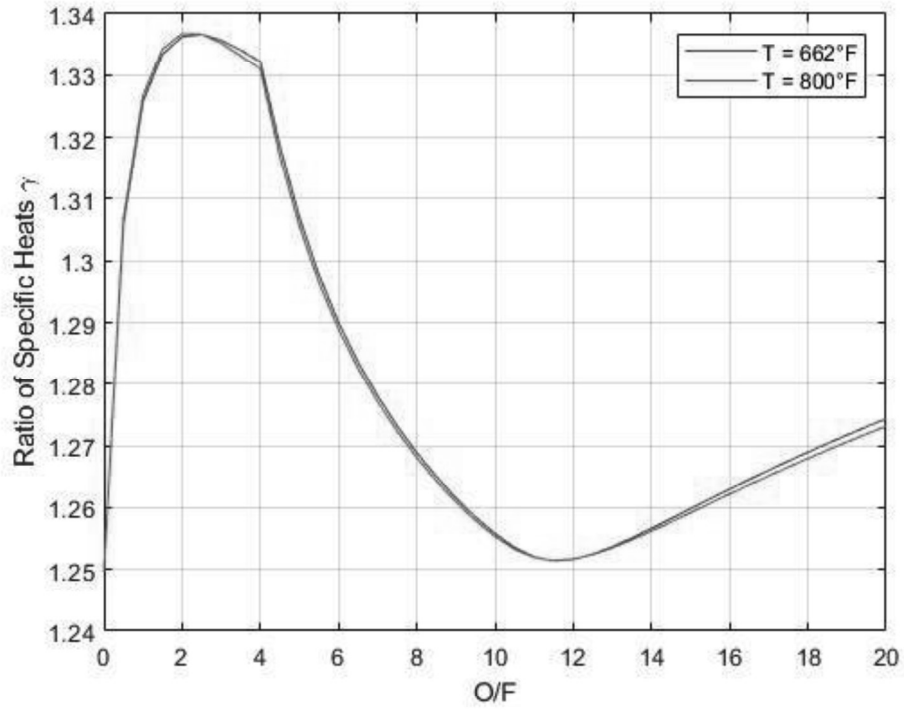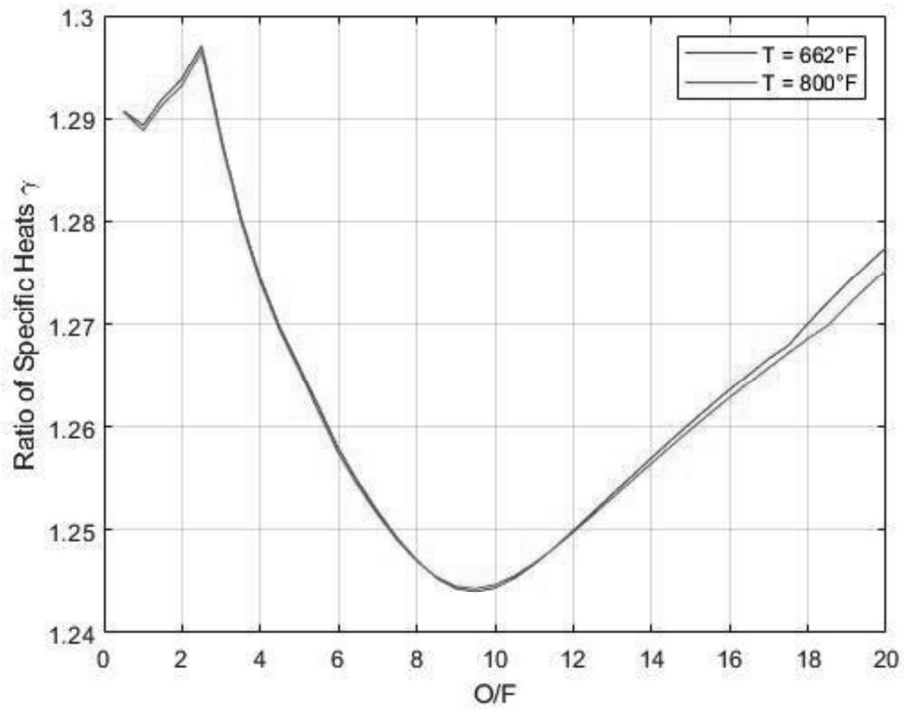
Figure B.3: Formulation A γ vs O/F

Figure B.4: Formulation B γ vs O/F

APPENDIX C: TEST DATA

Table C.1: Common Pretest Data

Property	Value	Units	Lower Confidence Bound	Upper Confidence Bound
d_i	1.80	in	1.79	1.81
d_o	2.00	in	1.99	2.01
L	per Test	in		
t_{ign}	per Test	s	+0.05	+0.45
d_5	0.873	in	0.759	0.863
d_6	1.07	in	1.06	1.08
θ	15	deg	14	16
c_{D5}	0.99	-	0.98	1.00
d_{noz}	0.255	in	0.254	0.256
$c_{D,noz}$	0.975	-	0.95	1.00
R_a	1717	$\dfrac{\text{ft lb}}{\text{slug °R}}$	-	-
p_∞	14.465	psia	14.460	14.470
γ	I	-	-1%	+1%
d_{O2}	0.040	in	0.0399	0.0401
d_{H2}	0.038	in	0.0379	0.0381
$c_{D,O2}$	0.97	-	0.94	1.00
$c_{D,H2}$	0.97	-	0.94	1.00
T_{O2}	44	°F	34	54
T_{H2}	44	°F	34	54
R_{O2}	1554	$\dfrac{\text{ft lb}}{\text{slug °R}}$	-	-
R_{H2}	24633	$\dfrac{\text{ft lb}}{\text{slug °R}}$	-	-

Table C.2: Grain Masses and Lengths

| Test	m_{liner} (lbm)	m_{assy} (lbm)	m_{post} (lbm)	L (in)
A_{LL1}	0.117	0.234	0.174	5.906
A_{LL2}	0.117	0.234	0.166	5.669
A_{LH1}	0.117	0.234	0.150	5.945
A_{LH2}	0.117	0.234	0.152	5.906
A_{HL1}	0.117	0.238	0.130	5.669
A_{HL2}	0.117	0.230	0.135	5.788
A_{HH1}	0.117	0.234	0.121	5.630
A_{HH2}	0.117	0.230	0.113	5.630
B_{LL1}	0.117	0.285	0.201	5.945
B_{LL2}	0.117	0.282	0.210	5.669
B_{LH1}	0.117	0.289	0.188	5.945
B_{LH2}	0.117	0.285	0.185	5.591
B_{HL1}	0.117	0.278	0.159	5.630
B_{HL2}	0.117	0.278	0.150	5.788
B_{HH1}	0.117	0.276	0.128	5.630
B_{HH2}	0.117	0.296	0.146	5.945
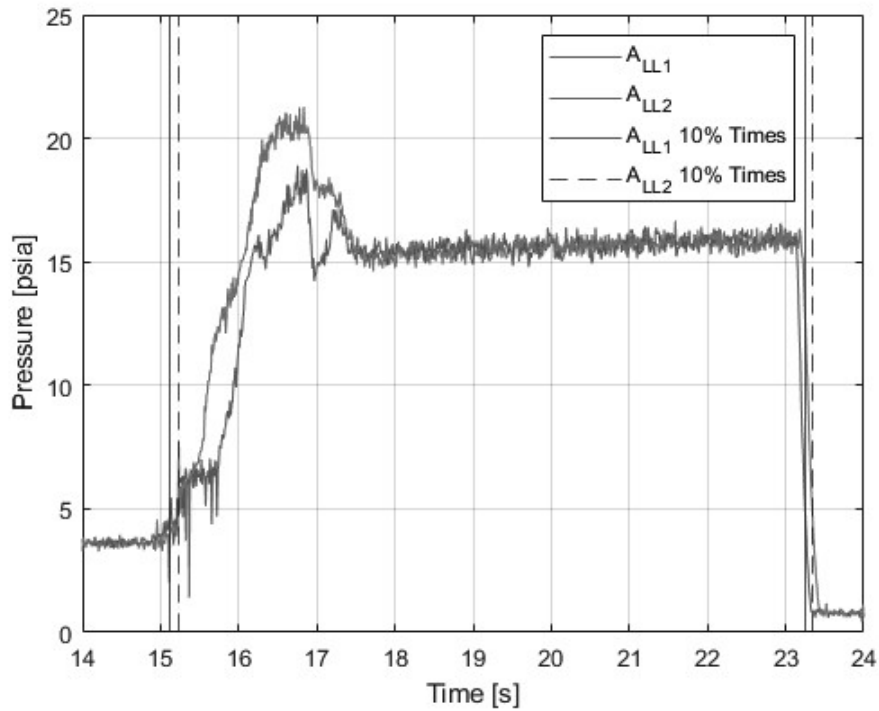
Figure C.1: A_{LL} with 10% P_{max} Times

Figure C.2: A_{LL} with 80% P_{max} Times

Figure C.3: A_{LH} with 10% P_{max} Times

127

Figure C.4: A_{LH} with 80% P_{max} Times

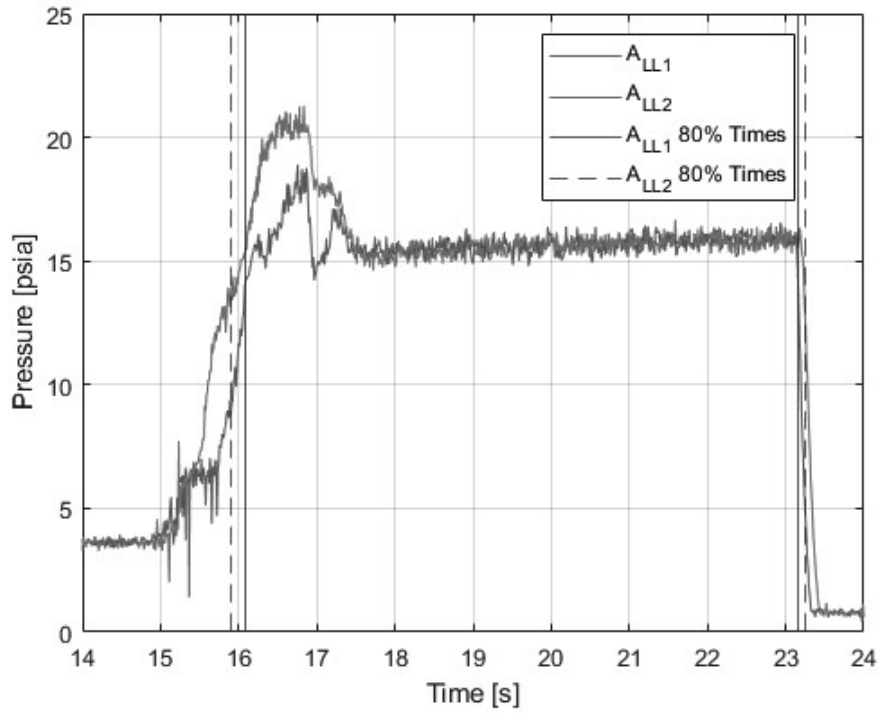Figure C.5: A_{HL} with 10% P_{max} Times

Figure C.6: A_{HL} with 80% P_{max} Times
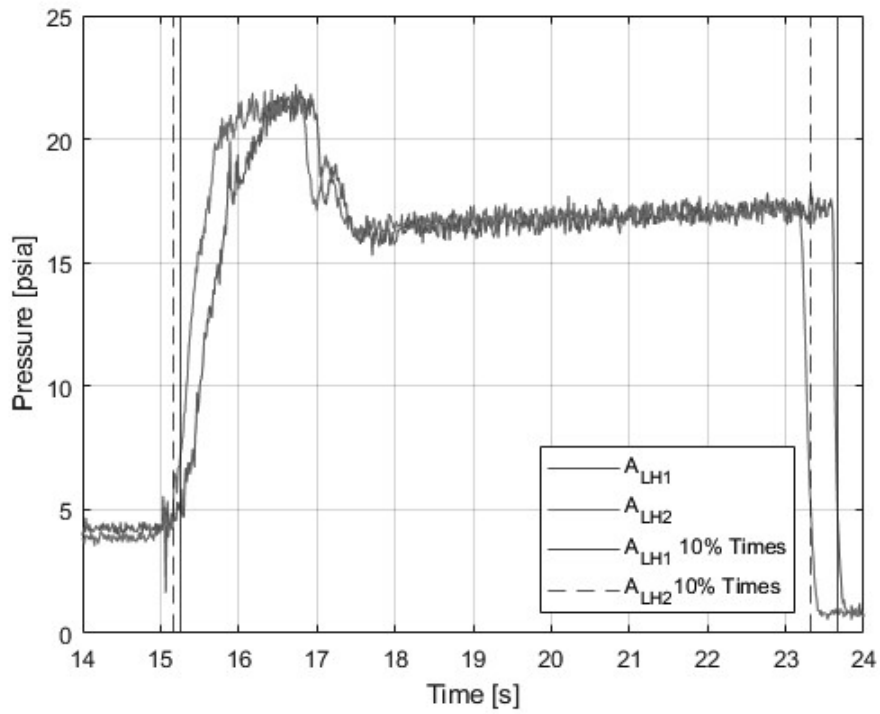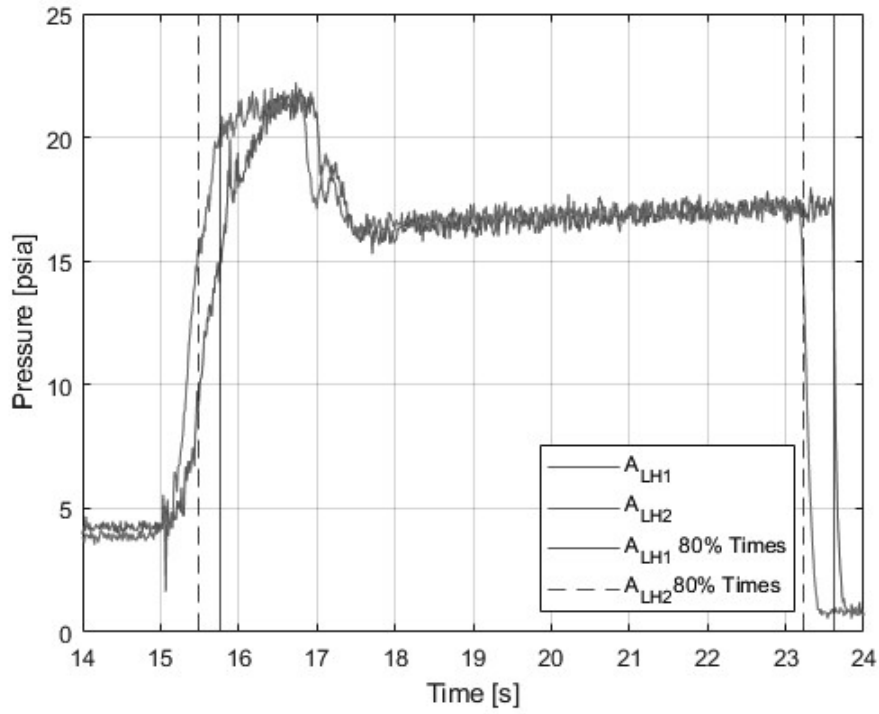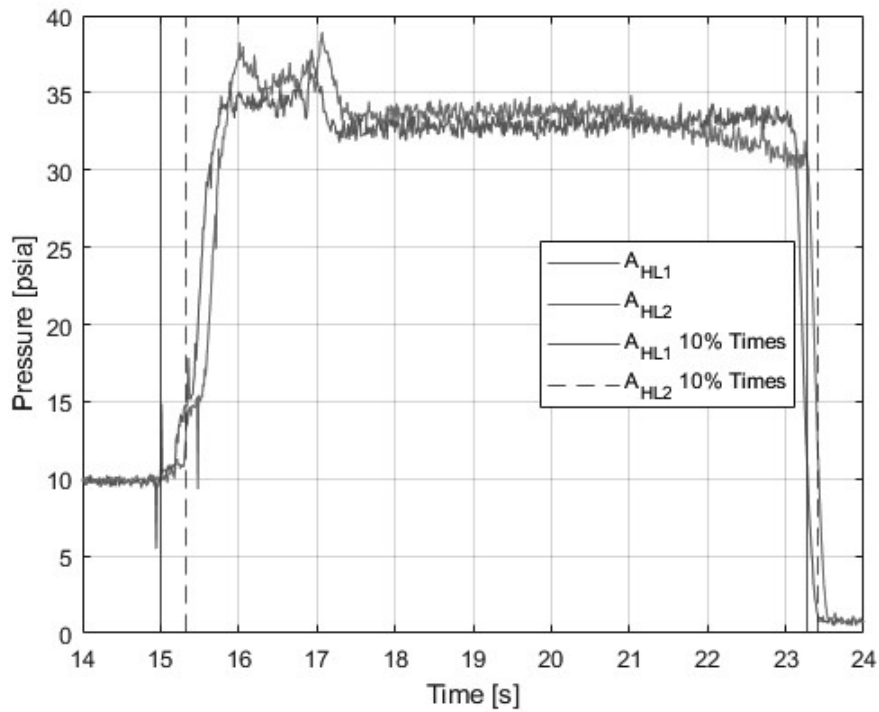

Figure C.7: A_{HH} with 10% P_{max} Times

Figure C.8: A_{HH} with 80% P_{max} Times

Figure C.9: B_{LL} with 10% P_{max} Times
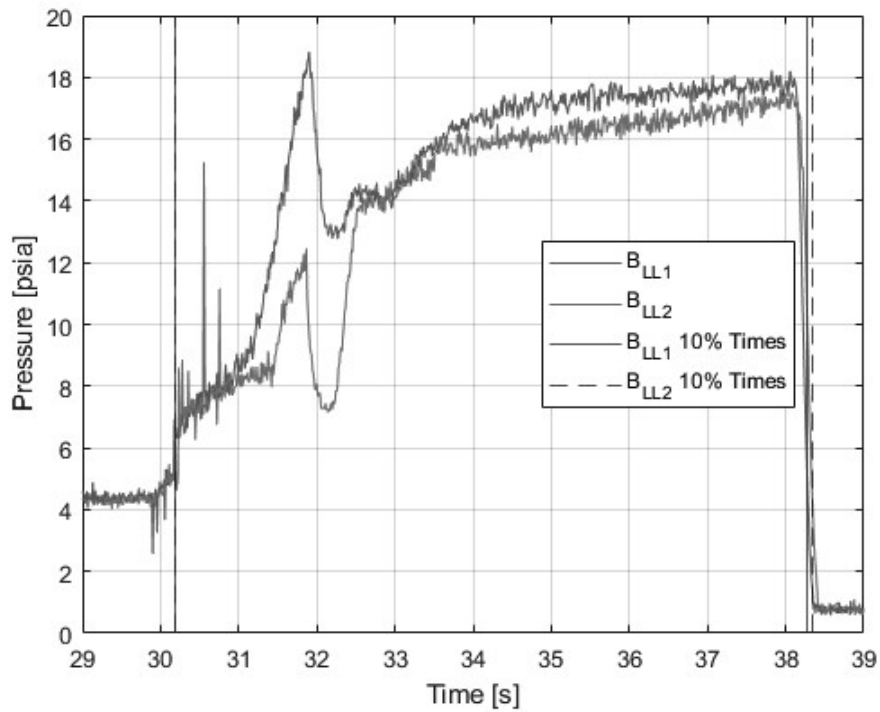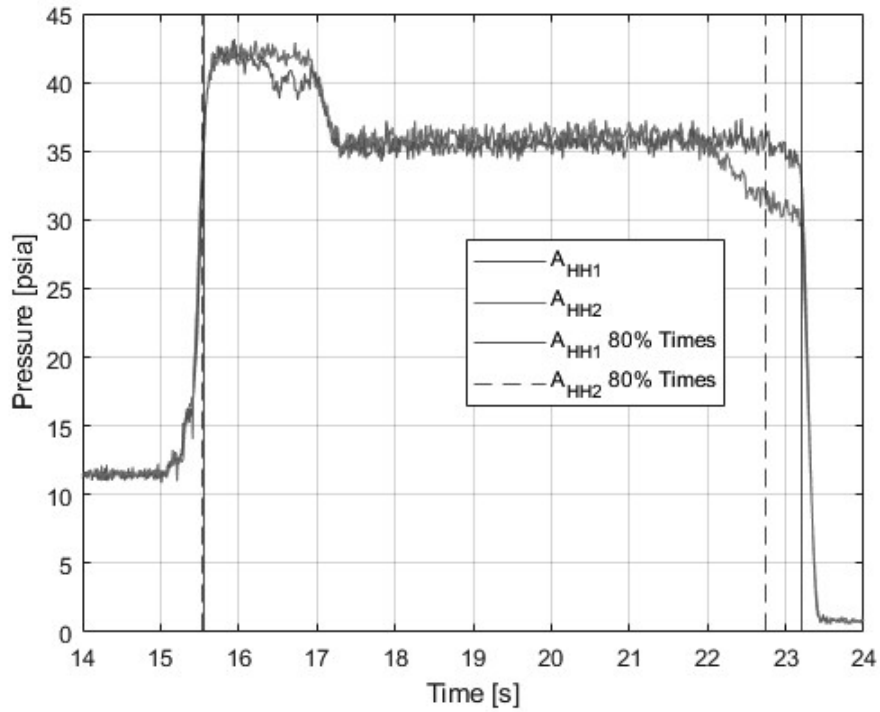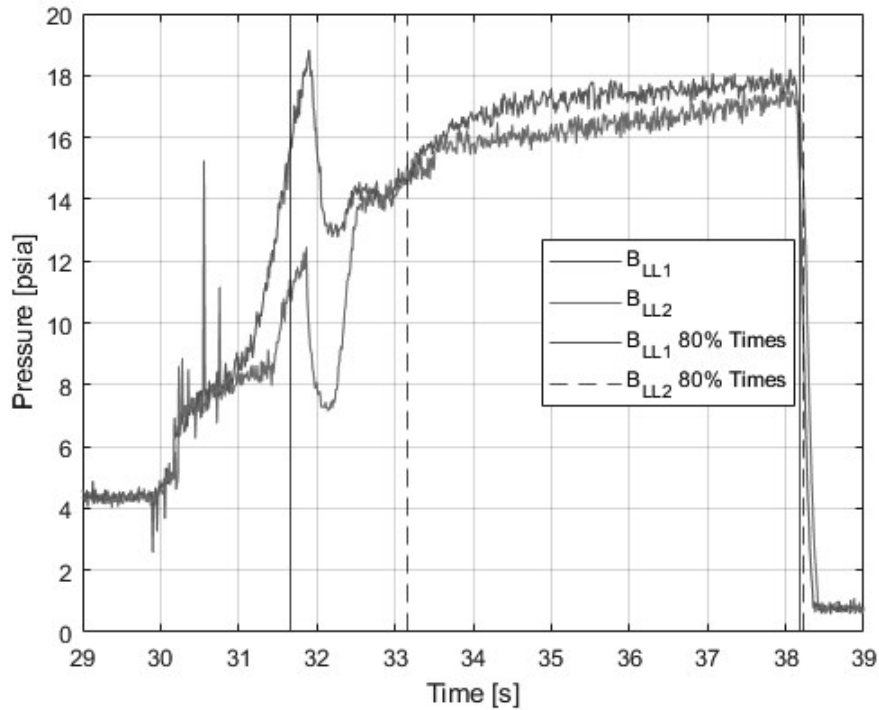
Figure C.10: B_{LL} with 80% P_{max} Times

For the 80% P_{max} on B_{LL2} shown in Figure C.10, there was a large difference between start times even with the traces sharing similar form. The igniter effect on B_{LL2} forced the burn time to start earlier than in B_{LL2}. It is thought that the burn time in B_{LL1} is the better representation of reality, and thus its burn start time is used for both traces during the analysis process. The traces in Figure C.14 have the same issue and were dealt with in the same manner. The earlier of the two was taken to the correct value and used for both tests.
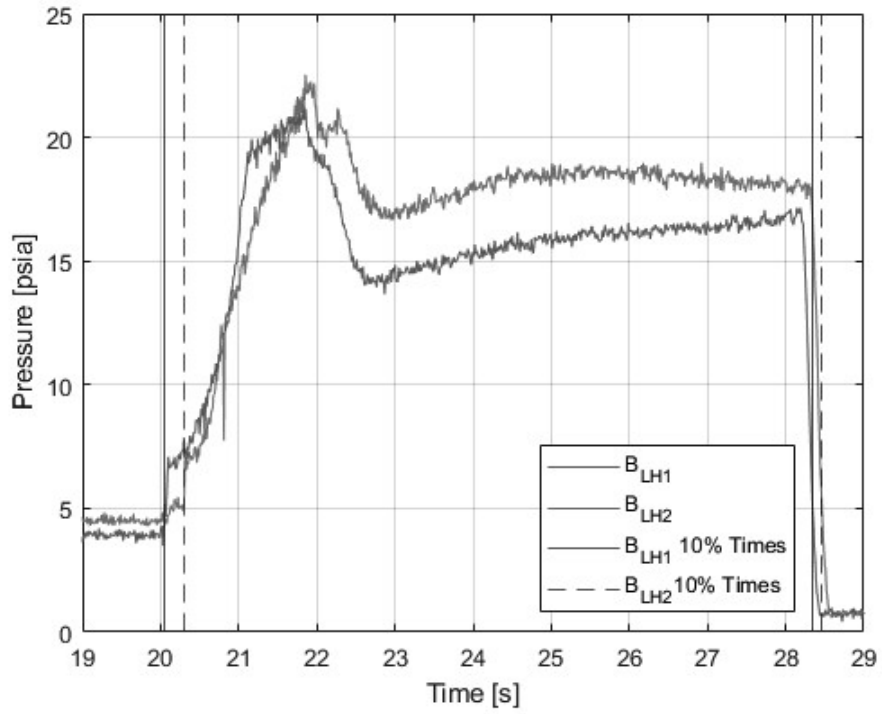
Figure C.11: B_{LH} with 10% P_{max} Times
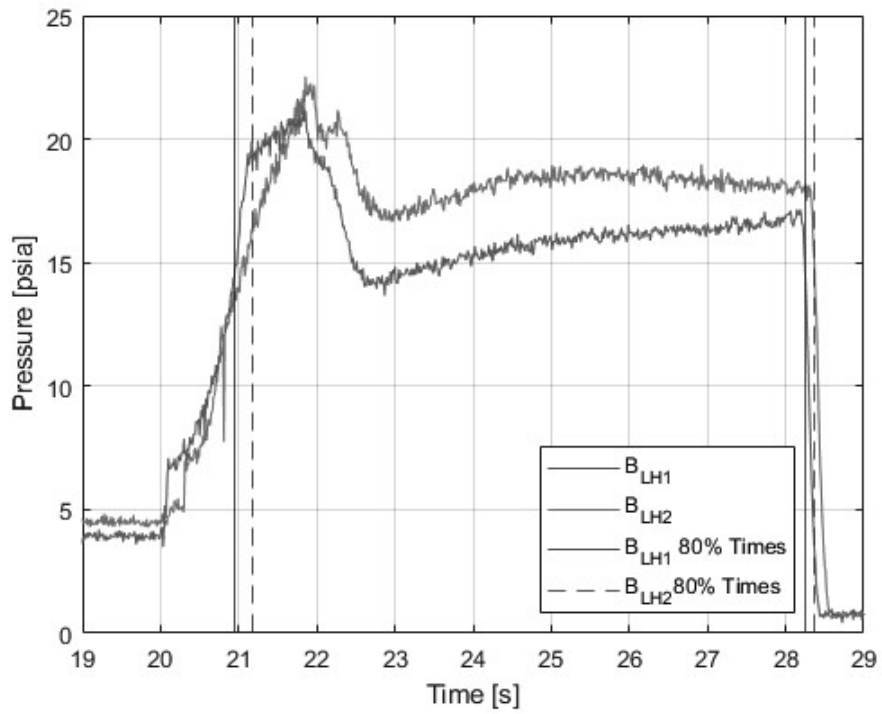
Figure C.12: B_{LH} with 80% P_{max} Times
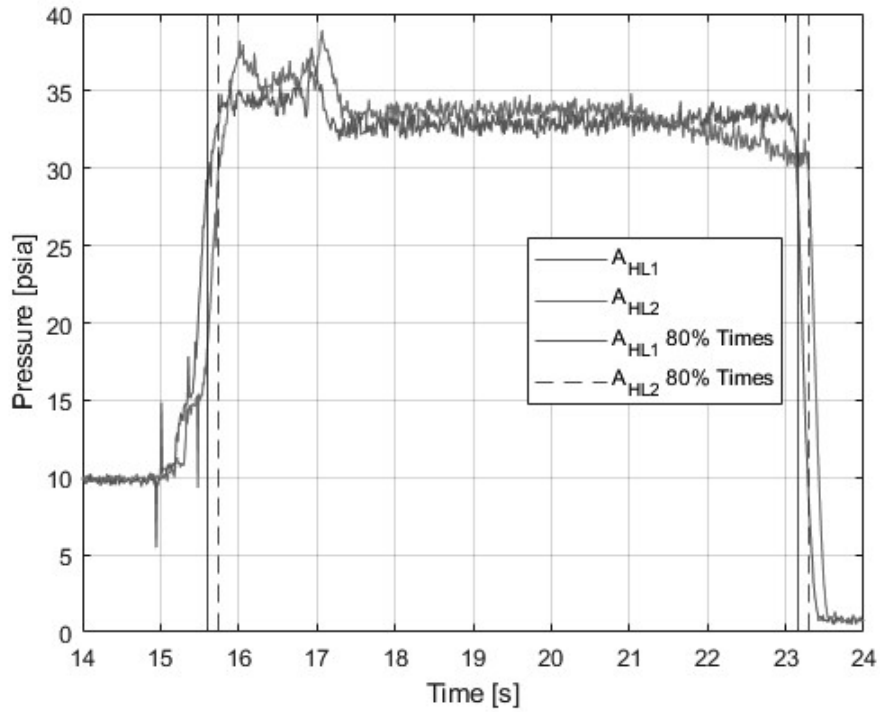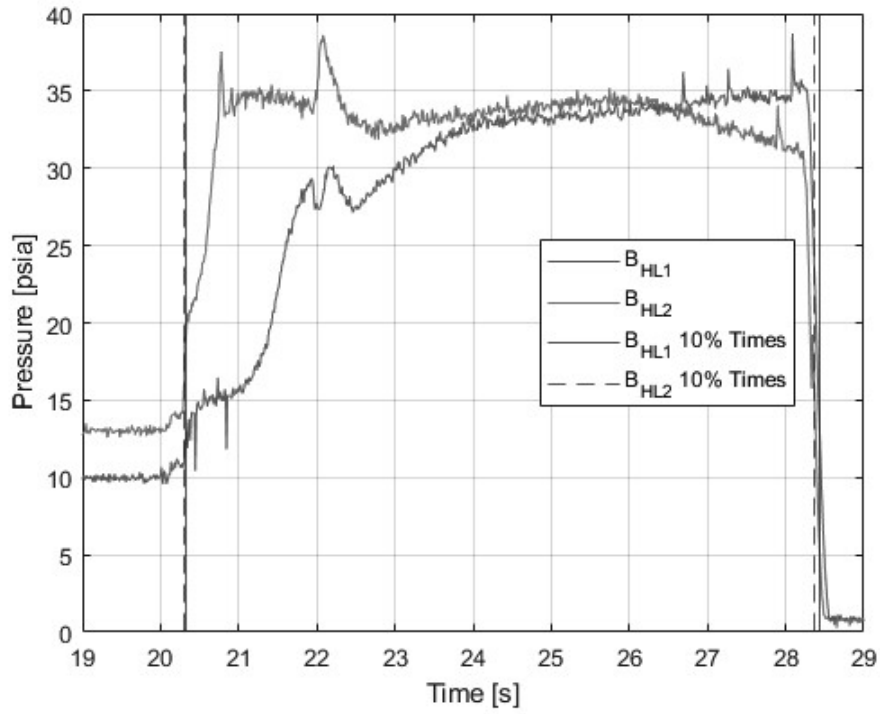
Figure C.13: B_{HL} with 10% P_{max} Times
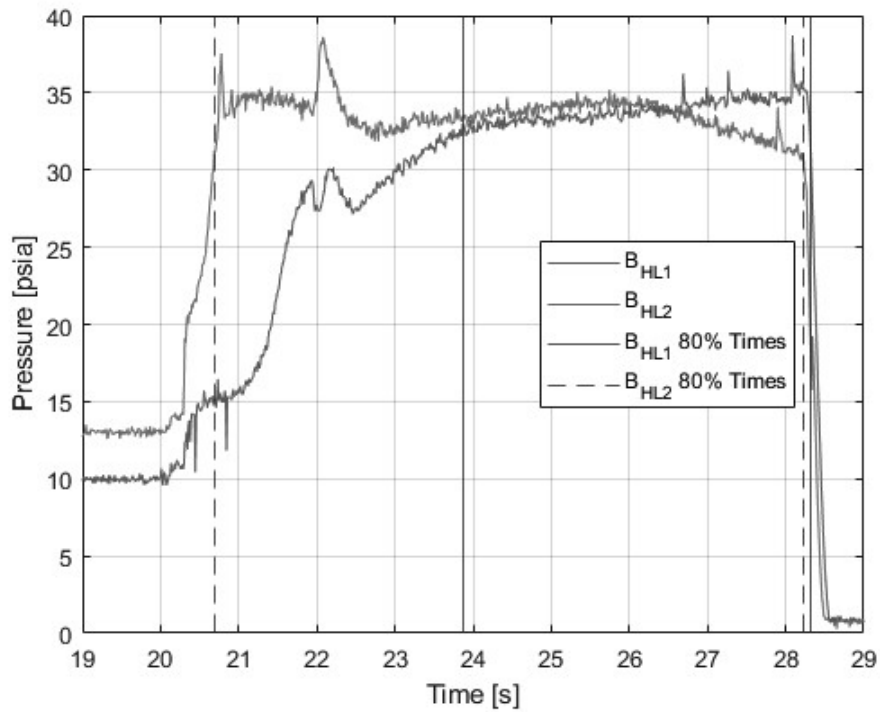
Figure C.14: B_{HL} with 80% P_{max} Times

133
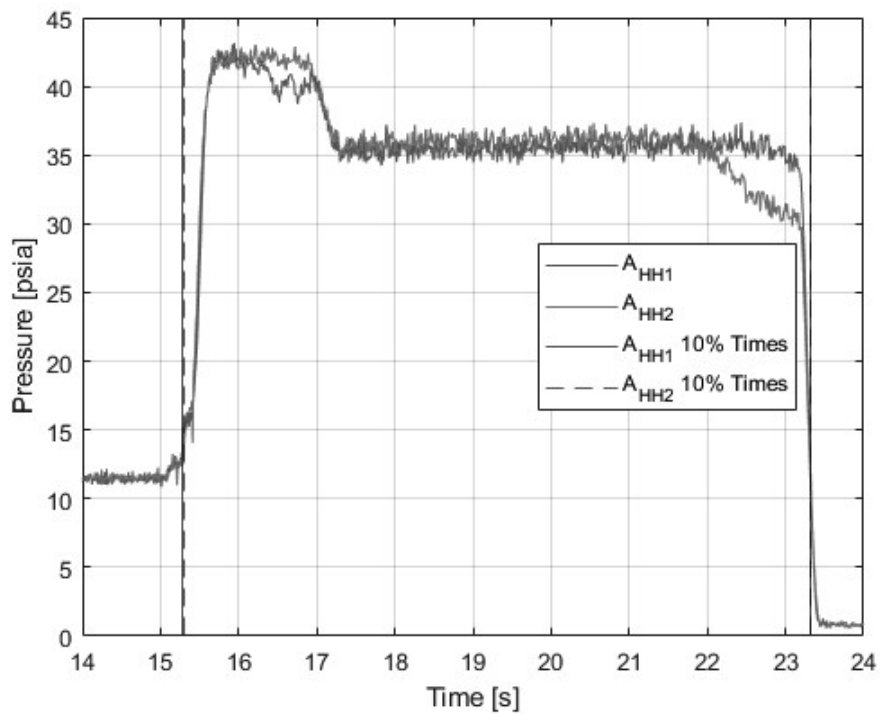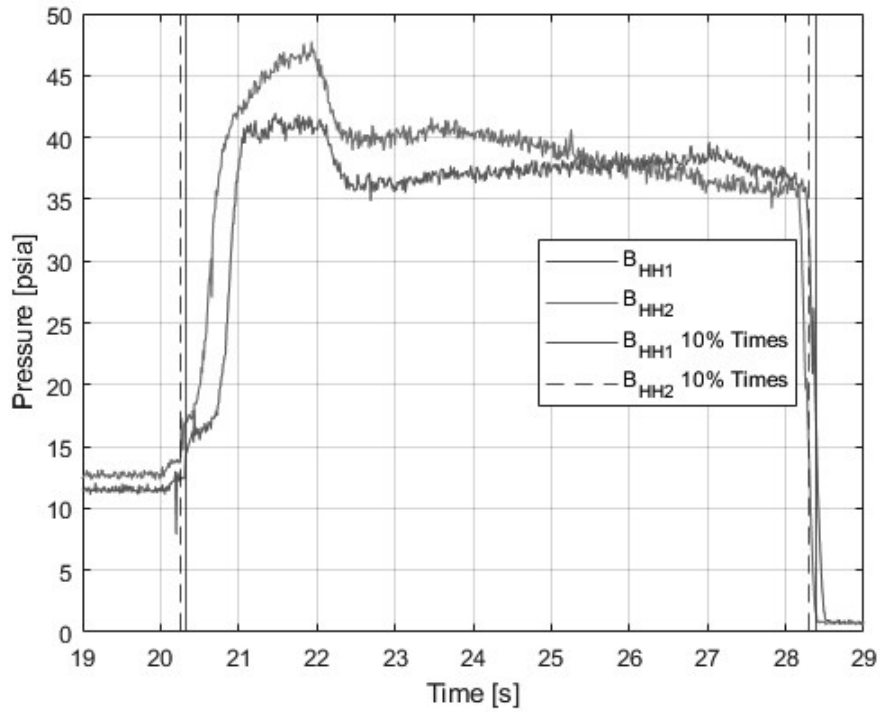
Figure C.15: B_{HH} with 10% P_{max} Times
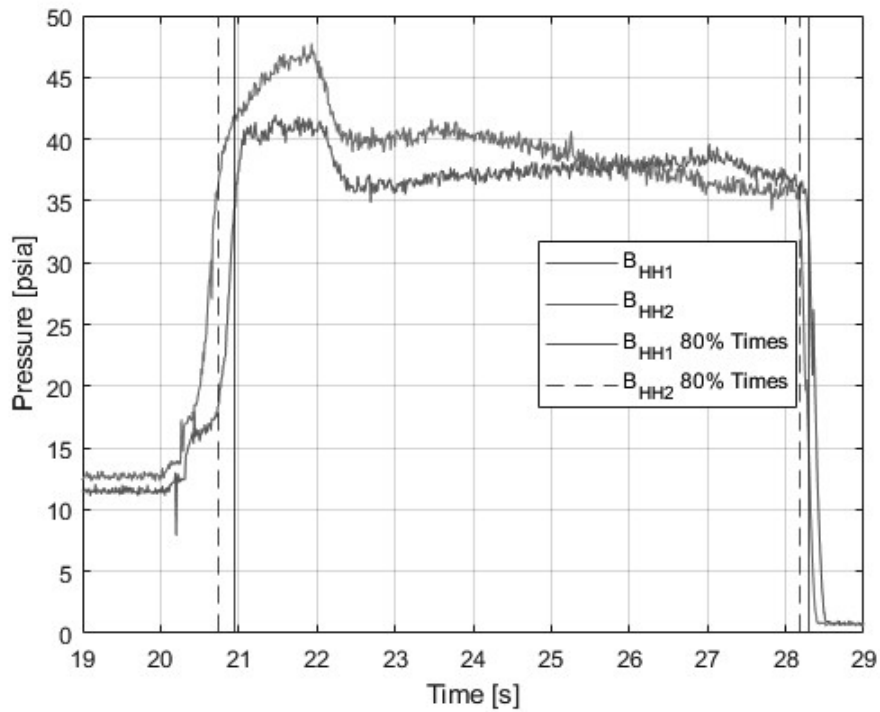
Figure C.16: B_{HH} with 80% P_{max} Times

The pressure transducers have a calibration curve that relates the voltage produced by the transducer to a pressure. This curve was constructed using a deadweight tester. Weights of known values were placed onto the tester to generate a known pressure. From this information a simple linear regression performed to obtain a slope, intercept, and variance. The aft end pressure transducer's calibration curve is show in Figure D.1.
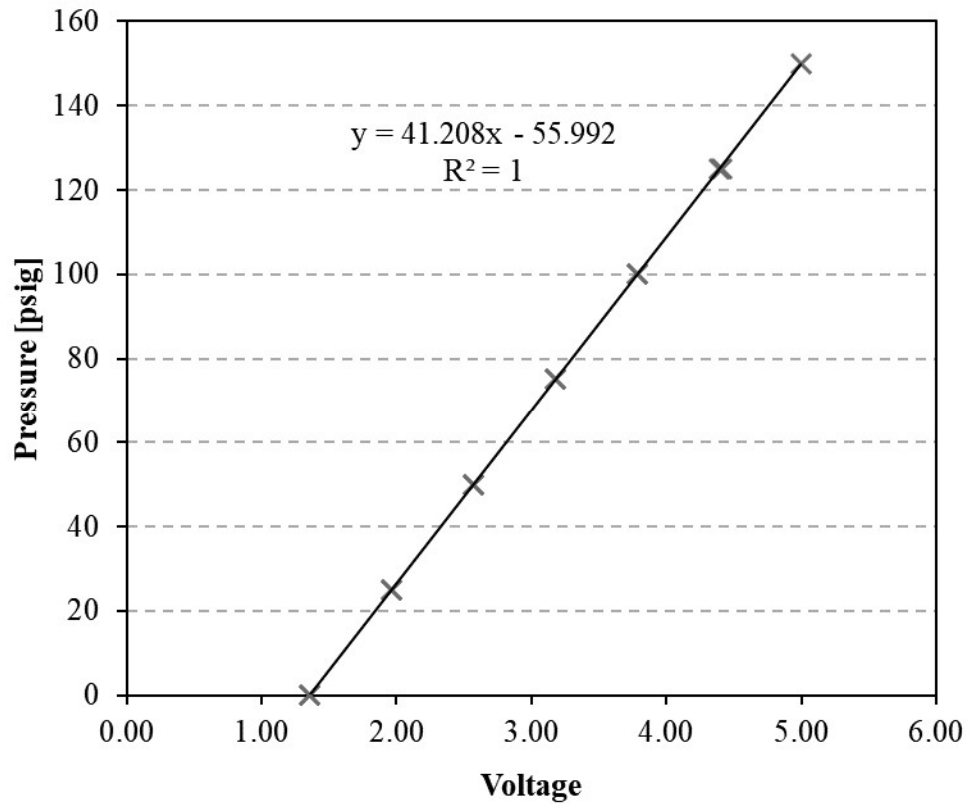
Figure D.1: Aft End Transducer Calibration Curve

The calibration data and curve does not directly provide a relation between the measured pressure and the uncertainty of the measured pressure. The data relates the known deadweight pressure to a voltage with uncertainty on the points in the relationship.

The goal of the MCM for the transducer calibration was to determine a confidence interval on a curve of measured voltage vs known pressure using the methods presented in Section 2.5.5. Using the calibration regression like the one shown in Section 2.5.6, a curve of measured pressure vs known pressure was constructed. The confidence intervals based from the previous MCM were fit to the new curve. For the MCM, the measured voltages and the dead weight tester pressures were taken as the inputs. The errors for each are shown in Table 4.5. The relative uncertainty of the aft end transducer is shown in Figure D.2.
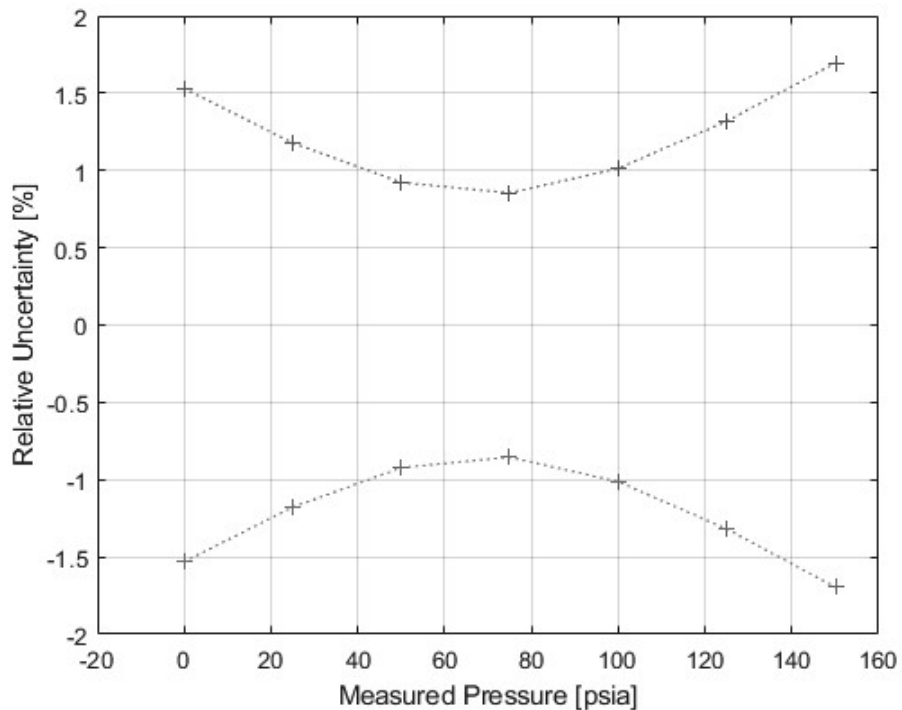
Figure D.2: Aft End Transducer Uncertainty Intervals

Table D.1: Transducer Calibration Uncertainties

Variable	Distribution	μ	2σ	Units	Description
V_{calib}	Normal	0	ε_r	V	Direct random error in time history of voltage data at each point
P_{calib}	Normal	0	0.001%	psi	Systematic error for deviation in weight from stated value

The calibration uncertainty was taken to be value of the value of the uncertainty interval at the measured pressure of interest. This was done to produce a single value for the uncertainty interval which reduces the complexity of the MCM code. In general, it is not always possible to condense the uncertainty intervals into a single point, but the transducer uncertainty intervals were flat over the range of interest which makes in an acceptable substitution.

PRC Calibration Report

Date:	8/2/2019		
Operator :	Dan Jones/ James Venters	Calibration Source:	Instrument Type: Dead Weight Pressure Tester
			Model #: R 50
Instrument	Pressure Transducer		Serial #: 17745
Range	0-150 (psig)		
Manufacturer	GE		
Model	Unik 5000	Slope	41.33 psi/V
Serial Number	11290186	Offset	-56.32 psi

Known Pressure		Measured Voltage	
[psig]		[V]	
0.00	#	1.362615	0.0001
25.00	#	1.967639	0.0002
50.00	#	2.570485	0.0002
75.00	#	3.174952	0.0001
100.00	#	3.780764	0.0001
125.00	#	4.387068	0.0001
150.00	#	4.994166	0.0001
125.00	#	4.387668	0.0002
100.00	#	3.781634	0.0002
75.00	#	3.176226	0.0001
50.00	#	2.571767	0.0001
25.00	#	1.968807	0.0002
0.00	#	1.365227	0.0002

Figure D.3: Head End Transducer Calibration Data

PRC Calibration Report

Date:	8/31/2018		
Operator :	Dan Jones/ James Venters	Calibration Source:	Instrument Type: Dead Weight Pressure Tester
			Model #: R 50
Instrument	Pressure Transducer		Serial #: 17745
Range	0-150 (psig)		
Manufacturer	GE		
		Slope	41.21	psi/V
Model	Unik 5000		
		Offset	-55.99	psi
Serial Number	11290191		

Known Pressure [psig]		Measured Voltage [V]	
0.00	#	1.360736	0.0002
25.00	#	1.966781	0.0002
50.00	#	2.568767	0.0016
75.00	#	3.175348	0.0002
100.00	#	3.78129	0.0001
125.00	#	4.388337	0.0001
150.00	#	4.995793	0.0001
125.00	#	4.411002	0.0001
100.00	#	3.781935	0.0001
75.00	#	3.175902	0.0002
50.00	#	2.570666	0.0001
25.00	#	1.967341	0.0001
0.00	#	1.360863	0.0002

$R^2 = 1$

Figure D.4: Aft End Transducer Calibration Data

PRC Calibration Report

Date:	8/31/2018				
Operator :	Dan Jones/ James Venters		Calibration Source:	Instrument	Dead Weight Pressure Tester
				Model #:	R 50
Instrument	Pressure Transducer			Serial #:	17745
Range	0-500 (psig)				
Manufacturer	GE				
			Slope	125.09	psi/V
Model	Unik 5000				
			Offset	-124.73	psi
Serial Number	5483229				

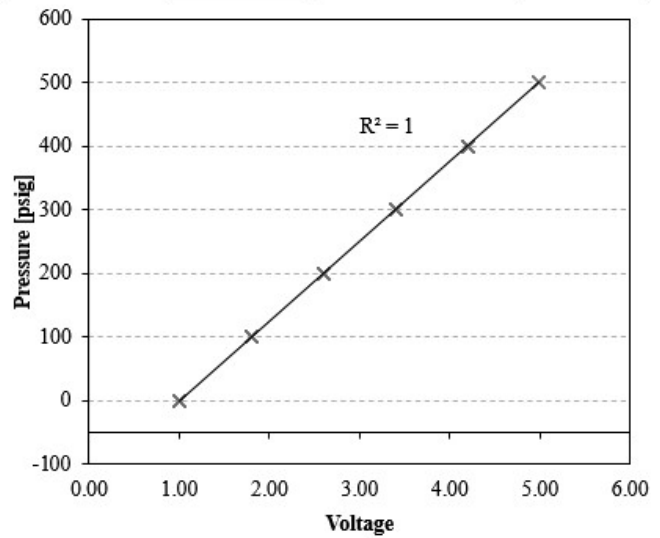| Known Pressure [psig]		Measured Voltage [V]	
0.00	#	0.996463	0.0001
100.00	#	1.797793	0.0001
200.00	#	2.597851	0.0001
300.00	#	3.397289	0.0002
400.00	#	4.195478	0.0003
500.00	#	4.991175	0.0002
400.00	#	4.195159	0.0002
300.00	#	3.396295	0.0002
200.00	#	2.596604	0.0002
100.00	#	1.796369	0.0002
0.00	#	0.994575	0.0002

Figure D.5 Sonic Nozzle Transducer Calibration Data

REFERENCES

[1] R. S. Fry, "A Century of Ramjet Propulsion Technology Evolution," *AIAA Journal of Propulsion and Power,* vol. 20, no. 1, 2004.

[2] G. P. Sutton and O. Biblarz, Rocket Propulsion Elements Ninth Edition, Hoboken: John Wiley & Sons, Inc., 2017.

[3] S. Krishnan and P. George, "SOLID FUEL RAMJET COMBUSTOR DESIGN," *Progress in Aerospace Sciences,* vol. 34, pp. 219-256, 1998.

[4] Y. M. Timnat, "Recent Developments in Ramjets, Ducted Rockets, and Scramjets," *Progress in Aerospace Sciences,* vol. 27, pp. 201-235, 1990.

[5] P. J. Waltrup, W. M. E., F. Zarlingo and E. Gravlin, "History of U.S. Navy Ramjet, Scramjet, and Mixed-Cycle Propulsion Development," *Journal of Propulsion and Power,* vol. 18, no. 1, pp. 14-27, 2002.

[6] Airforce Technology, "SR-72 Hypersonic Demonstrator Aircraft," [Online]. Available: https://www.airforce-technology.com/projects/sr-72-hypersonic-demonstrator-aircraft/. [Accessed 21 March 2021].

[7] C. Covault, "Hypersonic X-51 Scramjet to Launch Test Flight in May," Future US Inc, 17 May 2010. [Online]. Available: https://www.space.com/8428-hypersonic-51-scramjet-launch-test-flight.html. [Accessed 21 March 2021].

[8] B. Natan and S. Rahimi, "The Status of Gel Propellants in Year 2000," *International Journal of Energentic Materials and Chemical Propulsion,* vol. 5, no. 1-6, pp. 172-194, 2002.

[9] Y. Xiao, Z. Xia, L. Huang, L. Ma and D. Yang, "Experimental investigation of the effects of chamber length and boron," *Acta Astronautica,* vol. 160, pp. 101-105, 2019.

[10] C. Li, C. Hu, X. Xin, Y. Li and H. Sun, "Experimental study on the operation characteristics of aluminum," *Acta Astronautica,* vol. 129, pp. 74-81, 2016.

[11] A. Kuznetsov, Y. Solomon and B. Natan, "Development of a Lab-Scale Gel Fuel Ramjet Combustor," in *46th AIAA/ASME/SAE/ASEE Joint Propulsion Conference & Exhibit*, Nashville, TN, 2010.

[12] M. Hu, Z. Wei, S. Ding and N. Wang, "Numerical investigation of a combined solid fuel scramjet combustor," *Acta Astronautica,* vol. 148, pp. 210-219, 2018.

[13] S. Liu, J. Li, G. Zhu, W. Wang and Y. Liu, "Mixing and combustion enhancement of Turbocharged Solid Propellant Ramjet," *Acta Astronautica,* vol. 143, pp. 193-202, 2018.

[14] O. Musa, C. Xiong and Z. Changsheng, "Combustion characteristics and turbulence modeling of swirling reacting," *Acta Astronautica,* vol. 139, pp. 1-17, 2017.

[15] O. Musa, L. Weixuan, C. Xiong, G. Lunkun and L. Wenhu, "Experimental investigation on the effect of swirling flow on combustion characteristics and performance of solid fuel ramjet," *Acta Astronautica,* vol. 148, pp. 163-174, 2018.

[16] J. A. Blevins and H. W. Coleman, "Uncertainty Assessment of Ramjet Performance," *AIAA Journal of Propulsion and Power,* vol. 13, no. 6, pp. 730-736, 1997.

[17] L. Dunsworth and G. Reed, "Ramjet Engine Testing and Simulation Techniques," *Journal of Spacecraft and Rockets,* vol. 16, no. 6, 1979.

[18] Advisory Group for Aerospace Research & Development, "Experimental and Analytical Methods for the Determination of Connected-Pipe Ramjet and Ducted Rocket Internal Performance," North Atlantic Treaty Organization, Neuilly Sur Seine, France, 1994.

[19] P. G. Hill and C. R. Peterson, Mechanics and Thermodynamics of Propulsion, Reading, Massachusetts: Addison-Wesley Publishing Company , 1965.

[20] W. Brooks, "Workshop Report: Burn Rate Determination Methodology," in *18th JANNAF Combustion Meeting, Jet Propulsion Laboratory*, Pasadena, CA, 1981.

[21] A. G. f. A. R. &. Development, "Sonic Nozzles for Mass Flow Measurement and Reference Nozzles for Thrust Verification," North Atlantic Treaty Organization , Neuilly Sur Seine, France, 1997.

[22] M. Anklin, W. Drahm and A. Rieder, "Coriolis mass flowmeters: Overview of the current state of the art and latest research," Elsevier Ltd., 2006.

[23] H.-B. Ding, C. Wang and G. Wang, "Thermal Effect on Mass Flow-Rate of Sonic Nozzle," *Thermal Science,* vol. 22, no. 1A, pp. 247-262, 2018.

[24] J. Nanigan and D. Nanigan, "A Unique Thermocouple to Measure Temperatures of Squibs, Ingniters, Propellants, and Rocket Engines," SPIE Paper.

[25] R. Warren, "Design of Thermocouple Probes for Measurement of Rocket Exhauset Plume Temperatures," Aeronautical and Maritime Research Laboratory, Melbourne Victoria, 1994.

[26] K. K. Kou, Principles of Combustion, John Wiley & Sons, Inc. , 2005.

[27] M. A. Hitt, "Regression Rate Stury of Porous Axial-Injection, End Burning Hybrid Fuel Grains, Dissertation," The University of Alabama in Huntsville, Huntsville, AL, 2016.

[28] D. A. Jones, "Advanced Digital Methods for Propellant Burning Rate Determination, A Thesis," The University of Alabama in Huntsville, Huntsville, AL, 2015.

[29] R. S. Fry, L. DeLuca, R. Frederick, G. Gadiot, R. Strecker, H.-L. Besser, A. Whitehouse, J.-C. Traineau, D. Ribereau and J.-P. Reynaud, "Evaluation of Methods for Solid Propellant Burning Rate Measurement," North Atlantic Treaty Organization, 2001.

[30] R. S. Fry, "Solid Propellant Subscale Burning Rate Analysis Method for U.S. and Selected NATO Facilites," The John Hopkins University , Columbia, Maryland, 2002.

[31] L. Knox, "Experimental Determination of Regression Rates of Mixed Hyrbid Propellants, Master's Thesis," The University of Alabama in Huntsville, Huntsville, 2004.

[32] R. A. Frederick Jr. and B. E. Greiner, "Laboratory-Scale Hybrid Rocket Motor Uncertainty Analysis," *Journal of Propulsion and Power,* vol. 12, no. 3, pp. 605-611, 1996.

[33] D. Altman, P. Estey and M. J., "An Evaluation of Scaling Effects for Hybrid Rocket Motors," in *AIAA 27th Joint Propulsion Conference*, Sacramento, CA, 1991.

[34] J. J. Whitehead, Experimental Evaluation of a Mixed Oxidizer Hybrid Concept, Master's Thesis, University of Alabama in Huntsville, 2004.

[35] M. D. Mascaro, Regression Rate Determiation of a Gas Generator Hyrbid Rocket Motor with GOX, Master's Thesis, The University of Alabama in Huntsville , 2015.

[36] B. Raghunandan, E. Ravichandran and A. Marathe, "Combustion related to solid fuel ramjets," *AIAA Journal of Propulsion and Power,* vol. 45, no. 1, pp. 502-504, 1985.

[37] A. Netzer and A. Gany, "Burning and Flameholding Characteristics of a Miniature Solid Fuel Ramjet Combustor," *Journal of Propulsion and Power,* vol. 7, no. 3, pp. 357-363, 1991.

[38] R. LeMoyne, "Fundamental Analysis of a Solid Fuel Ramjet," *AIAA/3AF International Space Planes and Hypersonic Systems and Technologies Conference,* 2012.

[39] J. Gobbo-Ferreira, M. Silva and J. Carvalho Jr., "Performance of an Experimental Polyethylene Solid Fuel Ramjet," *Acta Astronautica ,* vol. 45, no. 1, pp. 11-18, 1999.

[40] W. H. Coleman and W. G. Steele, Experimentation, Validation, and Uncertainty Analysis for Engineers Fourth Edition, Hoboken, New Jersey: Wiley, 2018.

[41] D. M. Lineberry, Interviewee, *Guidance Meeting.* [Interview]. 26 January 2021.

[42] SubSurfWiki, "Skewed Distribution," [Online]. Available: https://subsurfwiki.org/wiki/Skewed_distribution. [Accessed 03 March 2021].

[43] K. K. Brown, H. W. Coleman and W. G. Steele, "Estimating Uncertainty Intervals for Linear Regression," American Institute of Aeronautics and Astronautics, Reno, NV, 1995.

[44] D. Lineberry and P. Berg, *UAH PRC Heated Air Flow Facility,* Huntsville, AL, 2021.

[45] Bronkhorst, "CORIOLIS MASS FLOW MEASURING PRINCIPLE," Bronkhorst USA LLC, [Online]. Available: https://www.bronkhorst.com/en-us/service-support/knowledge-base/coriolis-mass-flow-measuring-principle/. [Accessed 15 February 2021].

[46] ASME, "Fluid Meters Their Theory and Application 6e," 1971.

[47] Weather Underground, "Huntsville, AL Weather History," [Online]. Available: https://www.wunderground.com/history/daily/us/al/huntsville/KHSV/date/2020-10-20. [Accessed 02 March 2021].

[48] F. M. White, Fluid Mechanics 4e, McGraw Hill, 1998.

[49] Purdue University, "7. Solid Rocket Propulsion (SRP) Systems," Purdue, 2008.